

Photodiodes for Applications in Analog Optic Links and Microwave Photonics

A Dissertation

Presented to

the Faculty of the School of Engineering and Applied Science
University of Virginia

In Partial Fulfillment of the
Requirements for the Degree of
Doctor of Philosophy

By

Yiwei Peng

March 2021

APPROVAL SHEET

This Dissertation
is submitted in partial fulfillment of the requirements
for the degree of
Doctor of Philosophy

Author Signature: _____

This dissertation has been read and approved by the examining committee:

Advisor: Joe C. Campbell _____

Committee Chair: Andreas Beling _____

Committee Member: Robert M. Weikle _____

Committee Member: Steven M. Bowers _____

Committee Member: Joshua J. Choi _____

Accepted for the School of Engineering and Applied Science:

Craig H. Benson, School of Engineering and Applied Science

March 2021

© Copyright by

Yiwei Peng

All rights reserved

2021

This dissertation is dedicated to my parents

Contents

Acknowledgement	VIII
Abstract	X
List of Figures	XIII
List of Tables	XX
Chapter 1 Introduction	1
1.1 Photonic Generation of CW Microwave Signal.....	1
1.2 Optical Generation of Pulsed Microwave Signal.....	3
1.3 Analog Optic Link.....	6
1.4 Dissertation Organization.....	8
Chapter 2 Fundamentals of Photodiodes	10
2.1 Figures of Merit of Photodiodes.....	10
2.1.1 Responsivity.....	10
2.1.2 Bandwidth.....	11
2.1.3 Output RF Power.....	14
2.1.4 Linearity.....	19
2.1.5 S-Parameter.....	21
2.2 Fabrication Process Flow.....	22
2.2.1 P-metallization.....	23
2.2.2 P-mesa Etch.....	24
2.2.3 N-mesa Etch.....	25
2.2.4 N-metallization.....	26
2.2.5 P-contact Open.....	27
2.2.6 Seed Layer and Electroplating.....	28
2.2.7 Other Steps.....	29
Chapter 3 High-Power V-Band Photodiodes Flip-Chip Bonded on Diamond	30
3.1 Introduction.....	30

3.2 Device Structure and Simulation.....	31
3.3 Device Fabrication	33
3.4 Device Characterization	34
3.5 Conclusion.....	44
Chapter 4 Optical Generation of Pulsed Microwave Signals	45
4.1 Device Structure	45
4.2 Device Design and Characterization	46
4.3 Impulse Response.....	52
4.4 Pulsed Microwave Signal Generation	55
4.5 Conclusion.....	63
Chapter 5 High-Power and High-Linearity Photodiodes at 1064 nm.....	64
5.1 Introduction	64
5.2 1 st Group of Photodiodes.....	65
5.2.1 Device Design	65
5.2.2 Device Characterization	66
5.3 2 nd Group of Photodiodes	73
5.3.1 Device Design	73
5.3.2 Device Characterization	76
5.3.3 Nonlinear Analysis.....	82
5.4 Conclusion.....	87
Chapter 6 High-Performance Analog Photonic Link	88
6.1 Introduction	88
6.2 Figures of Merit.....	89
6.2.1 Link Gain	89
6.2.2 Noise Figure.....	90
6.2.3 Spurious Free Dynamic Range	92
6.3 Balanced Photodiodes Performance	92

6.3.1 <i>Device Design</i>	92
6.3.2 <i>Device Characterization</i>	95
6.4 Balanced Link Configurations	101
6.5 Low-Biased Link Configurations	106
6.6 Conclusion	110
Chapter 7 Conclusions and Future Work	111
7.1 Conclusions	111
7.2 Future Work	112
7.2.1 <i>High-Power RF Signals Generation</i>	112
7.2.2 <i>Photonic Wireless Emitter</i>	117
7.2.3 <i>Phase Modulated Photonic Links</i>	120
References	122
A. List of Publications	131
B. Vita	133

Acknowledgement

First of all, I would like to thank my advisor, Dr. Joe C. Campbell, with my deepest gratitude. Thanks to his support and insight, I was able to finish my study. I have been extremely lucky to have a supervisor who encouraged my research and allowed me to grow as a research scientist. He is always available to offer me guidance whenever I needed it. His immense knowledge and plentiful experience have encouraged me in my academic research and daily life. It is my fantastic fortune to be a Ph.D. student of such a nice and knowledgeable man who made great contributions to photonics.

I would like to thank my committee members, Dr. Andreas Beling, Dr. Robert M. Weikle, Dr. Steven M. Bowers, and Dr. Joshua J. Choi. They have provided me with great help and guidance on my research, especially Dr. Andreas Beling. I benefited greatly from the discussion with them.

I would like to thank my research group members and colleagues: Keye Sun, Yang Shen, Jiyuan Zheng, Xinjun Xue, Nan Ye, Qinglong Li, Zhanyu Yang, Jizhao Zang, Bassem M. Tossoun, Yuan Yuan, Qianhuan Yu, Andrew H. Jones, Jesse S. Morgan, Fengxin Yu, Ta-Ching Tzu, Junyi Gao, Ze Wang, Dekang Chen, Bintian Guo, Tasneem Fatema, Adam Alexander Dadey, Renjie Wang and Junwu Bai. It was really a great time to work together with them. Especially, I would like to thank Yuan Yuan and Jizhao Zang for mentoring me at the start of my Ph.D. work and Keye Sun and Yang Shen for a lot of help in my academic and daily life.

I would like to thank all the staffs of the Microfabrication Lab at University of Virginia: Alex Lobo, Michael Stogoski, and Joseph Beatrice. Thanks for their careful training and instrument maintenance in the cleanroom. I would also like to thank Dr. Matthew Konkol and Dr. Peng Yao at Phase Sensitive Innovation for their support and collaboration.

Last but not least, I would thank my family: my father Zhilin Peng and my mother Yuzhong Lu. Without understanding and support from them, I definitely could not finish my Ph.D research work. I love them deeply and I am forever grateful for their love.

Yiwei Peng

University of Virginia

March 2021

Abstract

In recent years, analog photonic links (APLs) have emerged as promising alternatives to all-electrical coaxial cable systems as they can provide low loss, broad bandwidth, immunity to electromagnetic interference (EMI), and reduced size and weight. With these advantages, APLs have been widely investigated in broadband wireless access networks, radio-over-fiber, and phased-array radar systems. The microwave range is the primary operating frequency for these systems due to its broad bandwidth and high data transmission rate. Photonic generation of continuous wave (CW) and pulsed microwave signals can provide widely tunable carrier frequency range with low phase noise and reduced system cost by eliminating the expensive electronic components. In these systems, the photodiode must be able to deliver very high photocurrent and, thus high radio frequency (RF) output power to improve link gain and signal-to-noise ratio, while maintaining high linearity. However, at present, the bottleneck in increasing the dynamic range and signal-to-noise ratio in these optical links is the power handling capabilities of the photodiodes.

Based on that, the primary focus of this work is to address some of these issues by demonstrating high-power photodiodes and their performance in microwave analog photonic links. High-power V-band charge-compensated modified uni-travelling-carrier (CC-MUTC) photodiodes at 1550 nm were developed and characterized. The devices were flip-chip bonded to diamond with high-thermal-conductivity for improved heat dissipation. The output power of 18 μm - and 24 μm - diameter devices was 22.3 dBm and 24.3 dBm at 50 GHz and 41 GHz, respectively. Compared to previous results with active cooling, the output RF power improved by more than 57% and the failure power density increased by more than 36%.

I also demonstrated photonic microwave generation of high-power pulsed signals in the X-, Ku- and K-band using the CC- MUTC photodiodes. The impulse photoresponse without modulation showed a maximum peak voltage of 38.3 V and full-width at half-maximum (FWHM) of 30 ps. High-power pulsed microwave signals at 10, 17 and 22 GHz with peak power up to 44.2 dBm (26.3 W), 41.6 dBm (14.5 W) and 40.6 dBm (11.5 W) were achieved, respectively. The record high peak power is desirable in radar and wireless applications.

In addition to work at 1550 nm, I have also designed, fabricated, and characterized high-power and high-linearity photodiodes at 1064 nm. Two groups of devices were designed and investigated. For the 1st design, the photodiodes with 15 μm and 18 μm diameters achieved 18.6 dBm RF output power at 55 GHz and 19.4 dBm RF output power at 41 GHz, respectively. The dark currents of these devices were typically below 10 nA at -8 V bias. The bandwidth was analyzed with parameters obtained from S-parameter fitting. There was good agreement between measured and calculated bandwidth. Based on the analysis, the redesigned 2nd group showed 48% higher bandwidth efficiency product (BEP). The RF output powers of photodiodes with diameters of 10 μm and 20 μm were 15 dBm at 60 GHz and 21.7 dBm at 39 GHz, respectively. The measured third-order intercept point (OIP3) showed a high linearity of 33 dBm at 40 GHz. A circuit analysis based on Z-parameter extraction indicates that voltage-dependent and photocurrent-dependent capacitance components are the primary nonlinear mechanisms for these photodiodes at high frequency.

Finally, using the same epitaxial wafer, I designed balanced photodiodes that delivered powers of 17.7 dBm, 19.8 dBm, 20.7 dBm and 22 dBm at 38 GHz, 29 GHz, 27 GHz and 24.5 GHz, respectively. High common-mode rejection ratio (CMRR) of 25 dB and good linearity with an OIP3 of 34 dBm were measured at 38 GHz for 10 μm -diameter balanced photodiodes. I

demonstrated two analog photonic links with different noise reduction techniques without electronic amplification. In the first link, I used balanced detection with a quadrature-biased Mach–Zehnder modulator (MZM) for noise cancellation. Link gain of 6.8 dB, noise figure (NF) of 25.8 dB and spurious free dynamic range (SFDR₃) of 114 dB·Hz^{2/3} at 38 GHz were achieved. The second link worked at low bias modulation for improved signal-to-noise ratio with a single photodetector. Record-high gain (19.3 dB at 26 GHz and 17 dB at 38 GHz) and low noise figure (14.5 dB at 26 GHz and 17 dB at 38 GHz) were demonstrated.

List of Figures

Figure 1-1. Environmental remote sensing system architecture [15].	2
Figure 1-2. Microwave photonics in a radar system.	4
Figure 1-3. A picture of the field-trial demonstrator. DSP, digital signal processor.	5
Figure 1-4. Schematic diagram of analog photonic link.	6
Figure 1-5. Calculated (a) RF link gain, (b) RF noise figure and (c) SFDR as a function of DC current.	7
Figure 2-1. Simplified circuit of photodiode	12
Figure 2-2. Simulated bandwidth of photodiode with and without an inductor	13
Figure 2-3. (a) Band diagram, carrier concentration and (b) electric field of PIN photodiodes...	15
Figure 2-4. Velocity of electrons and holes in InGaAs [53].	16
Figure 2-5. (a) Band diagram, carrier concentration, (b) electric field of UTC photodiodes and (c) band diagram, carrier concentration, (d) electric field of MUTC photodiodes	16
Figure 2-6. Electron saturation velocity versus temperature for InGaAs [60].	18
Figure 2-7. 3D view of flip-chip bonding process.	19
Figure 2-8. Frequency spectrum of a nonlinear system.	20
Figure 2-9. Definition of OIP3.	21
Figure 2-10. (a) Equivalent circuit in Keysight ADS software; (b) measured and fitting S parameter.	22
Figure 2-11. (a) Cross section of surface-illuminated photodiode; (b) fabrication process flow.	23
Figure 2-12. Schematic cross section of (a) patterned photoresist and (b) p-mesa.	24
Figure 2-13. Schematic cross section of (a) patterned photoresist and (b) n-mesa.	25
Figure 2-14. Schematic cross section of (a) patterned photoresist and (b) n-metal.	26

Figure 2-15. Schematic cross section of (a) patterned photoresist and (b) open p-contact.	27
Figure 2-16. Schematic cross section of (a) patterned photoresist and (b) seed layer and electroplating.....	28
Figure 2-17. Wafer before and after dicing.	29
Figure 3-1. The epitaxial layer design of InGaAs/InP MUTC.	32
Figure 3-2. Simulations of (a) frequency response and (b) saturation current of 28 μm -diameter photodiodes.	32
Figure 3-3. (a) Parameter analyzer for IV measurement; (b) dark current versus device diameter at different bias voltage.....	34
Figure 3-4. (a) LCR meter for CV measurement; (b) Current-voltage curves for devices with different sizes; (c) measured and fitted capacitances.....	35
Figure 3-5. Optical heterodyne setup.....	36
Figure 3-6. Bandwidth measurement under -6 V bias voltage of devices with (a) 32 μm -diameter, (b) 28 μm - diameter, (c) 24 μm -diameter and (d) 18 μm -diameter.	38
Figure 3-7. Output RF power versus photocurrent for devices with (a) 32 μm -diameter, (b) 28 μm - diameter, (c) 24 μm -diameter and (d) 18 μm -diameter.	39
Figure 3-8. Summary of RF power versus frequency.....	40
Figure 3-9. Two-tone OIP3 measurement setup.	41
Figure 3-10. Measured OIP3 versus (a) photocurrent at 20 GHz; (b) frequency at 33 mA.	42
Figure 3-11. The SIMS results of InGaAs/InP wafers.....	43
Figure 4-1. (a) Schematic cross section of InGaAs-InP MUTC photodiodes; (b) Photomicrograph of photodiodes.....	47

Figure 4-2. (a) Simulated breakdown voltage and peak power versus absorber thickness; Simulated electric field distribution at (b) -32 V and (c) -44 V when depleted absorber thickness is 350 nm.....	48
Figure 4-3. Current–voltage characteristic of a 50 μm -diameter device.	50
Figure 4-4. Frequency responses of the flip-chip-bond device with diameter of (a) 50 μm , (b) 40 μm and (c) 34 μm at different photocurrents.....	51
Figure 4-5. RF output power of 50 μm diameter device versus average photocurrent for different bias voltages at 10 GHz.	52
Figure 4-6. Normalized impulse response for different average photocurrents at (a) -17 V and (b) -36 V.	53
Figure 4-7. Maximum peak voltage versus bias voltage. Inset: Output peak voltage versus average optical power at -39.5 V.	54
Figure 4-8. Experimental setup for pulsed microwave signals generation.	55
Figure 4-9. Normalized shape of (a) rectangle waveform; (b) pattern generator output waveform and (c) EDFA transient waveform.....	56
Figure 4-10. Normalized output signal in (a) frequency domain and (b) time domain.	58
Figure 4-11. Waveform of the pulsed RF signal at 4 GHz. Inset: Waveform of input optical signal.	59
Figure 4-12. Peak power measured at (a) 10 GHz, (b) 17 GHz and (c) 22 GHz with 30 MHz repetition rate for different photocurrents at room temperature; (d) Maximum peak power and bias voltage at different duty cycles.....	60

Figure 4-13. Peak power measured at (a) 10 GHz, (b) 17 GHz and (c) 22 GHz with 30 MHz repetition rate for different photocurrents at -10 °C; (d) Maximum peak power at different repetition rate.	62
Figure 5-1. Epitaxial layer configuration of InGaAsP/InP photodiode.	66
Figure 5-2. Dark current versus bias voltage curves of devices with diameters from 10 μm to 28 μm.	67
Figure 5-3. Measured and calculated capacitances.	67
Figure 5-4. Measured S_{11} and fitting curves for photodiodes with: (a) 10 μm diameter; (b) 15 μm diameter; (c) 18 μm diameter; (d) 20 μm diameter; (e) 24 μm diameter.	68
Figure 5-5. Measured frequency response of photodiodes with different diameters.	70
Figure 5-6. Measured frequency response of 18 μm-diameter photodiode at different photocurrent.	71
Figure 5-7. Measured and simulated frequency response.	71
Figure 5-8. Output RF power and power compression at – 6 V bias voltage for photodiodes with: (a) 15 μm and 18 μm diameter; (b) 20 μm diameter and 24 μm diameter.	73
Figure 5-9. (a) Schematic cross section of InGaAs-InP MUTC photodiodes. (b) Band diagram of MUTC photodiodes. (c) Photomicrograph of photodiodes. (d) Photomicrograph of an AlN submount with CPW pads.	75
Figure 5-10. Dark current versus voltage for photodiodes with diameters from 10 to 20 μm. ...	76
Figure 5-11. Measured responsivity of a 10 μm-diameter photodiode.	77
Figure 5-12. Measured frequency response of photodiodes with various diameters.	77
Figure 5-13. Measured frequency response of a 16 μm-diameter photodiode.	78

Figure 5-14. RF output power and power compression versus photocurrent for photodiodes with: (a) 10 μm -, 14 μm -, (b) 16 μm -, 18 μm - and 20 μm - diameters.	79
Figure 5-15. (a) Measured fundamental power and IMD2 versus input power; (b) measured OIP ₂ versus photocurrent at 20 GHz for different bias; (c) measured fundamental power and IMD3 versus input power; (d) calculated and measured OIP ₃ versus photocurrent at 40 GHz for different bias.	82
Figure 5-16. (a) Equivalent circuit of the flip-chip bonded photodiodes. (b) Measured S11 (solid line) and fitting curves (dotted line) for a 16 μm -diameter photodiode.	83
Figure 5-17. Calculated capacitance (left axis) and differential capacitance (right axis) from the imaginary part of the 16 μm -diameter photodiode impedance versus photocurrent at 40 GHz and bias voltages of: (a) -6 V and (b) -7 V.	84
Figure 5-18. Calculated capacitance (left axis) and differential capacitance (right axis) from the imaginary part of the 16 μm -diameter photodiode impedance versus bias voltage at 40 GHz and photocurrent of 29 mA.	85
Figure 6-1. Photomicrograph of balanced photodiodes.	93
Figure 6-2. (a) Old version CPW design for our balanced photodetector; (b) New version CPW design for the balanced photodetector.	94
Figure 6-3. Simulated RF output power for (a) Old version CPW design; (b) New version CPW design.	94
Figure 6-4. Measured frequency response of photodiodes with various diameters.	96
Figure 6-5. Measured frequency response of photodiodes with various diameters.	97
Figure 6-6. CMRR for devices with 18 μm -, 16 μm - and 14 μm -diameter.	98

Figure 6-7. RF output power and power compression versus total photocurrent for balanced photodiodes with: (a) 10 μm -, 14 μm -, (b) 16 μm - and 18 μm -diameters.	99
Figure 6-8. State-of-the-art maximum RF output power for balanced photodiodes versus frequency.....	100
Figure 6-9. Measured OIP3 of balanced photodiodes at 38 GHz.	100
Figure 6-10. Experimental setup for balanced analog photonic link.	101
Figure 6-11. Noise figure and gain versus total photocurrent for balanced links using photodiodes with: (a) 10 μm -, (b) 14 μm -, (c) 16 μm - and (d) 18 μm -diameters.	103
Figure 6-12. Calculated thermal noise, shot noise and laser noise powers and measured noise power spectral density at different photocurrents at 24 GHz.	104
Figure 6-13. The link SFDR at 38 GHz versus bias voltages and photocurrents.	105
Figure 6-14. Experimental setup for low-bias photonic link.	106
Figure 6-15. Gain and noise figure at 25 GHz and 20 mA photocurrent versus bias point.....	107
Figure 6-16. Noise figure and link gain versus photocurrents at: (a) 26 GHz and (b) 38 GHz.	108
Figure 6-17. State-of-the-art (a) link gain and (b) noise figure as a function of frequency at 1550 nm and this work at 1064 nm. Hollow markers: low-biased intensity-modulated links; solid markers: quadrature-biased intensity-modulated links with balanced detection; half-filled markers: phase-modulated (PM) links. The links are amplifierless analog photonic links.	109
Figure 7-1. Schematic of TWPD.	113
Figure 7-2. Simulated (a) bandwidth and (b) S_{11}	114
Figure 7-3. (a) Equivalent circuit model of aperiodic TWPD; (b) simulated RF output.....	115
Figure 7-4. Layout of an (a) inductor and (b) capacitor.	116
Figure 7-5. Electric field with and without Zn diffusion.	116

Figure 7-6. Simulated (a) S parameter and (b) gain of antenna..... 117

Figure 7-7. Layout of photonic wireless emitter..... 118

Figure 7-8. Normalized output signal in (a) frequency domain and (b) time domain..... 119

Figure 7-9. Simulated gain of phased array..... 120

Figure 7-10. Experimental setup of phase modulated links with quadrature biased MZI and
balanced photodiodes..... 121

List of Tables

Table 5-1. Measured and fitted parameters.....	69
Table 5-2. Saturation characteristics.....	80

Chapter 1 Introduction

With the development of low-loss fiber, fiber optic links have proved to be advantageous compared to traditional coaxial cable systems for broad applications areas in terms of low loss, high EMI immunity and large bandwidth [1-3]. It is now possible to transmit massive amounts of information at record-high speeds, with minimal loss and interference [4]. The speed and volume of information transmission have paved the path for innovations in telecommunication, network and other data transmission industries [5].

1.1 Photonic Generation of CW Microwave Signal

Microwave refers to electromagnetic waves with frequencies between 300 MHz and 300 GHz. This frequency range is between the radio waves and infrared waves. The majority of applications for microwave technology are wireless networking and communications systems, security systems, radar systems, environmental remote sensing, and medical systems [6-8].

Microwave is extensively used for telecommunications due to its broad bandwidth and high data transmission rates. Wireless networks, such as Bluetooth and the IEEE 802.11 specifications used for Wi-Fi operate at 2.4 GHz [9, 10]. The frequency bands used for 5G (between 3 GHz to 28 GHz), which achieves download speeds in the gigabit per second (Gbit/s) range [11, 12] also fall within this spectrum.

Compared to visible and infrared light, microwaves have longer wavelength, which allows microwave radiation to penetrate through cloud cover, haze, dust, and rainfall [13, 14]. This property enables detection of microwave energy under almost all weather and environmental conditions [15].

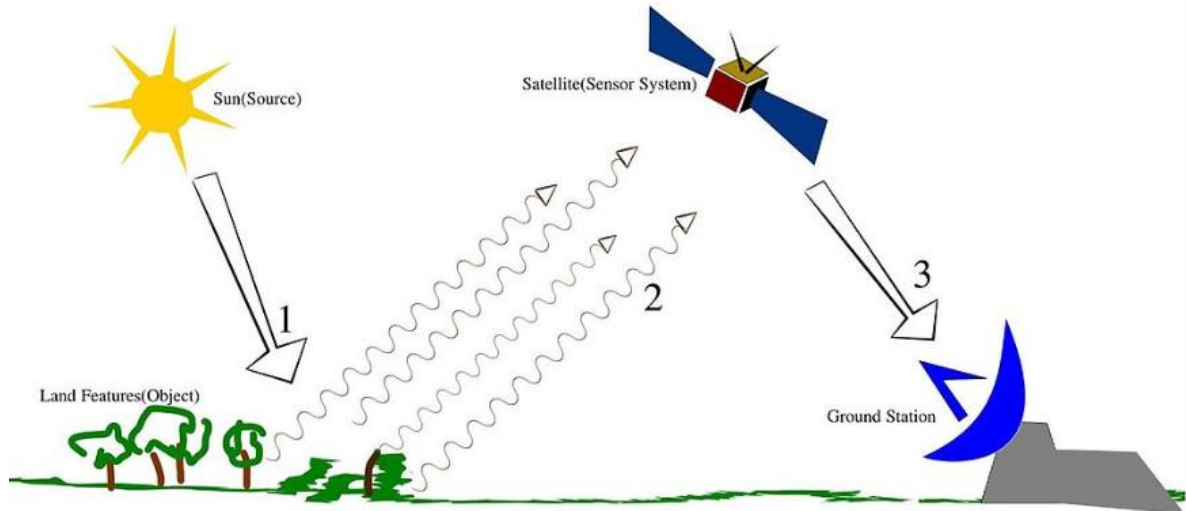


Figure 1-1. Environmental remote sensing system architecture [15].

It is beneficial to generate the microwave carrier signals of good quality for high-speed and high-power applications. Various solid-state devices have been developed as millimeter sources such as Gunn diodes [16], IMPATT diodes [17], TUNNEL diodes [18]. However, these electrical methods are limited by low-power output and high phase noise. Photonic microwave generation can provide broad, tunable bandwidth with low loss and suppressed phase noise compared with electrical generation methods [19, 20].

Photonic generation microwave signals is typically achieved by one of two methods [21, 22]. In the first method, optical signals from two different laser sources are heterodyned on a photodetector. A beat signal with a frequency equal to the spacing of these two wavelengths is generated at the output of the photodetector. In addition, the phases of the two laser sources can be locked to generate a signal with low phase noise and high stability. In the second method, microwave signals are created with an external modulation technique. The external modulator can be either an electrooptic intensity modulator or a phase modulator. For high-speed operation, a frequency-doubled or -quadrupled electrical signal can be optically generated by biasing the intensity modulator to suppress the even-order optical sidebands [22].

The frequency response and power handling capability of photodiodes are essential performance parameters in these systems because they determine the speed and RF power of the output signal. Further, post amplification using a low-noise amplifier can be eliminated if the photodiode can handle high power. Therefore, developing a high-power and high-speed photodiode is desirable to meet these requirements.

1.2 Optical Generation of Pulsed Microwave Signal

There have been numerous papers devoted to the generation of CW microwave signals based on optical heterodyne and external modulation [23-25]. Analog photonic links also need to be able to generate high-power pulsed RF signals, especially for radar and wireless applications [26]. The X (8-12 GHz), Ku (12-18 GHz) and K (18-27 GHz) frequency bands are important and widely used for navigation, microwave communications and remote sensing [27]. Photonics-based RF waveform generation and RF detection architecture in a radar system is illustrated in Figure 1-2.

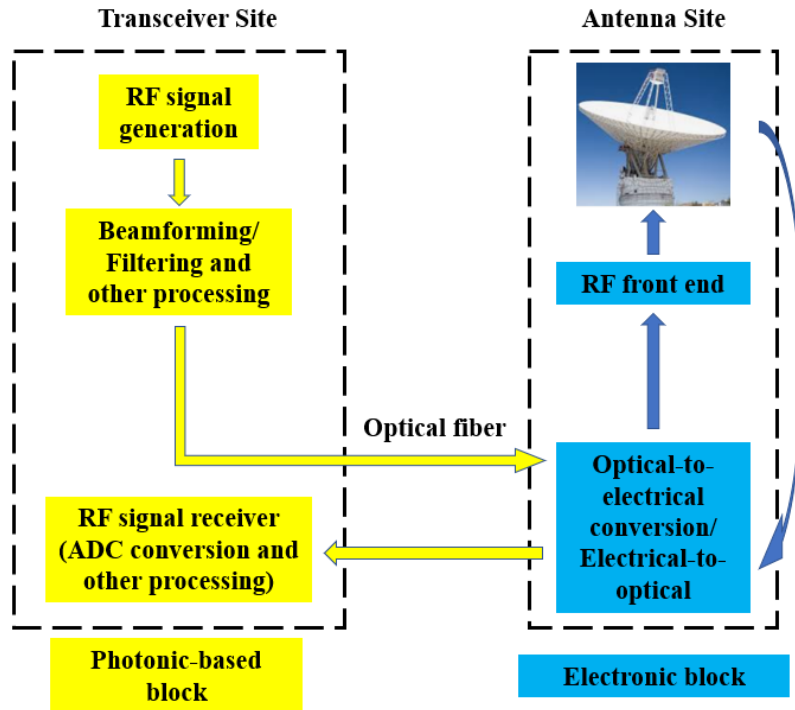


Figure 1-2. Microwave photonics in a radar system.

Pulsed microwave signals can be generated electrically using either analog or digital electronics, but the frequency is usually limited to several gigahertz [28]. Optical techniques are well suited to generate pulsed RF signals with high frequency and low noise. Figure 1-3 shows a proposed architecture using a single pulsed laser to generate tunable radar signals and receive their echoes [29]. The performance of the fully photonics-based coherent radar exceeds state-of-the-art electronics at carrier frequencies above 2 GHz.

There is another simple way to generate phase-locked laser lines with mode locked lasers [30]. The intrinsic phase-locking condition ensures RF signal generation with extremely low phase noise. In addition, it has been reported that spatial light modulator (SLM)-based pulse shaping techniques can be a promising solution for the generation of high-frequency arbitrary RF waveforms [31]. However, the system is bulky and complicated. The frequency-to-time mapping method is also promising for arbitrary waveform generation [32]. However, the pulse rate and pulse duration are

not flexible. In our work, we have demonstrated photonic generation of high-power pulsed microwave signals using a dual- MZM setup.

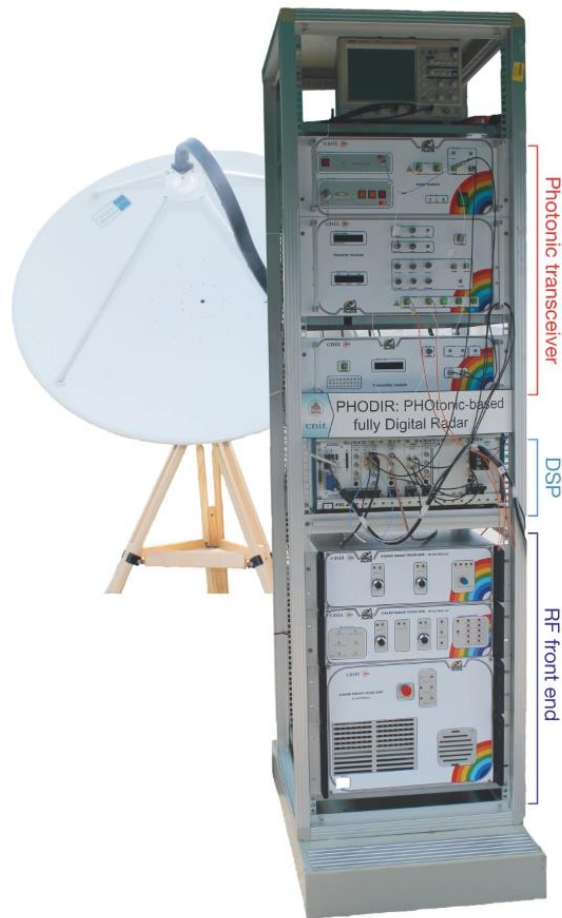


Figure 1-3. A picture of the field-trial demonstrator. DSP, digital signal processor.

To realize long detection distance and high resolution of radars, it is important to generate high-power pulsed RF signals. The photodiode is the key component to meet these requirements since it is the key device that determines the peak power of the entire system. For high-power performance, a higher bias voltage is required in order to mitigate saturation. Therefore, at the receiver side, a photodiode that has high avalanche breakdown voltage and good power handling ability is beneficial for the signal generation.

1.3 Analog Optic Link

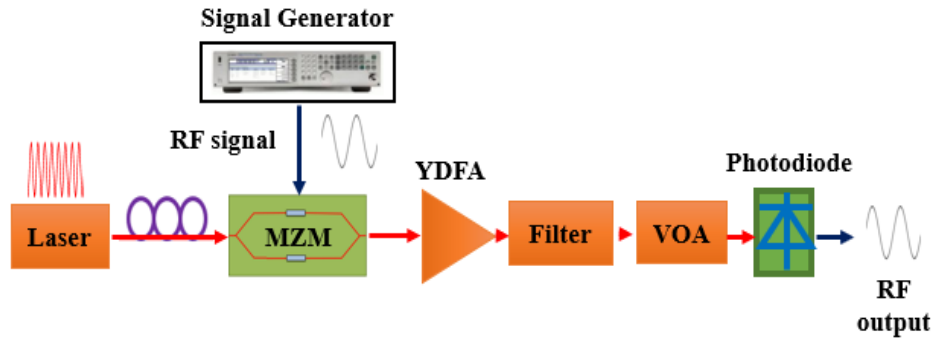


Figure 1-4. Schematic diagram of analog photonic link.

Since the invention of fibers, fiber optical links have transformed the telecommunication industry. Over many years of development, fiber optics have become the dominate choice for ethernet backbone infrastructure, high-speed internet services and networking [33]. Compared to electronic approaches, analog photonic links offer large transmission distances in radar applications, broad bandwidth in signal-processing and reduced size and weight in numerous military platforms [34]. In addition, fiber as a transmission medium offers immunity to electromagnetic interference and electrical isolation [35]. As shown in Figure 1-4, the simplest analog photonic link consists of transmitter, transmission medium (optical fiber) and receiver. The RF signal is applied to the optical signal by an E-O modulator. After the transmission, the photodetector is used to convert the optical signal back to the electrical format for further processing.

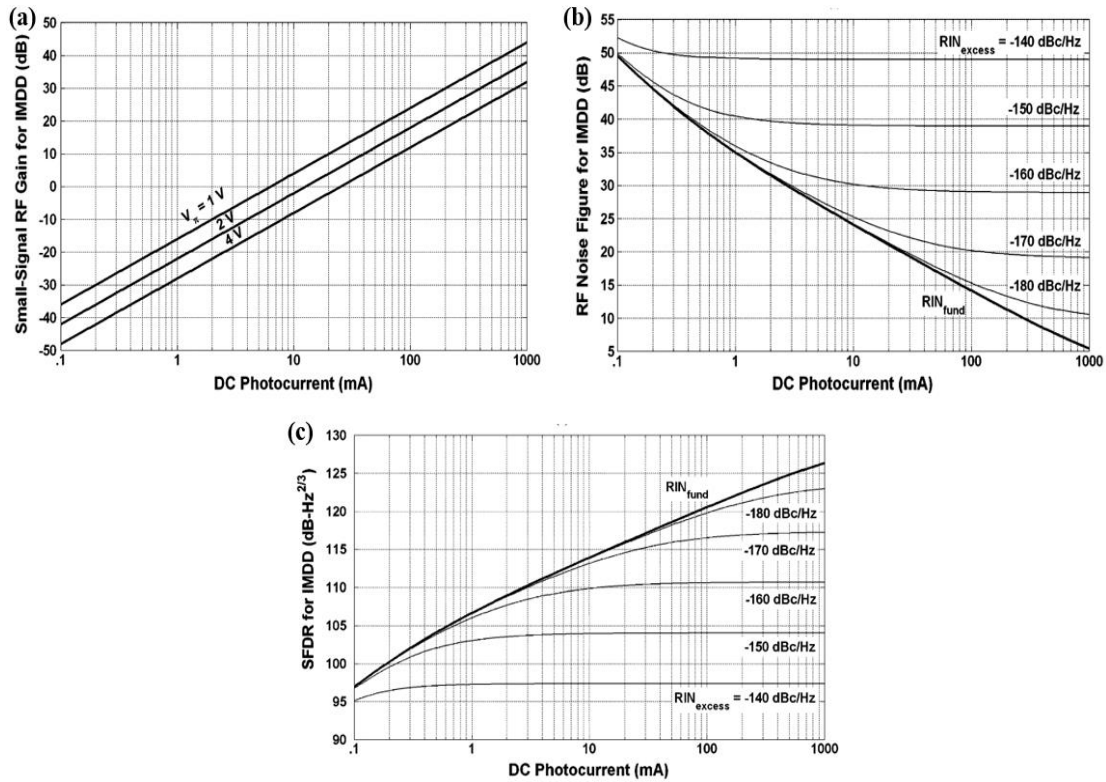


Figure 1-5. Calculated (a) RF link gain, (b) RF noise figure and (c) SFDR as a function of DC current.

For an analog link, the link performance is typically characterized by three key parameters: link gain, noise figure and dynamic range [36]. Link gain is the power transfer of the link. Noise figure characterizes the signal-to-noise ratio degradation and dynamic range describes the power range of the RF signal when the distortions are below the noise floor. Intensity modulation with direct detection (IM/DD) using an external optical intensity modulator is a straightforward approach and has been widely investigated. Owing to the low loss of fiber, the link performance primarily depends on the characteristics of the laser, modulator and photodiode. A high-power laser with low noise and a modulator with low modulation voltage are desirable at the transmitter. At the receiver side, with high optical power received by the photodiode, high RF power is generated. Figure 1-5 shows that link gain increases with increasing photocurrent. Similarly, noise figure decreases and dynamic range increases with increasing photocurrent. It can be shown that

the small-signal gain for the IM/DD link is proportional to the square of the DC photocurrent and inversely proportional to the square of the modulation voltage of the modulator [36].

Apart from 1550 nm, the wavelength 1064 nm has been chosen as another optimal operating wavelength for photonic link as a result of the availability of high-power and ultra-stable lasers at that wavelength [37, 38]. In addition, the Ytterbium-doped fiber amplifiers (YDFA) can boost the optical signal, providing the potential to develop a high-power photonic link [39, 40]. However, to date, there have been few reports of links that operate at 1064 nm. One focus of my work was to demonstrate a high-performance link utilizing high-power and high-linearity photodiodes at that wavelength.

However, with the increase of photocurrent, APLs will be limited by relative intensity noise (RIN) of the laser and amplified spontaneous emission (ASE) noise of optical amplifier [41, 42]. To address these issues, I designed balanced photodetectors because balanced detection provides cancellation of common mode noise [43, 44]. In addition, balanced detection can double the optical power handling capacity of a photonic link.

1.4 Dissertation Organization

This work focuses on demonstration of high-power and high-speed photodiodes and their performance in photonic links. To the best of my knowledge, this Ph.D work has achieved the following records:

- Flip-chip-bonded-on-diamond InP/InGaAs CC-MUTC photodiode with record RF output power in the frequency range from 30 GHz to 50 GHz
- Photonic generation of high-power pulsed RF signal with > 26 W peak power level
- CC-MUTC photodiode with record peak voltage
- First high-speed and high-linearity photodiode designed for 1064 nm

- Balanced photodiodes with the highest reported output power in frequency range from 25 GHz to 40 GHz
- First demonstration of low-bias and balanced analog photonic links at 1064 nm

Chapter 2 introduces the fundamentals of high-power photodiodes and fabrication processes. Chapter 3 describes the realization of MUTC photodiodes with record RF output power in the V band. Chapter 4 describes the photonic generation of high-power pulsed microwave signals. Chapter 5 presents high-power and high-linearity photodiodes at 1064 nm. Chapter 6 demonstrates balanced photodiodes and analog photonic link at 1064 nm. Chapter 7 is the summary and future work.

Chapter 2 Fundamentals of Photodiodes

2.1 Figures of Merit of Photodiodes

2.1.1 Responsivity

The responsivity relates the fraction of photons that can produce detected carriers. The responsivity of the photodiode is defined as the ratio of generated photocurrent to the incident optical power and can be expressed as:

$$R = \frac{I_p}{P} \quad (2.1)$$

where I_p and P are the photo-generated current and incident optical power.

The external quantum efficiency η is defined as the ratio of the number of photo-generated carriers to the number of incident photons. External quantum efficiency depends on the reflectivity at the surface, the absorption layer thickness and the absorption coefficient of the material. It can be express as:

$$\eta = (1 - \rho)[1 - e^{-\alpha(\lambda)L}] \quad (2.2)$$

where ρ characterizes the surface reflectivity, α represents absorption coefficient of the material and L is the thickness of the absorption layer. It can be observed quantum efficiency is improved with a thicker absorption layer for a certain absorption material. The relationship between responsivity and the external quantum efficiency is [45]:

$$R = \eta \frac{\lambda q}{hc} \quad (2.3)$$

where λ , q , h and c are the optical wavelength, elementary charge, Planck constant and speed of light, respectively.

For surface-illuminated photodiodes, the reflection loss is primarily due to reflection at the

air/semiconductor interface. When light travels from a material with refractive index n_1 to a material with refractive index n_2 , the reflection is given by the following relation:

$$\rho = \frac{(n_1 - n_2)^2}{(n_1 + n_2)^2}. \quad (2.4)$$

For InP substrate ($n_1=3.5$), the reflection loss at 1550 nm is approximately 31 %. To reduce the reflection loss, an anti-reflection (AR) coatings can be deposited. Typically, a $\lambda/4$ -thick anti-reflection coating is adopted. The reflection at normal-incident with a quarter wavelength coating of refractive index n_0 can be expressed as [46]:

$$\rho = \frac{(n_1 - \frac{n_0^2}{n_2})^2}{(n_1 + \frac{n_0^2}{n_2})^2}. \quad (2.5)$$

For InP substrate, SiO_2 ($n_0 = 1.44$) is widely adopted as the coating material because it has refractive index close to the optimal value of $\sqrt{n_1 n_2}$ and it is easy to deposit. If $\lambda/4$ -thick SiO_2 is deposited, the ideal reflectivity is 8 %. To further decrease the reflectivity, a double or multi-layer anti-reflection coating can be used as shown in [47, 48].

2.1.2 Bandwidth

The frequency response of reverse biased photodiodes is similar to that of a low pass filter. Bandwidth is used to characterize how fast the photodiodes can operate. The 3 dB bandwidth is defined as the frequency where the RF output power decreases by 3 dB from the value at low frequency. The bandwidth of the photodiode is primarily limited by the carrier transit time and the resistance-capacitance (RC) response time [49].

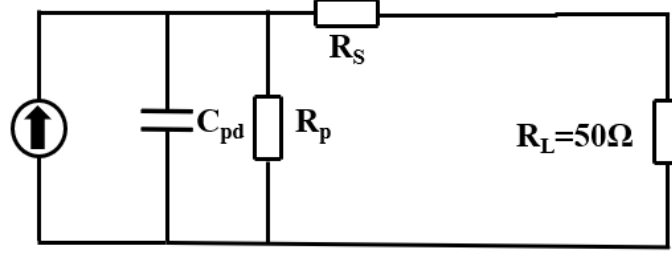


Figure 2-1. Simplified circuit of photodiode

The simplified equivalent circuit of photodiode is shown in Figure 2-1. The C_{pd} , R_s , R_p , and R_L parameters represent the junction capacitance, series resistance, junction resistance and load resistances, respectively. Based on that, the RC time bandwidth f_{RC} can be expressed as:

$$f_{RC} = \frac{1}{2\pi C_{pd}(R_s + R_L)}. \quad (2.6)$$

The junction capacitance, C_{pd} is estimated using the expression:

$$C_{pd} = \frac{\epsilon_0 \epsilon_r A}{d} \quad (2.7)$$

where A is the photodiode junction area and d is the depletion region width. To achieve high speed, we can reduce the capacitance and the series resistance of the photodiode. C_{pd} is typically the dominate factor for the RC-limited bandwidth if the photodiode internal resistance is not comparable to the load. A smaller mesa size and thicker depletion region yield lower capacitance.

The RC-limited bandwidth can be further improved by incorporating an inductor in a photodiode circuit. For an RLC circuit, the current-related relative transfer function to the load can be written as:

$$H_{RLC}(\omega) = \frac{1}{1 - \omega^2 LC_{pd} + i\omega C_{pd}(R_s + R_L)} \quad (2.8)$$

where L refers to the inductance. From this equation, it can be seen that $H'_{RLC}(f) = 0$ at the resonance frequency of $f = \frac{1}{2\pi\sqrt{LC_{pd}}}$. This effect is called inductive peaking [50] and can be used

to significantly improve the 3 dB bandwidth. Above the 3 dB bandwidth, the RF output power

drops more rapidly with increasing frequency. The power output from the RLC circuit drops at 40 dB/dec compared with 20 dB/dec for the RC circuit. The optimum inductance to achieve a maximized RLC-limited 3 dB bandwidth can be derived as:

$$L = \frac{C_{pd}(R_S+R_L)}{2} \quad (2.9)$$

Figure 2-2 shows simulated bandwidth of RC and RLC circuit frequency responses for a 40 μm -diameter photodiode. The capacitance is 150 fF and the optimal inductance is 400 pH. From the curves, the RLC circuit with 19 GHz 3dB bandwidth shows 45 % improvement compared with RC circuit with 13 GHz bandwidth.

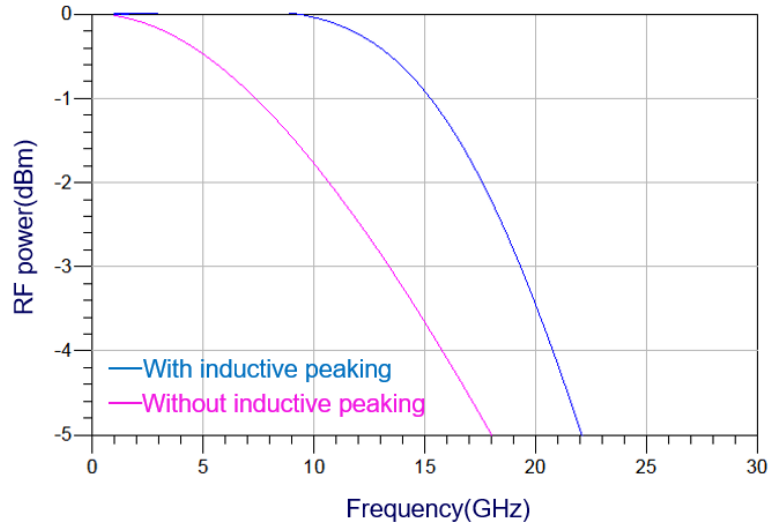


Figure 2-2. Simulated bandwidth of photodiode with and without an inductor

Since it is impractical to use a lumped inductance at high frequency, a short section of a transmission line with a large characteristic impedance can be treated as a series inductor. The input impedance Z_{in} for a short transmission line with a load can be expressed as [51]:

$$Z_{in} = Z_0 \frac{Z_L + jZ_0 \tan \beta l}{Z_0 + jZ_L \tan \beta l} \quad (2.10)$$

where Z_0 is the characteristic impedance of the transmission line, Z_L is the load impedance and βl is the electrical length. When the electrical length is smaller than $\pi/4$ and characteristic impedance of the transmission line is high. Equation 2.10 can be simplified as:

$$Z_{in} \approx Z_L + jZ_0\beta l = Z_L + j\omega L \quad (2.11)$$

where L is the equivalent inductance of the high impedance transmission line. By incorporating a high impedance transmission line in the coplanar waveguide (CPW), the device frequency response can be dramatically enhanced.

The carrier transit time is the time required for the photo-generated electrons and holes to be collected by the metal contacts after generation in the absorption layers. For a PIN structure, the holes determine the transit-time-limited bandwidth because their saturation velocity is much lower than that of electrons.

The transit-time-limited bandwidth can be improved by the UTC structure since only electrons need to travel through the whole junction. The transit-time-limited bandwidth of a UTC photodiode can be approximated as [52]:

$$f_{tr} = \frac{W_A^2}{2D_e} + \frac{W_A}{v_{th}} + \frac{W_D}{v_e} \quad (2.12)$$

where W_A , W_D , D_e , v_{th} and v_e represent the absorption width, drift layer width, electron diffusion coefficient, thermotic emission velocity and electron velocity, respectively. The transit time includes the diffusion time in the absorption layer and drift time in drift layer.

Assuming the transit-time-limited and RC-time-limited bandwidth have Gaussian responses, the overall 3 dB bandwidth, f_{3dB} , can be approximated as [49]:

$$f_{3dB} = \frac{1}{\sqrt{\frac{1}{f_{tr}^2} + \frac{1}{f_{RC}^2}}} \quad (2.13)$$

2.1.3 Output RF Power

RF output power is the amount of AC power delivered to the load. Typically, the output power will increase quadratically with the photocurrent before it saturates. The RF compression is defined as the deviation of the measured RF output power from the ideal linear output. The RF saturation

power is usually adopted to characterize the photodiode and is defined as the point where the RF compression drops by 1 dB from its peak value.

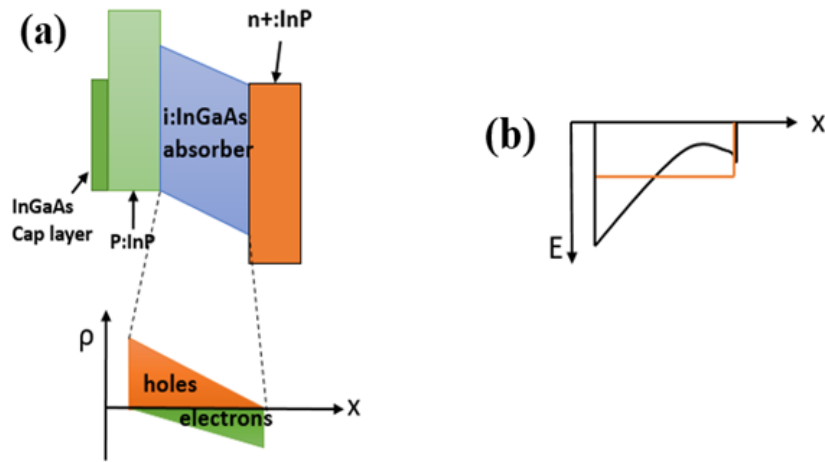


Figure 2-3. (a) Band diagram, carrier concentration and (b) electric field of PIN photodiodes

One of the important limiting factors to achieve high RF power levels is the space charge effect, which results from charge screening in the depletion region. Figure. 2-3 shows the carrier distribution in a PIN photodiode under high level illumination. When the light is absorbed in the intrinsic region, electron and hole pairs are generated and they drift toward the anode and cathode. As the optical power increases, the excess charges accumulate near the edges of the depletion region, due to the limited velocity of carriers, and create an electric field that opposes bias. Therefore, the electric field is distorted by these charges. The space charge field will increase with photocurrent. This will cause the total field to collapse. As shown in Figure 2-4, the carriers cannot maintain saturation velocity at low field [53]. A low carrier velocity will cause a drop in the output RF power of the photodetector. It can also be observed that holes are the primary limitation since holes have a much slower velocity.

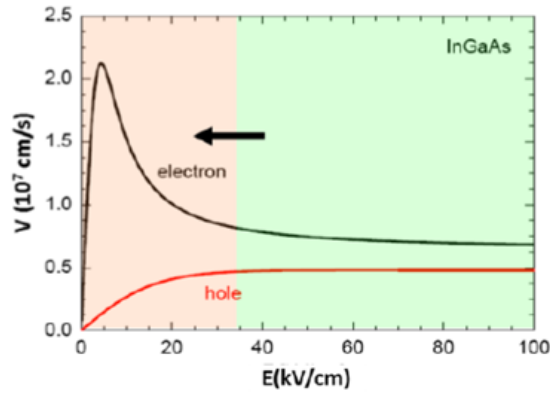


Figure 2-4. Velocity of electrons and holes in InGaAs [53].

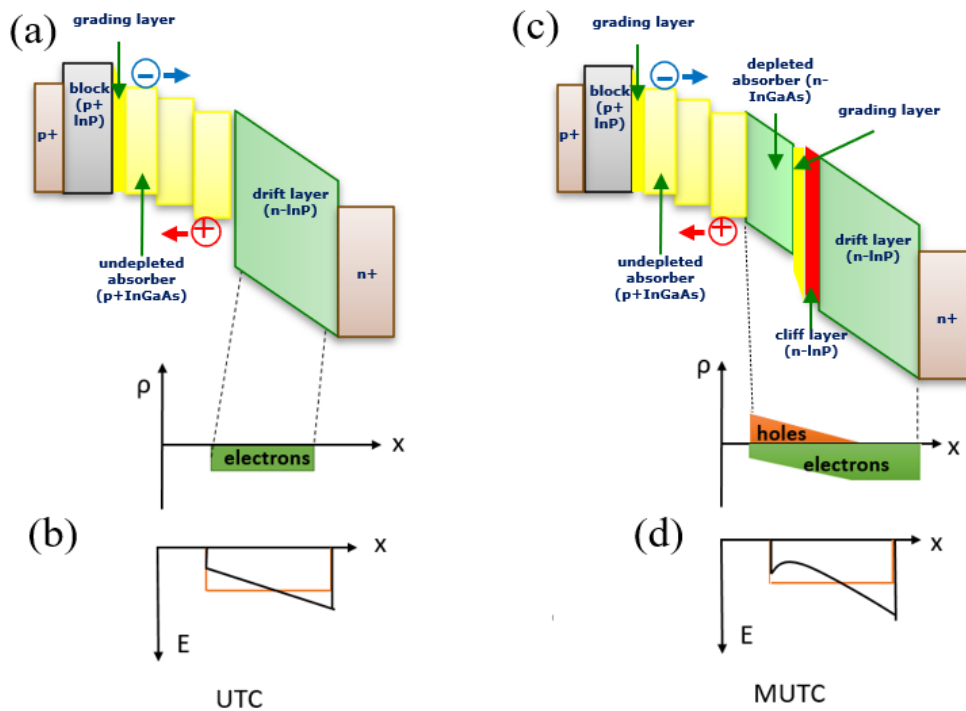


Figure 2-5. (a) Band diagram, carrier concentration, (b) electric field of UTC photodiodes and (c) band diagram, carrier concentration, (d) electric field of MUTC photodiodes

Mitigated space charge and improved performance have been achieved with the UTC photodiode, demonstrated by Ishibashi in 1997 [54]. It should be mentioned that the undepleted absorber in the UTC structure utilizes graded doping to generate a quasi-electric field to assist carrier transport. Since only electrons need to travel through the whole junction, the balance

between electrons and holes transit time can be achieved with dedicated design. The excess hole density in the absorption layer decays quickly with the dielectric relaxation time. Since electrons have higher velocity, less carriers accumulate in the drift layer and the space charge effect is mitigated.

The performance of UTC photodiodes has been further improved with the MUTC photodiode as shown in Figures 2-5 (c) and (d) [55]. By incorporating a depleted InGaAs absorption layer with suitable thickness, the responsivity of the photodiodes can be increased without sacrificing bandwidth [56]. A cliff layer is inserted to adjust the electric field in the depleted region. The drift layer is pre-distorted to partially compensate the electric field collapse caused by the space charge effect under high optical illumination [57]. At the heterojunction interface, the grading layers are inserted to smooth the bandgap discontinuity which further mitigates the charge accumulation [58].

Another factor that limits the output power of a photodiode is heat dissipation. As discussed above, the electric field in the depletion region should be high enough to guarantee that the photogenerated electrons and holes travel at saturation velocity. Therefore, the simplest method to mitigate the space charge effect is to increase the bias voltage on the photodiode and thus increase the electric field across depletion region. However, the high electric field in the depletion region is the source of most of the heat generation in a photodiode. The poor thermal conductivity of InGaAs absorption layer ($0.05 \text{ W} \cdot \text{cm}^{-1} \cdot \text{K}^{-1}$) impedes heat transfer from the absorption layer to the drift layer and the InP substrate layer [59]. As a result, the device junction temperature increases as the optical input increases.

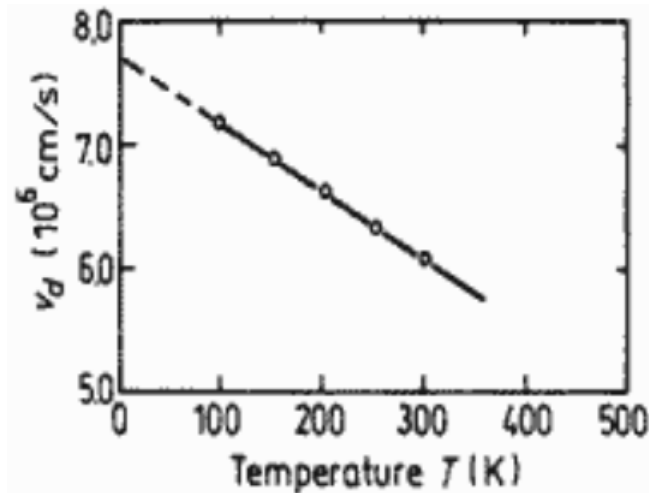


Figure 2-6. Electron saturation velocity versus temperature for InGaAs [60].

As the Figure 2-6 shows, the electron saturation velocity decreases as temperature increases [60]. Therefore, the frequency response and RF output power will degrade at high-power level.

In addition, an increase in junction temperature results in the reduction of the energy bandgap of InGaAs [61]. As a result, the dark current of the junction will increase and lead to further increase in the junction temperature. Since the photodiode has a certain heat dissipation ability, the cycle of reduced bandgap causing more absorption and heat generation which further reduces the bandgap with more heat generation can kill the device.

A flip-chip bonding technique is adopted to improve thermal dissipation [62-64]. It has been shown that higher saturation current and RF output power can be achieved by flip-chip bonding to high-thermal-conductivity substrates. Gold pillars are plated on the mesa and the coplanar waveguide contact pads are grown on a high-thermal-conductivity submount. Gold is chosen as the bonding material because it can be joined at temperatures below its melting point and it provides good electrical conductance. A 3D illustration of the flip-chip bonding process is illustrated in Figure 2.7. A bonding machine from FINETECH is used to flip-chip bond the chips onto the submount. During the process, the Au-Au bond is formed with 2~5 N force at 340 °C by

the thermocompression process. For characterization, these photodiodes can be contacted through the metal RF pads on the submount.

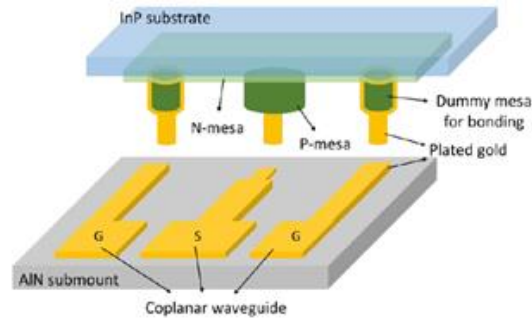


Figure 2-7. 3D view of flip-chip bonding process.

2.1.4 Linearity

Linearity describes the distortion of the output signal. The photodiode nonlinearity directly affects the spurious free dynamic range of an analog optic link [65]. It has been reported that the nonlinear behavior of photodiodes results from many physical mechanisms, including carrier velocity modulation [66], nonlinear capacitance [67, 68], nonlinear resistance [69], and nonlinear responsivity [70]. In addition, device heating [71] and circuit loading effects are also capable of producing nonlinear response. Nonlinearity study is a complicated task because most of these mechanisms are interrelated.

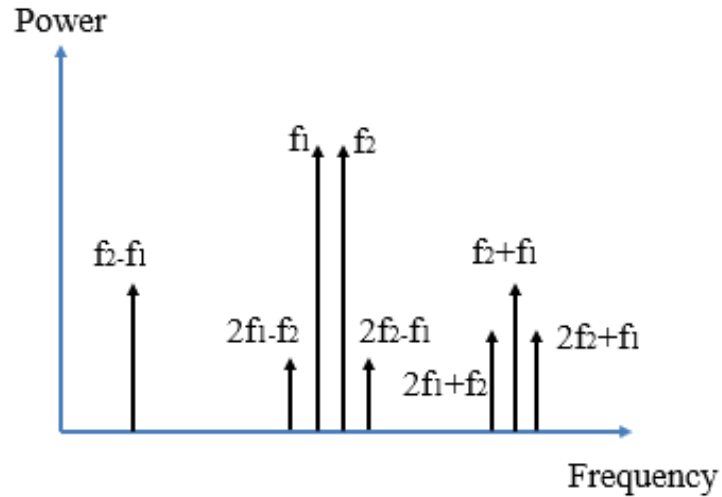


Figure 2-8. Frequency spectrum of a nonlinear system.

When two intensity-modulated light sources are incident on the photodiode, there should be only two fundamental frequencies at the output for a linear system. In the frequency domain, second and third-order distortions excited by two input signals are shown in Figure 2-8. Typically, the third-order intermodulation distortion (IMD3) is considered as the most troublesome for sub-octave systems. This is due to the fact that the IMD3s are the largest nonlinear distortion products that fall in the vicinity of the fundamental frequencies or the passband of the system [41]. They increase with input power three times faster than the signal if there is no linear processing.

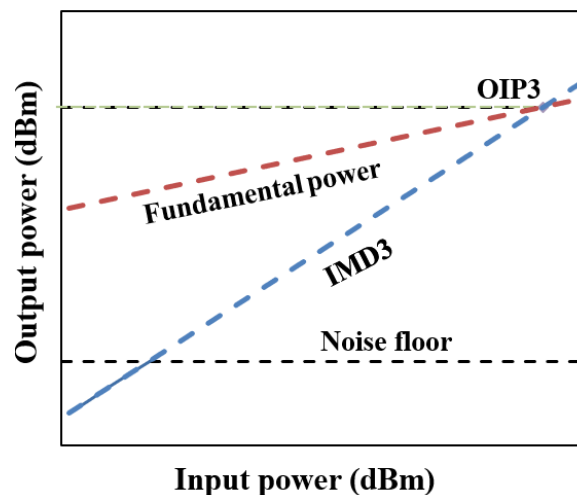


Figure 2-9. Definition of OIP3.

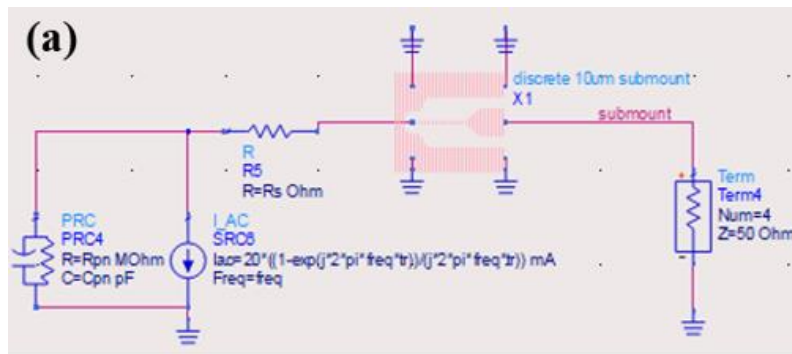
The output third-order intercept point is the figure of merit to characterize nonlinear systems [72]. From the Figure 2-9, the red line is the output power at the fundamental frequency and the blue line is that of IMD3. Output power at the fundamental frequency versus input power increases with a slope of 1 while the IMD3 increases with a slope of 3. The intercept power of a linear extrapolations of these two lines is defined as the OIP3. In the weakly nonlinear region, the OIP3 can be calculated by the following:

$$OIP_3 = P_f + \frac{1}{2}(P_f - P_{IMD3}) \quad (2.14)$$

where P_f is the power of fundamental frequency and P_{IMD3} is the power of the IMD3, both in units of dBm. The photodiode linearity will be studied in Chapter 5.

2.1.5 S-Parameter

Scattering parameters (S-Parameters) are used to describe the relationship between different ports. For photodiodes, the commonly used S-parameter is S_{11} , which is the ratio of the reflected wave to incident wave at the RF output port [73, 74].



(b)

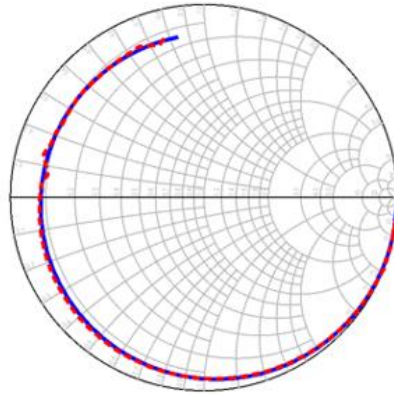


Figure 2-10. (a) Equivalent circuit in Keysight ADS software; (b) measured and fitting S parameter.

The parameters can be extracted from the fitting of S_{11} based on the equivalent circuit of the photodiode. Figure 2-10 (a) shows the circuit model in Keysight Advanced Design System (ADS) software. Both the RC equivalent circuit and coplanar waveguide pads are included. During the fitting process, the value of resistance, inductance and capacitance of the photodiodes are tuned to make the simulated S_{11} curve coincide with the measured S_{11} curves. As shown in Figure 2-10 (b), the blue curve is the simulated S_{11} and the red curve is the measured result. They agree well in the frequency range from 100 MHz to 67 GHz.

2.2 Fabrication Process Flow

The fabrication process for the MUTC photodiodes is described in this section. The cross section of a back-illuminated photodiode is demonstrated in Figure 2-11(a). The photodiodes are fabricated using a double mesa structure. The first mesa stops at the n-contact layer to define the p-mesa. The second mesa etches into the semi-insulating InP substrate. SiO_2 is deposited on the sidewall of the mesa as a passivation layer to reduce surface leakage current. Figure 2.11 (b) shows the fabrication process flow, which will be described step by step.

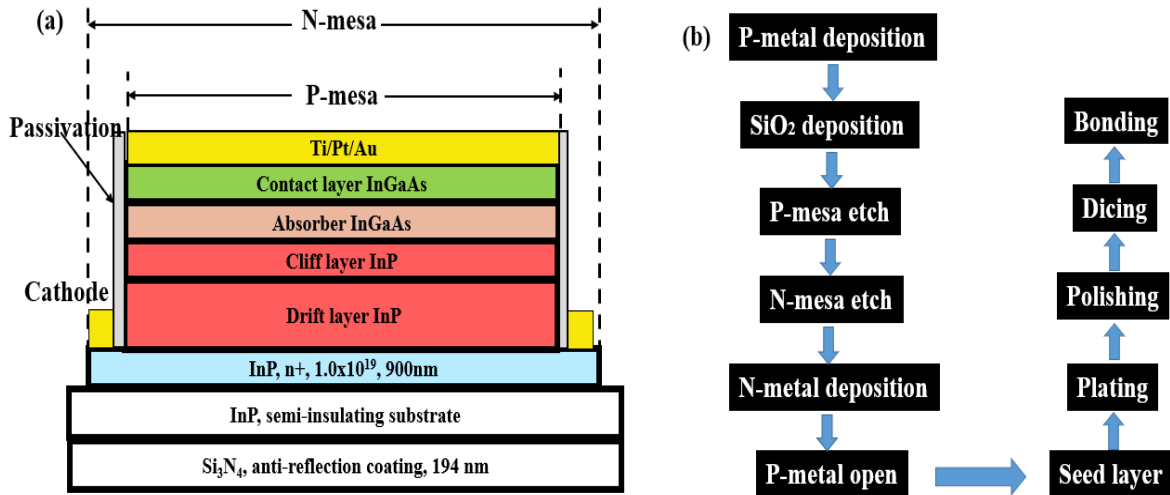


Figure 2-11. (a) Cross section of surface-illuminated photodiode; (b) fabrication process flow.

2.2.1 P-metallization

The first fabrication step is p-metal deposition on the top of the photodiode. For high-speed design, a low contact resistance is always required to achieve a low RC time constant. For our MUTC photodiode, we adopt metal layer stacks of Ti/Pt/Au/Ti (10/10/80/10 nm) on the p-type InGaAs contact layer. Titanium is used for adhesion to the InGaAs surface layer and the platinum layer prevents gold migration into the semiconductor [75]. The gold provides a good electrical conductance.

Before fabrication, the wafer is cleaned with Acetone/IPA and O_2 plasma to remove particles and contaminants. The metal stack is deposited using E-beam evaporation. The deposition is carried out at vacuum level below 10^{-6} Torr.

2.2.2 P-mesa Etch

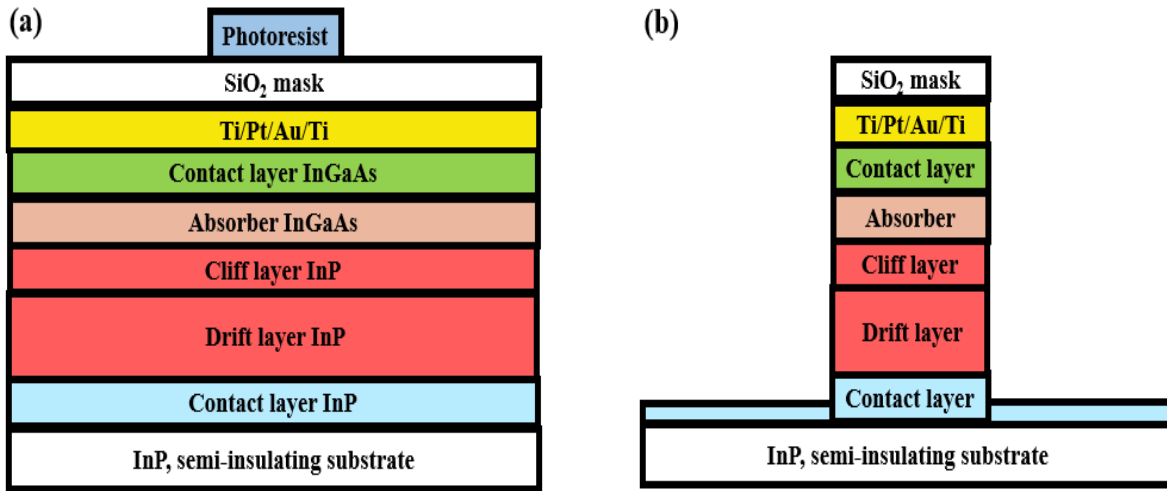


Figure 2-12. Schematic cross section of (a) patterned photoresist and (b) p-mesa.

The p-mesa etch step is shown in Figure 2-12. Wet etch, dry etch, or a combination can be used to form the p-mesa. The wet etch method can achieve a smooth sidewall, and thus result in lower dark current due to less surface leakage. However, it will lead to lateral undercutting because the wet etch is isotropic. For our high-speed photodiodes fabrication, we adopt reactive ion etch (RIE) and inductively coupled plasma (ICP) etch to eliminate the undercut issue.

At first, the SiO₂ is deposited on top of the p-metal using plasma-enhanced chemical vapor deposition (PECVD) as a hard mask since the etch rate is stable and easy to control. During lithography, HMDS and AZ 5214 photoresist are spun on the wafers with thickness of 1.5 μm and pre-baked at 100 °C for 2 min before exposure. Then, a Karl Suss MJB4 is used as a contact lithography tool for exposure with equivalent dose of 170 mJ/cm². The wafer is developed in AZ 300 MIF developer for 30 s. The hard mask etch is done using an Oxford RIE machine with CHF₃ gas. The pattern of the photoresist transfers to the SiO₂ after this etch. After cleaning with O₂ plasma to remove the residual photoresist on top of the SiO₂, the wafer is put back in the Oxford

for further etching. In our experiments, a recipe with $\text{Cl}_2:\text{N}_2$ gas mixture is used to etch III-V materials with a 150 W RF power and 1000 W ICP power. We also prepare a dummy SiO_2 wafer in the chamber to monitor how much of the SiO_2 is etched at the same time. The step height of the mesa and oxide can be determined by a profilometer. In this way, we can precisely control how much III-V we etch away. The wafer is then soaked in bromine: methanol for a few seconds to remove some of the surface damage arising from the dry etch in order to reduce the dark current. It should be noted that the resistance of the final device will be large if the wafer is over-etched.

2.2.3 N-mesa Etch

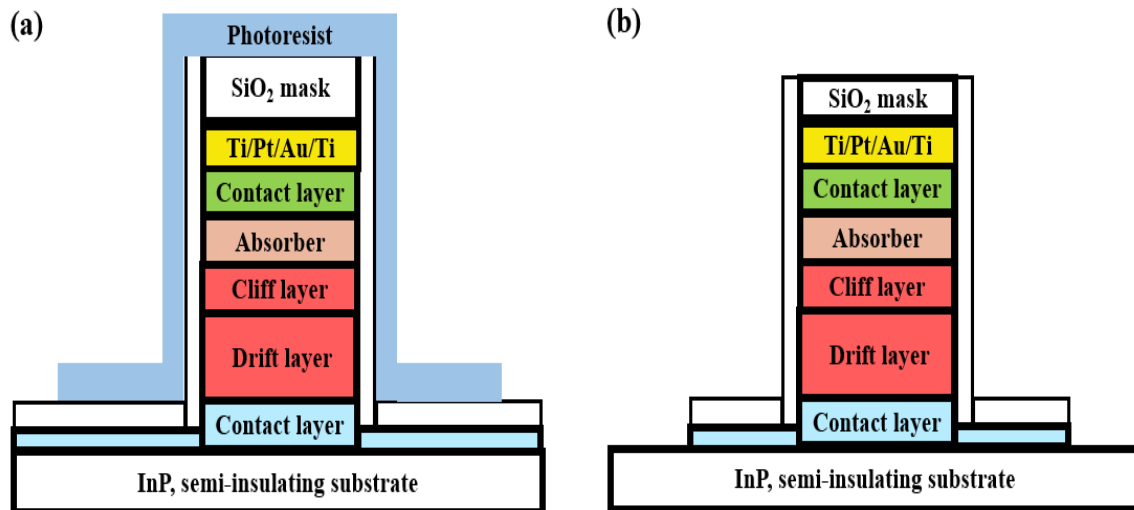


Figure 2-13. Schematic cross section of (a) patterned photoresist and (b) n-mesa.

The n-mesa etch is done after the p-mesa etch. The n-mesa needs to be defined to isolate the discrete devices to each other. The etch should stop at the non-conductive substrate. The RF signal pad should be isolated from the highly doped layer to minimize the RF signal loss. For our flip-chip bonded devices, the isolated n-mesa can reduce the parasitic capacitance due to less overlap between the RF pads and the contact layer.

Like the p-mesa etch, the wafer is cleaned and loaded into the PECVD chamber for another

layer of hard mask. This oxide layer also serves as a passivation layer to passivate dangling bonds and thus reduce the surface leakage current. We use photoresist AZ 5214 for lithography and transfer the pattern to the oxide layer with the RIE etch. The III-V materials are etched with an RIE-ICP recipe. The n-mesa can be over-etched as long as not all of the hard mask is consumed. The n-mesa fabrication process is shown in Figure 2-13.

2.2.4 N-metallization

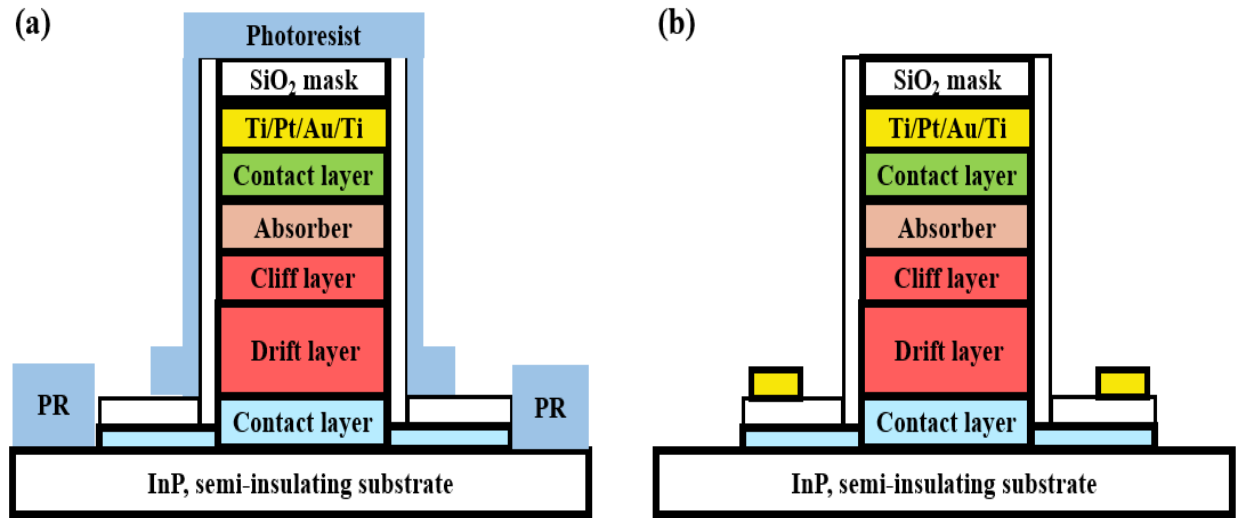


Figure 2-14. Schematic cross section of (a) patterned photoresist and (b) n-metal.

After standard lithography with AZ 5214, the n metal stacks consisting of AuGe/Ni/Au (20/20/80 nm) are deposited by E-beam evaporation as shown in Figure 2-14. The n-contact is then formed by a lift-off procedure.

AuGe/Ni/Au stacks can provide low series resistance and good adhesion on the heavy-doped InP contact layer. During the rapid annealing, AuGe alloy with lower barrier height can be formed and Ge settles in the indium vacancies as a donor, which leads to low resistance [76].

2.2.5 P-contact Open

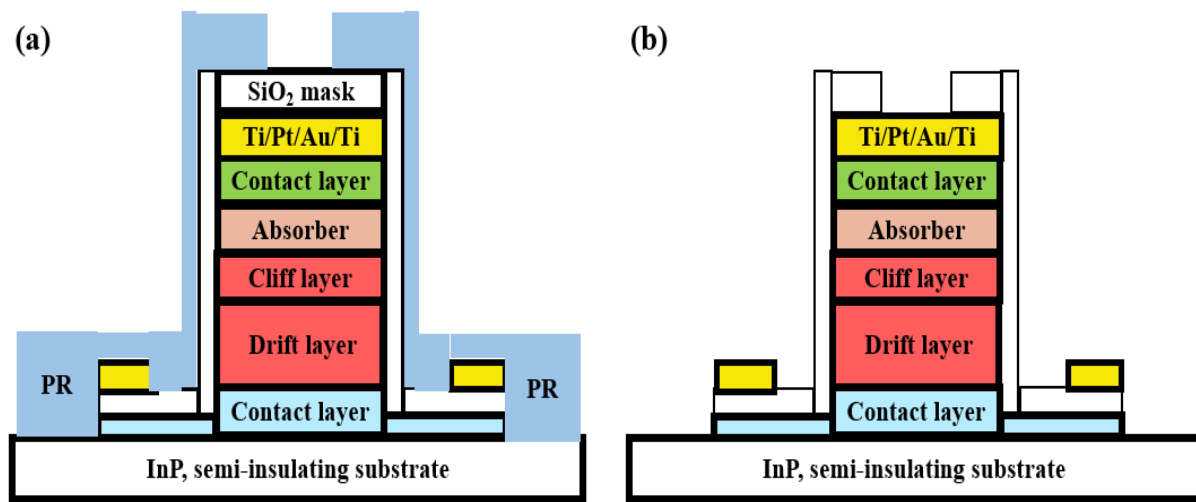


Figure 2-15. Schematic cross section of (a) patterned photoresist and (b) open p-contact.

Following the n-metal deposition, the next step is opening the p-contact. Since there is still a residual hard mask on top of the metal, the SiO₂ layer should be removed to expose the p-metal. The lithography in this step is critical because the contact opening is small for high-speed devices. If the sidewall of the p-mesa is exposed, the protective SiO₂ layer on sidewall will be etched and the metal deposited in the following step will short the device.

The SiO₂ etching is conducted in the Oxford. After etching, the device is ready for current-voltage measurement.

2.2.6 Seed Layer and Electroplating

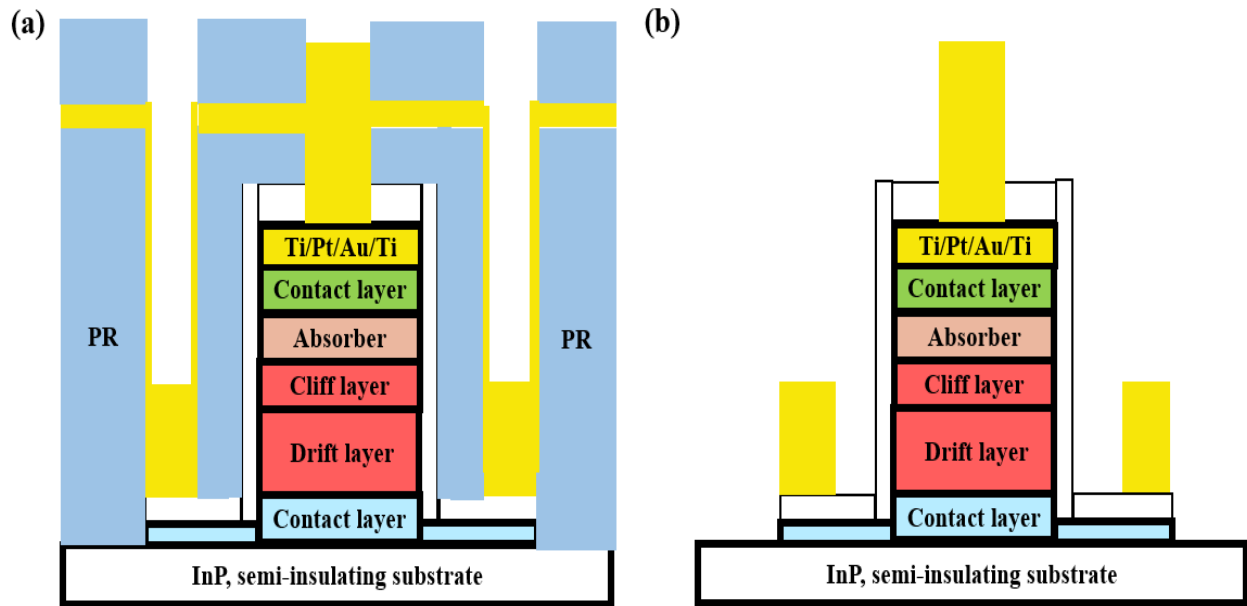


Figure 2-16. Schematic cross section of (a) patterned photoresist and (b) seed layer and electroplating.

The contact layer is only about 100 nm, which is too thin for flip-chip bonding. Thicker gold needs to be plated. As shown in Figure 2-16, two lithography steps are processed in sequence. The first lithography creates 1.5 μm -thick photoresist on top of the p-metal. Then, Ti/Au (10/50 nm) is evaporated as a seed layer. The second lithography is done on top of the first photoresist to open the mesa regions. Then, a gold layer with thickness approximately 2 μm is plated in the open area. The top layer photoresist is removed with O_2 plasma and the seed layer is etched with gold etchant. Finally, lift off is carried out to complete the photodiode fabrication process.

2.2.7 Other Steps

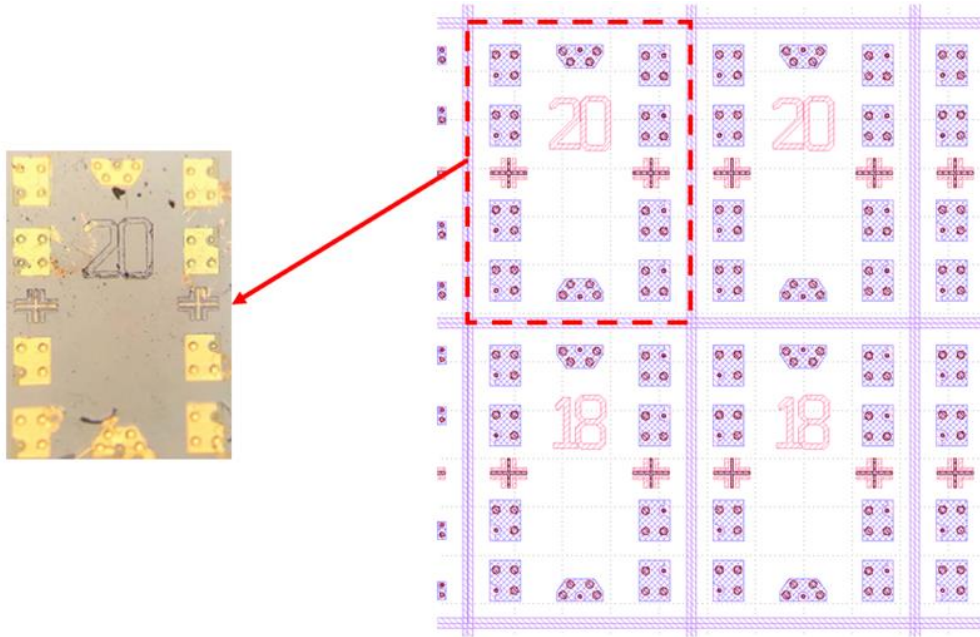


Figure 2-17. Wafer before and after dicing.

After photodiode fabrication, the backside needs to be polished. The purpose of polishing is to remove residues and smooth the backside of the wafer for improved responsivity. This is accomplished using the Logitech polishing machine.

Usually, an anti-reflection coating is deposited on the backside of the wafers to reduce reflection for flip-chip bonded photodiodes. A Si_3N_4 or SiO_2 layer is deposited using PECVD. The thickness of the layer has been discussed in the previous section.

Following the AR coating, the wafer is diced into 1mm x 2mm chips for further flip-chip bonding. As shown in the red box in Figure 2-17, there are two photodiodes and four balanced-photodiode pairs on each die. Typically, a layer of photoresist is spun onto the top surface of the wafer in order to protect the devices from accidental damage during the dicing process.

The last step is to flip-chip bond the diced chips to a submount with RF pads.

Chapter 3 High-Power V-Band Photodiodes Flip-Chip Bonded on Diamond

3.1 Introduction

Photonic generation of millimeter-wave frequencies has numerous advantages [20, 21]. Among them, V-band frequencies ranging from 40 GHz to 75 GHz are of particular interest since the V-band is license free in many countries and is most often used for wireless backhaul and point to point or point to multi-point radio links [77, 78].

As discussed in the previous chapter, high power photodiodes are key components in photonic generation of microwave signals. The space charge effect and thermal failure are two primary limiting factors for generated RF output power. The MUTC structure has been shown to effectively suppress the space charge effect. In an InGaAs/InP MUTC photodiode, carriers are generated in the InGaAs absorption layer. Since only electrons need to travel through the InP drift layer and excess holes quickly decay during the dielectric relaxation time, the effective transit time is shorter than for a PIN structure, which has both electrons and holes in the drift region.

When photodiodes operate at high reverse bias to mitigate the electric field collapse, there is a dramatic increase in heat and thermal-related performance degradation. In order to improve the thermal handling ability, it is beneficial to flip-chip bond the photodiode to a substrate with high thermal conductivity. Initially, photodiodes were flip-chip-bonded on aluminum nitride (AlN) submounts with a thermal conductivity of 285 W/mK [63]. Diamond has a higher thermal conductivity of about 2000 W/mK. Compared with a 50 μm -diameter device on an AlN submount, it has been shown that a device on a diamond submount achieves 80% greater maximum RF output power [64]. In this work, chemical-vapor-deposition (CVD) diamond was used as the submount.

3.2 Device Structure and Simulation

The CC-MUTC photodiodes have achieved better performance than other types of photodetectors with respect to the figures of merit that are important for analog optical links [54]. Therefore, I designed and characterized high-power CC-MUTC photodiodes that operate at V-band and 1550 nm. Figure 3-1 shows the epitaxial structure of the InP/InGaAs wafer. The growth began with n-type doped InP contact layer. 700 nm lightly n-doped drift layer acted as a space-charge compensation layer where the electric field was pre-distorted to achieve a flat electric field profile at high photocurrent [55]. A cliff layer with doping level of 1.6×10^{17} and thickness of 50 nm was used to enhance the electric field in the depleted portion of the absorption layer [79]. Two 15 nm quaternary layers were grown to “smooth” the abrupt conduction band barrier at the InGaAs-InP heterojunction interface between InP and InGaAs. This can prevent electrons from accumulating at the heterojunction interface. The doping in the p-type absorber was “graded” in three steps ($5 \times 10^{17} \text{ cm}^{-3}$, $1.1 \times 10^{18} \text{ cm}^{-3}$, $2 \times 10^{18} \text{ cm}^{-3}$) to create a quasi-field that aids carrier transport. Finally, the two top layers were a 100 nm $2 \times 10^{18} \text{ cm}^{-3}$ p-doped InP electron-blocking layer and a 50 nm heavily p-doped $2 \times 10^{19} \text{ cm}^{-3}$ InGaAs contact layer.

Contact layer InGaAs, p+, Zn, 2×10^{19} , 50nm
InP, p+, Zn, 2×10^{18} , 100nm
Grading InGaAsP, Q1.1, p+, Zn, 2×10^{18} , 15nm
Grading InGaAsP, Q1.4, p+, Zn, 2×10^{18} , 15nm
Un-depleted absorber InGaAs, p+, Zn, 2×10^{18} , 50nm
Un-depleted absorber InGaAs, p+, Zn, 1.1×10^{18} , 50nm
Un-depleted absorber InGaAs, p+, Zn, 5×10^{17} , 50nm
Depleted absorber InGaAs, n-, Si, 1×10^{16} , 200nm
Grading InGaAsP, Q1.4, n-, Si, 1×10^{16} , 15nm
Grading InGaAsP, Q1.1, n-, Si, 1×10^{16} , 15nm
Cliff layer InP, n-, Si, 1.6×10^{17} , 50nm
Drift layer InP, n-, Si, 1×10^{16} , 700nm
InP, n+, Si, 1.0×10^{18} , 100nm
InP, n+, Si, 1.0×10^{19} , 900nm
InP, semi-insulating substrate, Double side polished

Figure 3-1. The epitaxial layer design of InGaAs/InP MUTC.

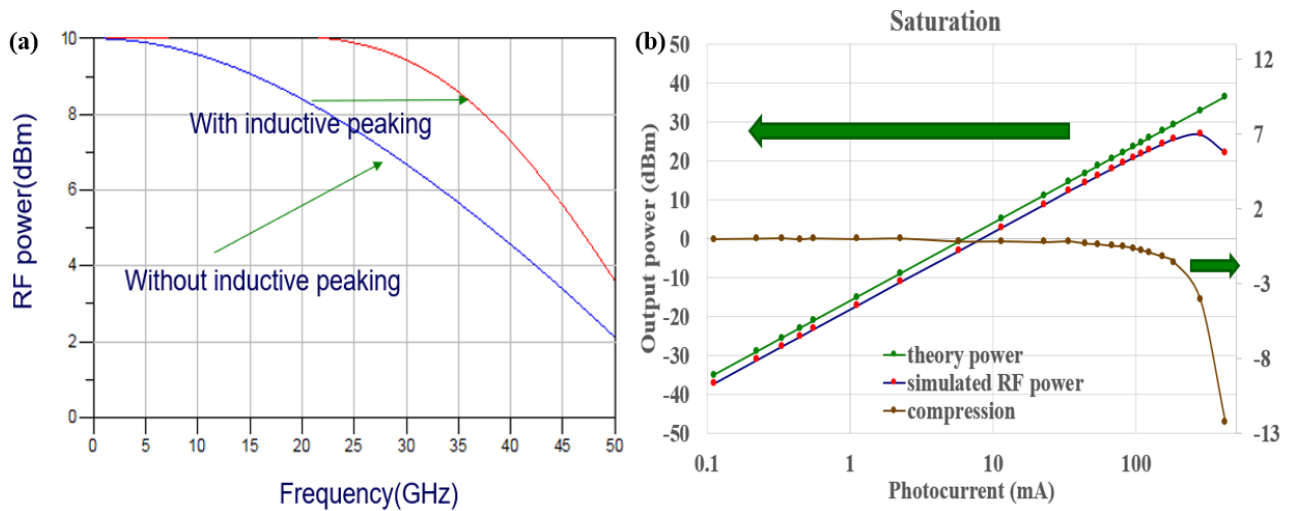


Figure 3-2. Simulations of (a) frequency response and (b) saturation current of 28 μm -diameter photodiodes.

To simulate the bandwidth of the photodiodes, the transit-time limited bandwidth was obtained in Ansys Crosslight. The electron and hole saturation velocities in InP were set as $1.5 \times 10^7 \text{ cm/s}$ and $0.45 \times 10^7 \text{ cm/s}$, respectively. For this epitaxial layer structure, the simulated transit-time limited bandwidth is 48 GHz at -8 V, where the junction is fully depleted. The RC product limitation was calculated based on the equivalent circuit model in the Advanced Design

System. When we took both the transit-time and the RC-time into consideration, the overall simulated bandwidth is shown in Figure. 3-2 (a). As I stated in a previous section, the 3 dB bandwidth can be further enhanced by incorporating a high impedance transmission line. The simulated bandwidth for a 28 μm -diameter device with inductive peaking is 37 GHz, which is 55 % higher compared to the result without peaking. The frequency response is primarily limited by the relatively large RC product.

From the simulated RF power, the 28 μm -diameter device saturates at 160 mA at 40 GHz, where the thermal failure was not taken into consideration. The RF output power increases superlinearly with the photocurrent before it saturates due to the space charge effect.

3.3 Device Fabrication

The MUTC photodiodes were fabricated with diameters from 18 μm to 36 μm . The device was defined with a dry-etched double-mesa procedure. AuGe/Ni/Au and Ti/Pt/Au were deposited as n-metal and p-metal contacts, respectively. Au bonding bumps with a diameter of 12 μm and a height of 2 μm were plated on the p and n contacts. After back-side polishing, a 250 nm-thick SiO_2 anti-reflection coating was deposited as anti-reflection coating at 1.55 μm . In the flip-chip bonding process, a chip with six photodiodes was bonded onto a diamond submount by Au-Au thermo-compression. Through the Au bonding bumps and CPW pads, the Joule heat generated in the junction can be dissipated to the diamond submount.

3.4 Device Characterization



(a)

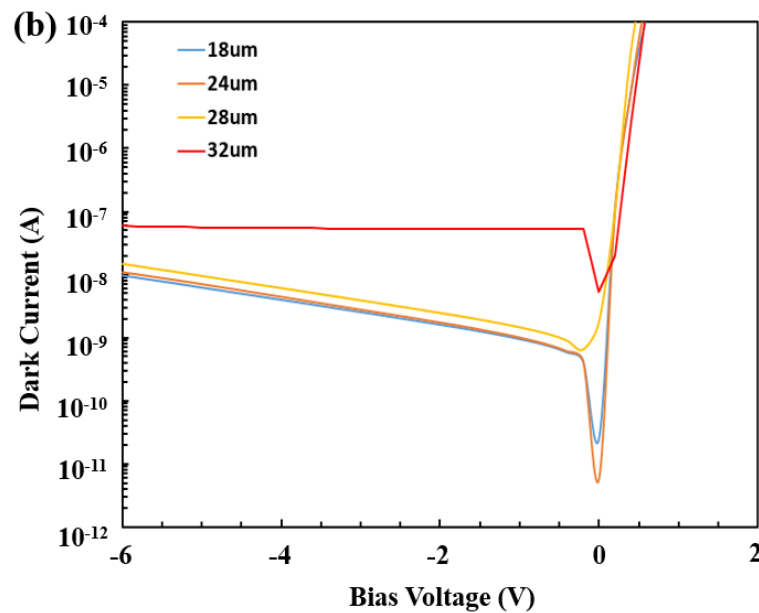


Figure 3-3. (a) Parameter analyzer for IV measurement; (b) dark current versus device diameter at different bias voltage.

The current-voltage (I-V) relationship is one of the important parameters of a diode. The dark current of the photodiode is the current that flows in the diode without light. Low dark current is always preferable for low noise. There are three primary sources of the dark current, generation-recombination inside the depletion region, band-to-band tunneling and surface leakage [80].

The IV curve measurement was carried out with an HP 4156B semiconductor parameter analyzer. The photo response can also be measured with a lamp. The dark current versus bias voltage are shown in Figure. 3-3 (b). Typically, the dark currents are in the range of $10^{-8} \sim 10^{-7}$ A at

-6 V bias.



(a)

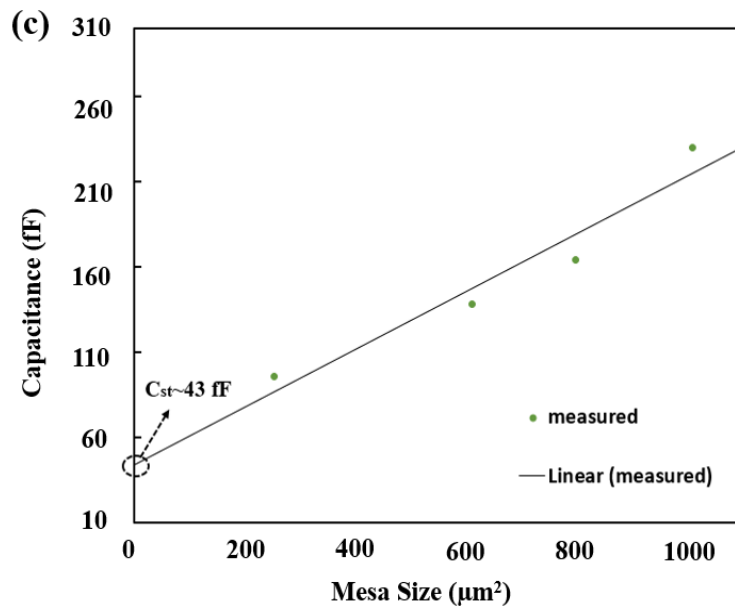
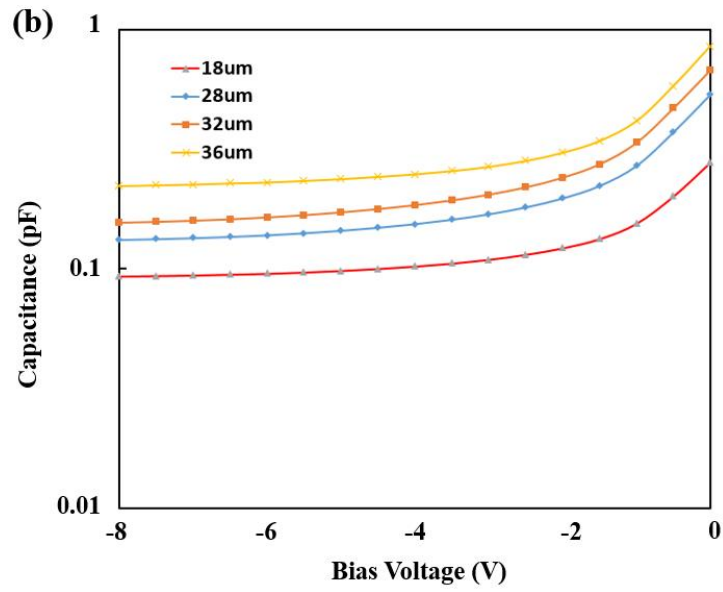


Figure 3-4. (a) LCR meter for CV measurement; (b) Current-voltage curves for devices with different sizes; (c) measured and fitted capacitances.

The capacitance-voltage (C-V) measurement can characterize the photodiode junction capacitance, which can be used for RC-time constant calculation. The CV measurement was performed with an HP 4275A Multi-Frequency LCR meter.

After flip-chip bonding, the photodiode capacitance, which includes junction capacitance and parasitic capacitance, was measured at 100 kHz using an LCR meter. The capacitance initially decreases and then saturates when the junction is fully depleted after -4 V. The parasitic capacitance was extrapolated by plotting the measured capacitances versus areas as shown in Figure 3-4(c). A parasitic capacitance of 43 fF was determined from the intercept of the linear fitting. The parasitic capacitance is mainly from the CPW and contact pad.

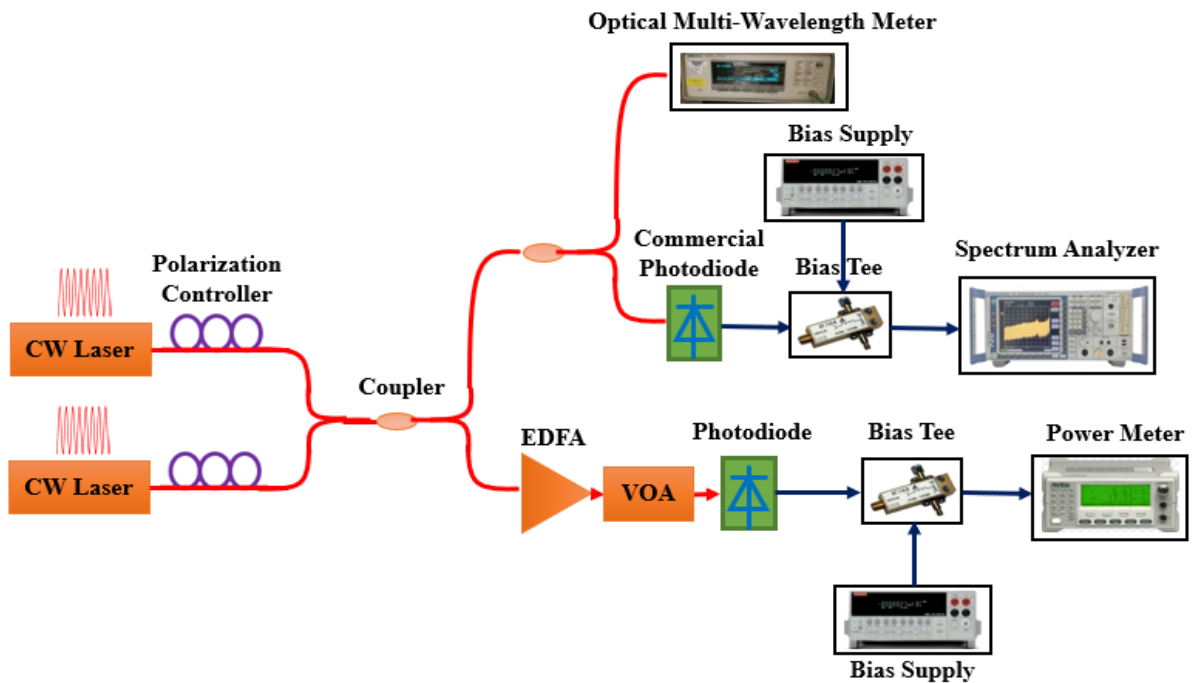


Figure 3-5. Optical heterodyne setup

The DC responsivity can be calculated by comparing the optical output power from the attenuator with the DC photocurrent read from the source meter. The measured responsivity was 0.36 A/W at 1550 nm.

The bandwidth and saturation characteristics were measured with an optical heterodyne setup.

Figure 3-5 illustrates the measurement set-up. CW light from two lasers with wavelength near 1550 nm was coupled through polarization controllers and combined with an optical coupler. To achieve 100% modulation depth, the output power of the DFB lasers needs to be matched by controlling the injection current. The beat frequency of the two lasers was tuned by changing the temperature of one laser. This achieved a wide frequency range. The signal was split into three branches. The optical signal was detected by an optical multi-wavelength meter at the first branch, which can monitor RF frequency above 50 GHz. For the second branch, the signal was coupled into a commercial 50 GHz photodiode followed by an HP8565E electrical spectrum analyzer. These monitored the beat frequency lower than 50 GHz. In the third arm, the signal was amplified by an erbium-doped fiber amplifier (EDFA), attenuated by a variable optical attenuator and focused onto the photodiode with a lensed fiber. The RF output power was detected with a power meter after a bias-tee. During the measurement, the lensed fiber was pulled back to the point where the photocurrent dropped by half to realize uniform illumination. A computer with a Labview program is responsible for controlling the measurement progress.

As shown in Figure. 3-6, the 18 μm -, 24 μm -, 28 μm - and 32 μm - diameter photodiodes exhibit bandwidths of 59 GHz, 44 GHz, 37 GHz and 31 GHz, respectively. The smaller devices work at V-band, while the larger diameter photodiodes demonstrate smaller bandwidth due to the increased RC-time limitation. Similar to other UTC photodiodes [63, 64], we observe bandwidth enhancement at high current levels due to the generated electric field in the undepleted absorber, which is beneficial to the carrier transport. For 18 μm -diameter device, the peaking effect from the high impedance transmission line is observed at 40 GHz, which improves the power level by 2 dB.

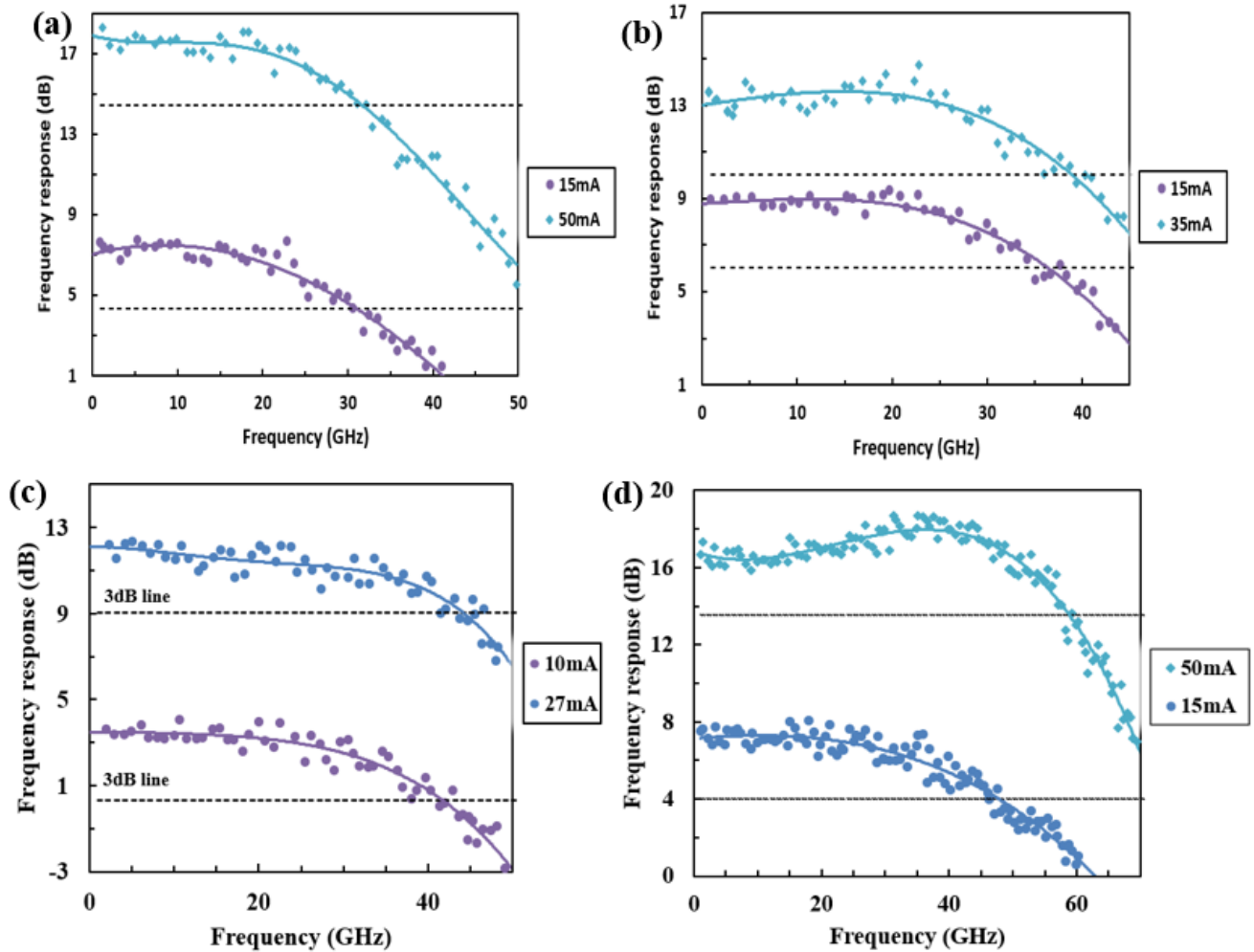


Figure 3-6. Bandwidth measurement under -6 V bias voltage of devices with (a) 32 μm -diameter, (b) 28 μm -diameter, (c) 24 μm -diameter and (d) 18 μm -diameter.

The saturation characteristics were then measured to demonstrate the RF output power. The saturation current is defined as the value where the RF compression decreases 1 dB from its peak value. As shown in Figure. 3-7, the corresponding maximum RF output powers at 28 GHz, 34 GHz, 40.5 GHz and 50 GHz are 25.5 dBm, 24.5 dBm, 24.3 and 22.3 dBm with saturation currents of 150 mA, 130 mA, 105 mA and 90 mA, respectively. The output RF power approaches the ideal RF power gradually with increasing photocurrent. This is the well-known bandwidth enhancement that originates from the current-induced electric field in the graded absorption layer [81, 82]. As

photocurrent increases, the space-charge effect causes an electric field reduction in the depletion region, which impedes carrier transport and ultimately leads to saturation. To mitigate the space-charge effect, the reverse bias voltage can be increased to the point where either thermal failure or junction breakdown occurs.

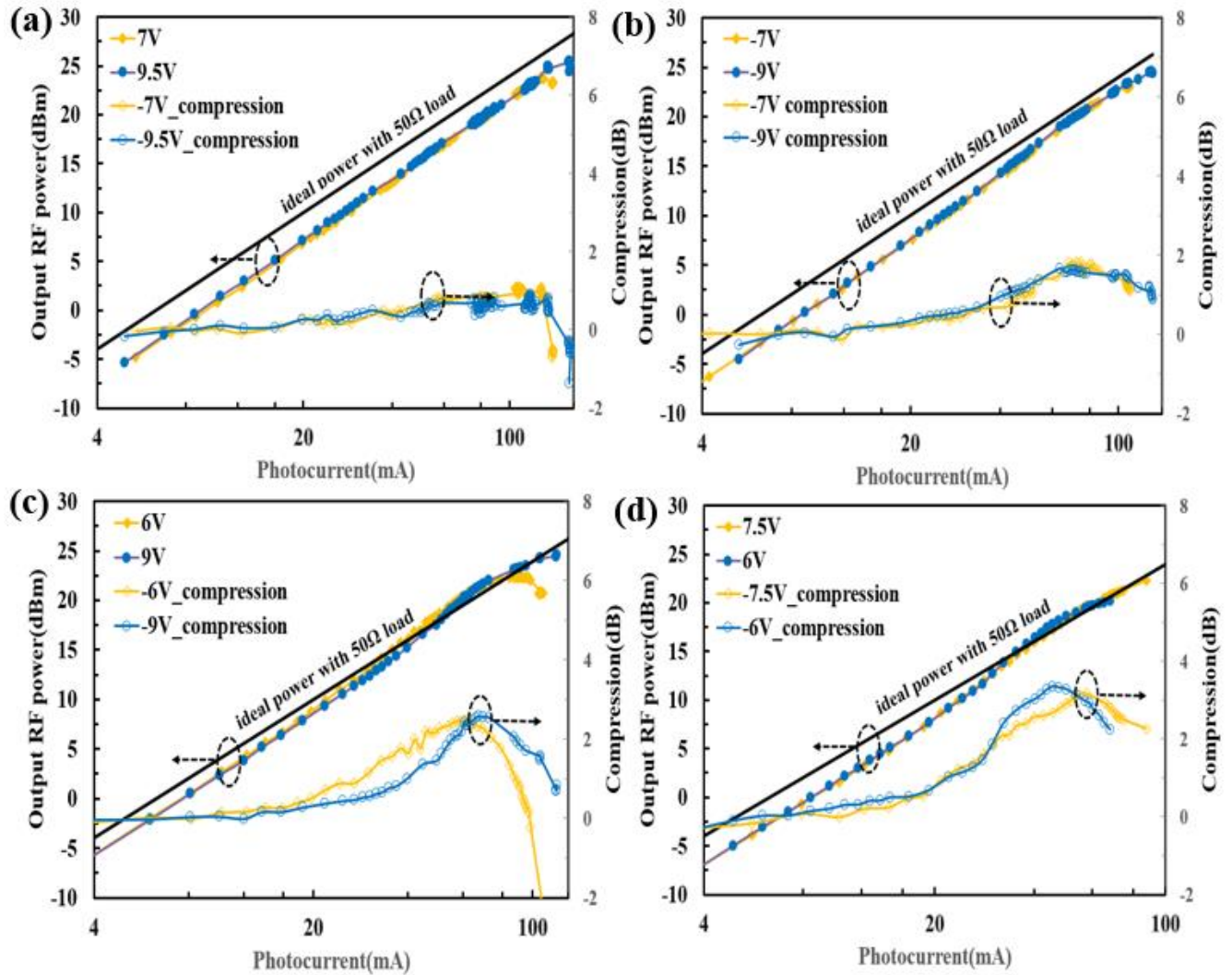


Figure 3-7. Output RF power versus photocurrent for devices with (a) 32 μm-diameter, (b) 28 μm- diameter, (c) 24 μm-diameter and (d) 18 μm-diameter.

The output power of the 18 μm-diameter device on diamond submount at 50 GHz is 22.3 dBm and that for a similar device on AlN with active cooling (~10°C) is 20.3 dBm [63]. The output RF

power improves by 57%. The failure power density, which is defined by the product of the reverse bias and the DC current at thermal failure, of an 18 μm -diameter photodiode on diamond submount increases by 36% compared with that of a photodiode flip-chip bonded to AlN [63].

A summary of RF output power versus frequency is plotted in Figure. 3-8. Compared to previous results of different types of photodetectors, my CC-MUTC photodiodes achieve the record high output RF power in the frequency range from 30 GHz to 50 GHz. They are attractive for APLs because they enable high link gain and photonic generation of low-noise microwave signals. In addition, these photodiodes permit the replacement of expensive low-noise broadband RF amplifier [30].

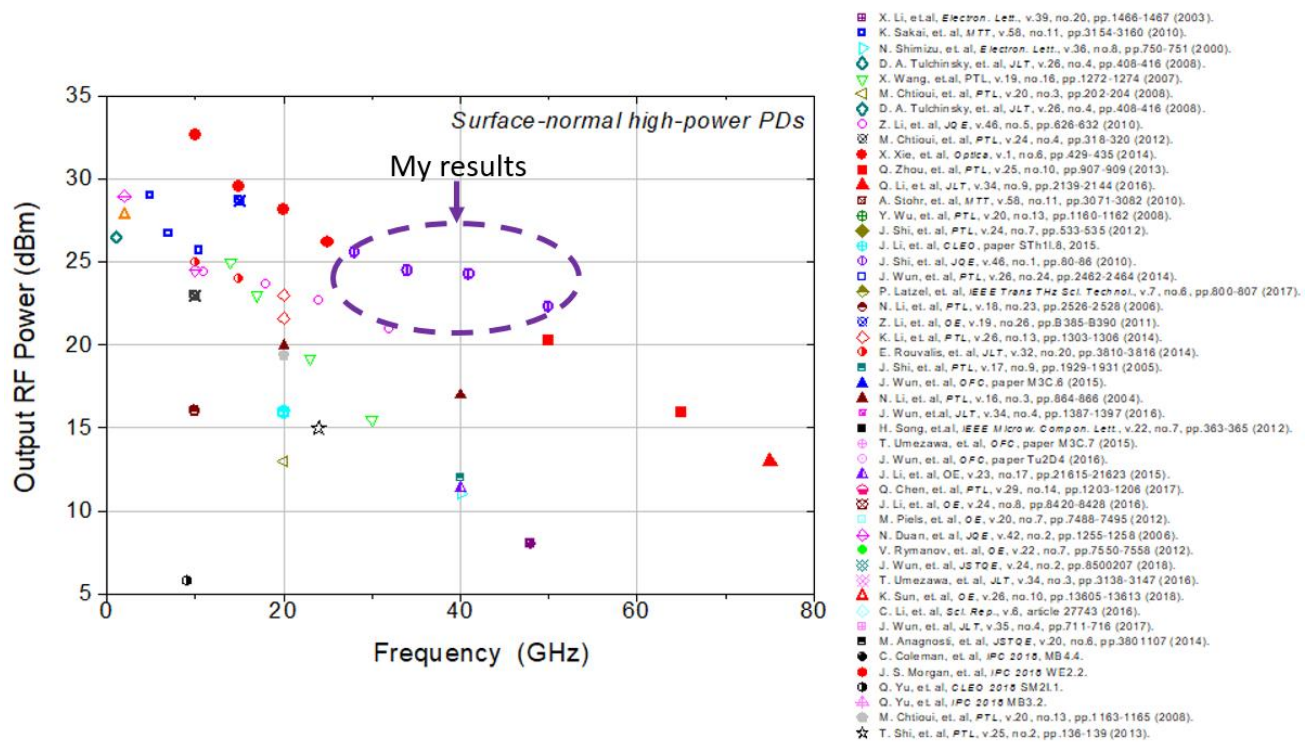


Figure 3-8. Summary of RF power versus frequency.

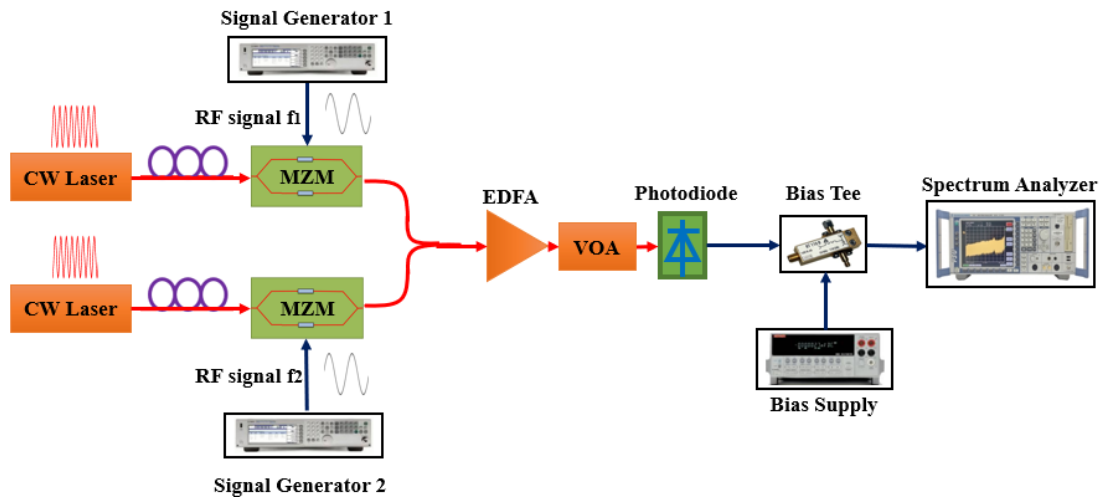


Figure 3-9. Two-tone OIP3 measurement setup.

To characterize the photodiode nonlinearity, the OIP3 was measured using the two-tone setup as shown in Figure 3-9. Light from two lasers near 1550 nm was intensity-modulated by two Mach-Zehnder modulator (MZMs) with the modulation frequencies of f_1 and f_2 , respectively. The polarization controllers were used before the MZMs to achieve the largest modulation efficiency because the MZM is sensitive to polarization. The optical signal was coupled by a 3 dB coupler, amplified by an EDFA and controlled by an optical attenuator. Then, the light was converted to an electrical signal by the photodiode. After a bias tee, the power of IMD3 ($2f_1-f_2$, $2f_2-f_1$) and power levels of the fundamental frequency were measured with an electrical spectrum analyzer (ESA). Assuming that IMD3 always increases with the input power at a slope of 3, the OIP3 can be calculated according to equation (2.14).

During the OIP3 measurement, the frequency of the RF signals f_1 and f_2 needs to be chosen properly to make sure that the IMD3 will not overlap with other intermodulation distortion products. It should be noted that ESA itself will generate IMD3 due to the nonlinearity of the electrical components in the ESA. Typically, the IMD3 generated by the ESA is much stronger than that generated by the photodiodes under test. To solve this problem, an attenuator is usually

used at the input of the ESA. Since the IMD3 components decrease three times faster than the signal at fundamental frequency, the proper attenuation results that the IMD3 generated by the ESA is much weaker than the IMD3 generated by the photodiode. Then, the influence of the ESA nonlinearity can be avoided.

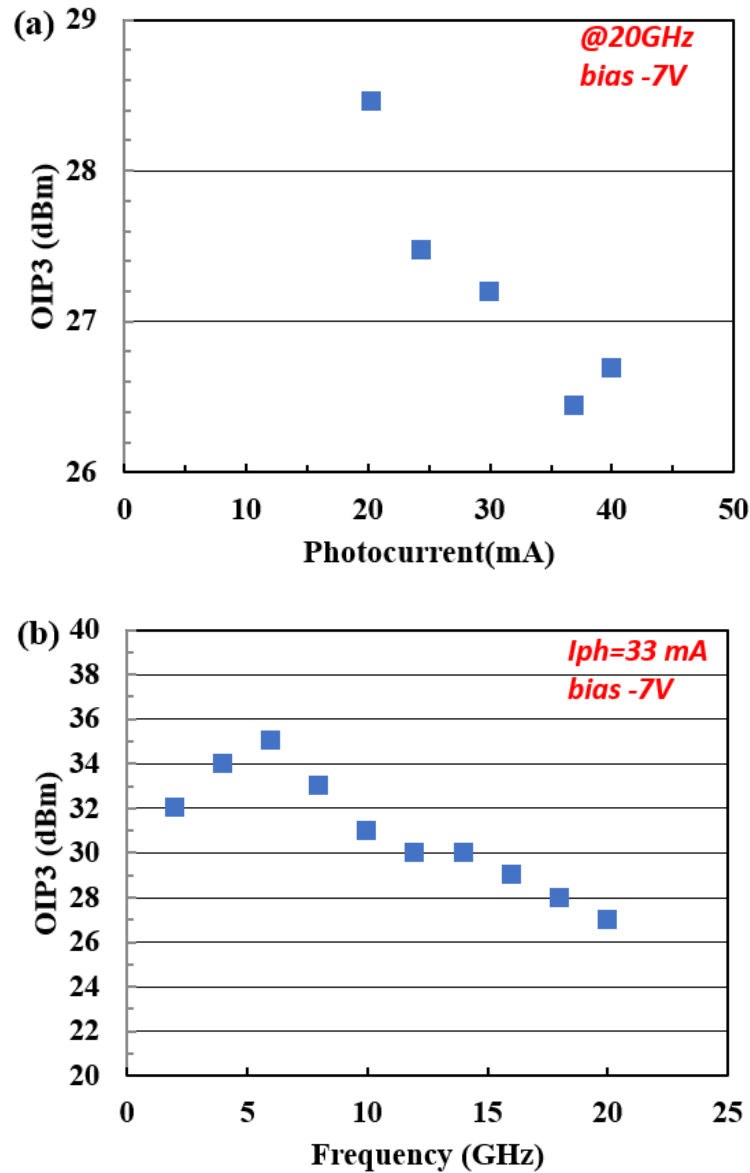


Figure 3-10. Measured OIP3 versus (a) photocurrent at 20 GHz; (b) frequency at 33 mA.

Figure. 3-10 shows the OIP3 of the CC-MUTC at different photocurrent and frequency for a 24 μ m-diameter device. The peak value of OIP3 is 35 dBm at 6 GHz and 28.5 dBm at 20 GHz.

There are four limiting factors for the MUTC photodiode nonlinearity, photocurrent-dependent responsivity, voltage-dependent responsivity, photocurrent-dependent capacitance, and voltage-dependent capacitance [83]. At high frequency, photocurrent-dependent capacitance and voltage-dependent capacitance are usually the dominating factors, which will be explained in Chapter 5. OIP3 varies with the photocurrent as shown in Figure. 3-10 due to the variation of differential capacitance. Typically, the photocurrent increase will lead to larger voltage swing on the load resistor and thus result in an increase of voltage-controlled capacitance. As a result, the OIP3 value decreases with the photocurrent here.

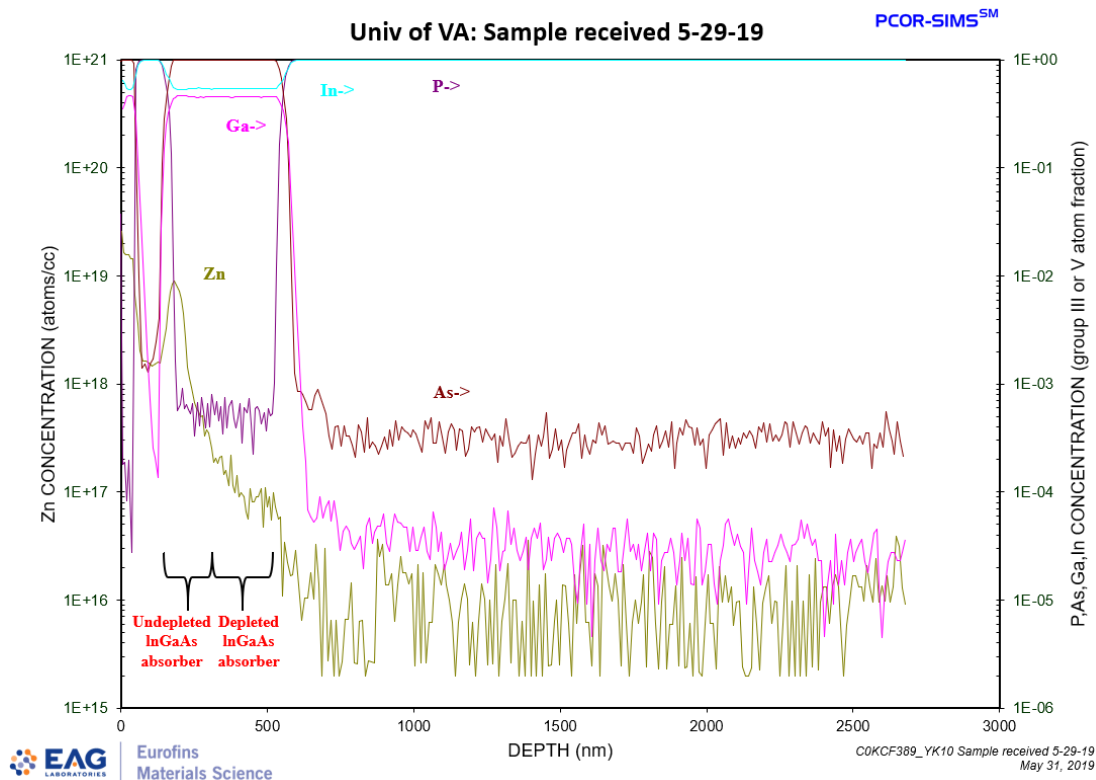


Figure 3-11. The SIMS results of InGaAs/InP wafers.

To further understand the nonlinearity, we did secondary ion mass spectrometry (SIMS) to observe the doping concentration. It can be observed from the SIMS results as shown in Figure 3-11 that the doping concentration of the depleted absorber is more than one order of magnitude

higher than the designed value due to Zn diffusion. Therefore, the doping difference between the depleted absorber and the undepleted absorber is not abrupt and thus the voltage-dependent capacitance is enhanced, which leads to lower OIP3 compared to the estimation.

3.5 Conclusion

In this chapter, 22.3 dBm output power at 50 GHz and 24.3 dBm at 41 GHz for flip-chip-bonded-on-diamond photodiodes without active cooling has been achieved. These CC-MUTC photodiodes achieved record high RF output in frequency range from 30 GHz to 50 GHz. The output RF powers improve by ~57% and the failure power increase by ~36 % compared to previous results with photodiodes bonded to AlN submounts. The measured third-order output intercept point showed a linearity of 29 dBm at 20 GHz.

Chapter 4 Optical Generation of Pulsed Microwave Signals

4.1 Device Structure

Photonic generation of microwave signals has attracted great interest for many years in application areas, such as satellite communications, 5G communications, optical sensing and phased array antennas, due to the low loss, high data rate and high frequency capability [35]. Previously, generation of continuous-wave microwave signals based on optical heterodyne [84], external modulation [24] and other approaches have been investigated [25]. Photonic generation of pulsed microwave signals is desirable for radar and wireless applications [27]. Among them, the X (8-12 GHz), Ku (12-18 GHz) and K (18-27 GHz) frequency bands are important and widely used for navigation, airport surveillance and imaging [26]. Various techniques including spatial light modulator-based pulse shaping [31], optoelectronic oscillation-based pulse phase coding [85] and polarization modulator-based signal phase coding [86] have been demonstrated to generate high-frequency pulsed radio frequency signals. Recently, Khaldoun et al. reported an optical frequency division system using a femtosecond laser frequency comb to generate microwave pulses with high spectral purity and stability [87]. However, to realize these applications in military platforms, it is important to generate high power pulsed RF signals. The photodiode is the key component to achieve this since it usually determines the peak power of the entire system. Previously, photonic generation of 1 GHz and 10 GHz RF signals with peak power of 41.5 dBm (14.2 W) and 40 dBm (10 W) using MUTC photodiodes have been reported [88]. In that work, the peak powers were limited by avalanche breakdown at high reverse bias.

In this chapter, I describe an optimized MUTC structure that achieved photonic generation of pulsed microwave signals at higher frequencies with higher peak power. The epitaxial design of

the back-illuminated MUTC photodiode that achieve high avalanche breakdown voltage is shown. One of the primary design goals was to increase the voltage at which avalanche breakdown occurs relative to the detectors used in Ref. [88]. The impulse response and generated pulsed RF signals are demonstrated. The relationship between the maximum peak power and duty cycle has also been studied.

4.2 Device Design and Characterization

The back-illuminated MUTC photodiode structure was grown on semi-insulating InP substrate by metal organic chemical vapor deposition (MOCVD). The epitaxial layers of the InP/InGaAs wafer are shown in Figure. 4-1(a). The growth began with an n-type InP contact layer. An 800 nm lightly n-doped drift layer acts as a space charge compensation layer that pre-distorts the electric field in order to achieve a flat electric field profile at high photocurrent. A cliff layer with a doping level of $1 \times 10^{17} \text{ cm}^{-3}$ and a thickness of 50 nm was used to adjust the electric field profile in the depleted absorber and drift layer [62]. Two 15 nm-thick lightly p-doped InGaAsP quaternary layers were deposited to assist hole collection and block electrons. The doping in the p-type undepleted absorber was graded in three steps in order to accelerate the carriers. A 100 nm InP layer was used to block the electrons and a 50 nm p-type InGaAs was used as the contact layer.

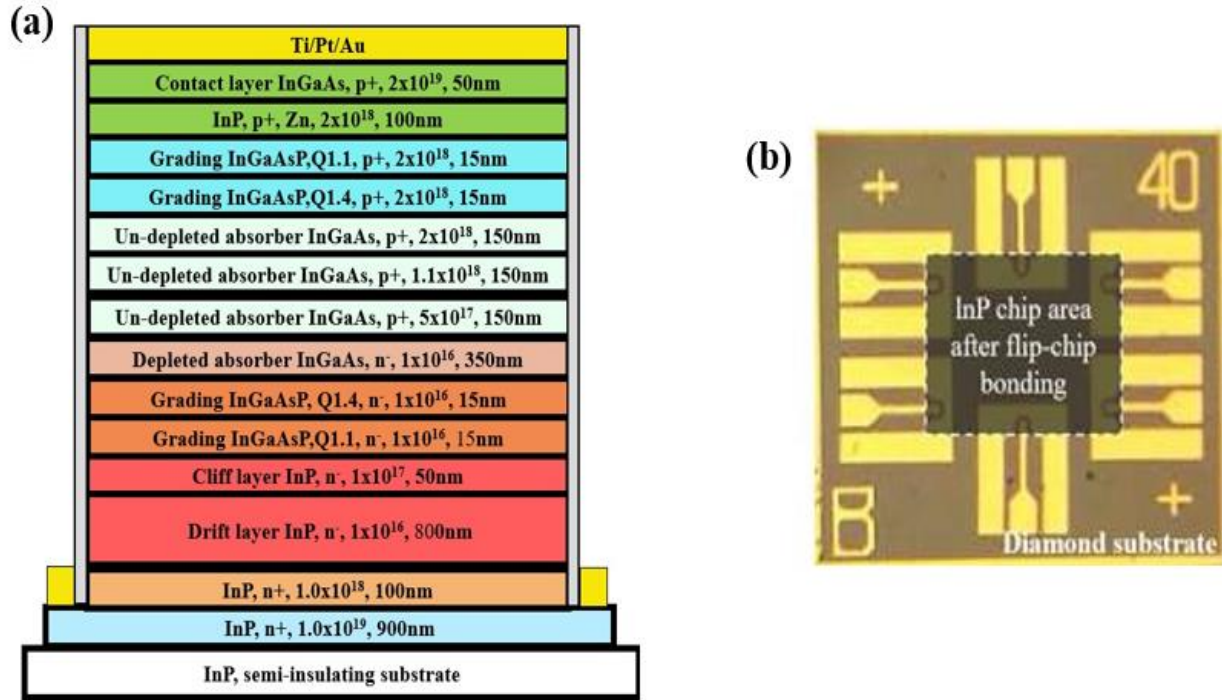


Figure 4-1. (a) Schematic cross section of InGaAs-InP MUTC photodiodes; (b) Photomicrograph of photodiodes.

The CC-MUTC photodiodes with diameters ranging from 34 μm to 50 μm were fabricated using the double-mesa structure. Ti/Pt/Au/Ti and AuGe/Ni/Au metal stacks were used as the p and n contacts, respectively. After polishing, a 194 nm-thick Si_3N_4 layer was deposited on the back of the wafer as an anti-reflection coating. The wafer was then diced into chips. In order to improve thermal dissipation, the diced chips were flip-chip bonded onto high thermal conductivity diamond submounts with coplanar waveguide pads. Figure. 4-1(b) is a photograph of a diamond submount with six sets of CPWs on the InP chip. The area with white dashed lines indicates the position of the InP chip after flip-chip bonding.

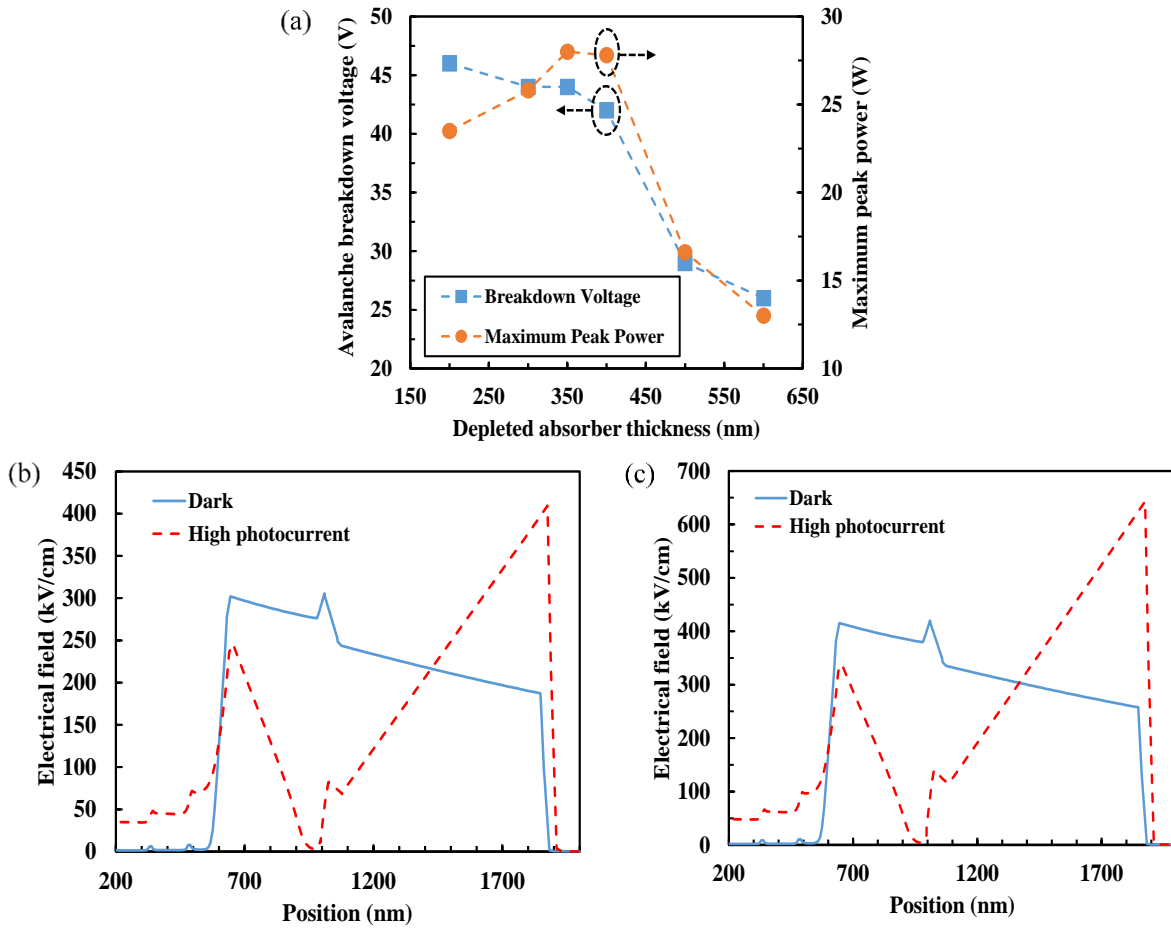


Figure 4-2. (a) Simulated breakdown voltage and peak power versus absorber thickness; Simulated electric field distribution at (b) -32 V and (c) -44 V when depleted absorber thickness is 350 nm.

Since pulsed-illumination significantly suppresses the deleterious heating effects, photodiodes can be biased at higher voltage to achieve higher peak power compared to CW operation. The thickness of the absorber region and the drift layer were optimized using the Crosslight simulation tool to achieve high avalanche breakdown voltage as well as suppression of the space charge effect. Avalanche multiplication occurs when the electric field in the depleted region exceeds the material breakdown electric field. The simulated breakdown voltage is the maximum voltage under which the simulated electric field is below the breakdown value. The relationship between the ionization

coefficients and electric field of InGaAs and InP can be found in [89-91]. It is worth mentioning that the breakdown electric field varies with the layer thickness because the required ionization coefficients for multiplication depend on the layer thickness. The 350 nm depleted absorber and 800 nm InP were adopted to enable a high simulated junction breakdown voltage of -44 V as showed in Figure. 4-2 (a), with the corresponding breakdown electric fields of 400 kV/cm in InGaAs and 560 kV/cm in InP. The electric field distribution under dark and intense illumination condition at -32 V and -44 V are shown in Figure. 4-2 (b) and (c). Impact ionization is most likely to occur in the InGaAs layer under low illumination and in the InP layer under intense illumination. This is a result of the change in the electric field profile with current. Under high-level illumination, excess holes and electrons accumulate in the InGaAs intrinsic region and the electric field becomes too low to maintain the saturation velocity of the carriers. Therefore, the device becomes saturated. The minimum required electric field in the depletion region to maintain electron saturation velocity sets a limit to the intensity of incident light and the maximum generated photocurrent. The simulated electric field collapses when the generated average photocurrent is 68 mA and the duty cycle of the gated signal is 5 % at -44 V. The simulated peak power can be calculated based on the generated photocurrent. As showed in Figure. 4-2 (a), initially the peak power increases with the increasing absorber thickness because the space charge effect in the drift layer is suppressed. The peak power decreases as the absorber thickness further increases due to the significant avalanche breakdown voltage drop caused by the lower breakdown electric field. The maximum simulated peak power of 28.5 W for 50 μm -diameter devices at 10 GHz can be achieved at an optimized depleted absorber thickness of 350 nm.

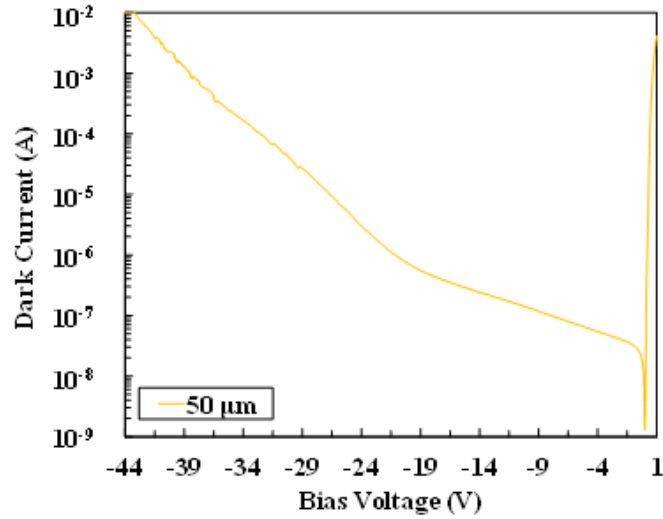


Figure 4-3. Current–voltage characteristic of a 50 μm -diameter device.

Figure. 4-3 shows the measured dark current versus bias voltage for a 50 μm -diameter device. Avalanche breakdown occurs when the number of impact ionization events increases dramatically and the multiplication gain (M) approaches infinity [92]. Since an abrupt increase of current is not observed, we conclude that the avalanche breakdown does not occur for bias lower than -43 V and the tunneling effect dominates the dark current for bias greater than ~ -20 V.

An optical heterodyne setup with optical modulation depth close to 100 % was used to characterize responsivity, bandwidth, and saturation current. The measured responsivity at 1550 nm is 0.69 A/W at room temperature. During the bandwidth measurements, the lensed fiber was pulled back until the maximum photocurrent dropped by half in order to achieve a uniform illumination. As shown in Figure. 4-4, the 50 μm -, 40 μm - and 34 μm -diameter photodiodes exhibit 3-dB bandwidths of 16, 20 and 27 GHz at 110 mA, 50 mA, and 50 mA photocurrent, respectively. A high impedance transmission line provides inductive peaking in order to boost the device bandwidth. As discussed above, an inductor can be used to create a pole in the transfer function of a photodiode which will cause peaking effect around a certain resonant frequency. Owing to the inductive peaking, all three devices show flat response up to 10 GHz. The bandwidth enhancement

that originates from the self-induced electric field in the graded absorption layer is observed at high photocurrent [82].

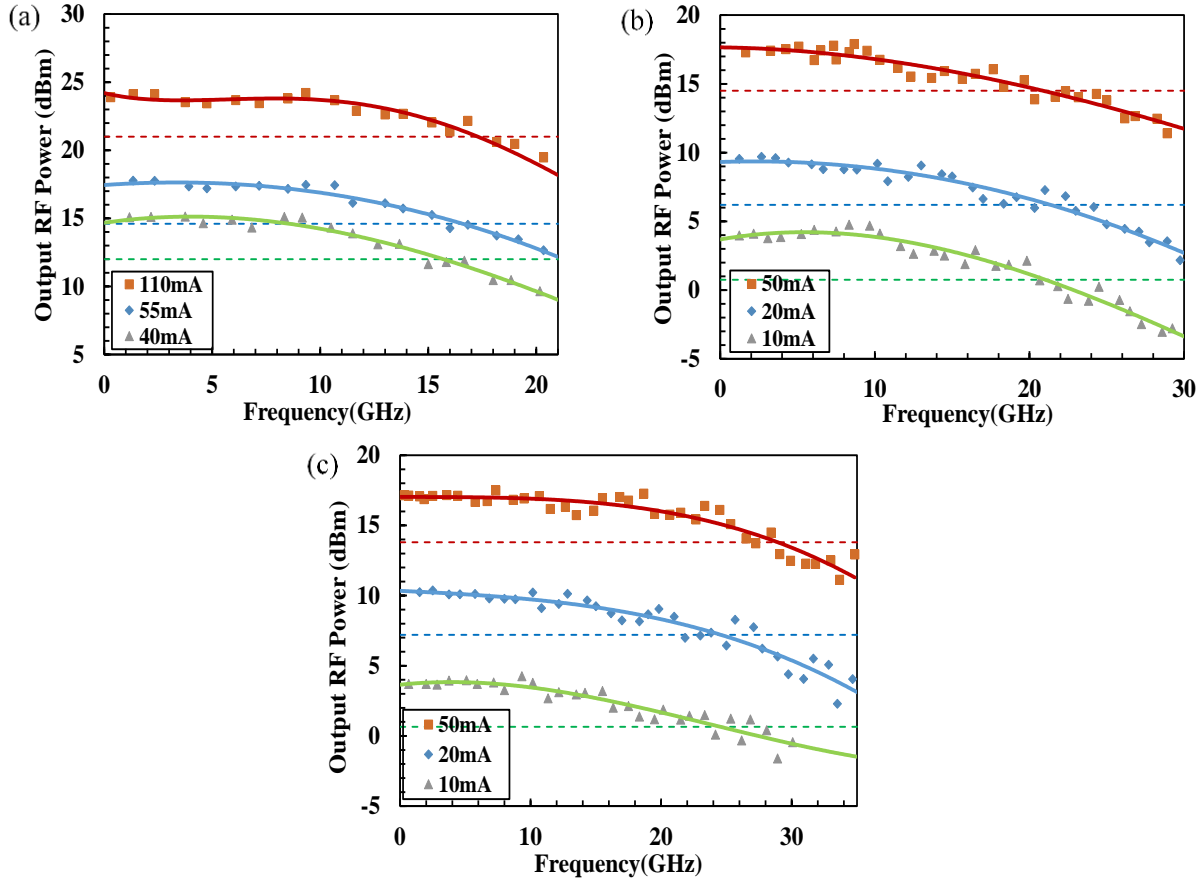


Figure 4-4. Frequency responses of the flip-chip-bond device with diameter of (a) 50 μm , (b) 40 μm and (c) 34 μm at different photocurrents.

During the saturation power measurement, the photodiodes were mounted on a copper heat sink at room temperature. A 50- μm device exhibits saturation current of 205, 265 and 290 mA at the 1 dB compression point. The corresponding RF output powers are 28.5, 31.2, and 32.3 dBm at -9 , -12.5 and -14.7 V bias, respectively. The saturation phenomenon at -12.7 V and -9 V are due to the space charge effect, which results in the electric field collapse in the depleted region. Higher bias voltage can suppress the space charge effect and lead to a higher RF output power. The device failed at -14.7 V bias and 290 mA average photocurrent. The heat generated at high

bias and high current leads to high junction temperature and thermal-related performance degradation [59, 93].

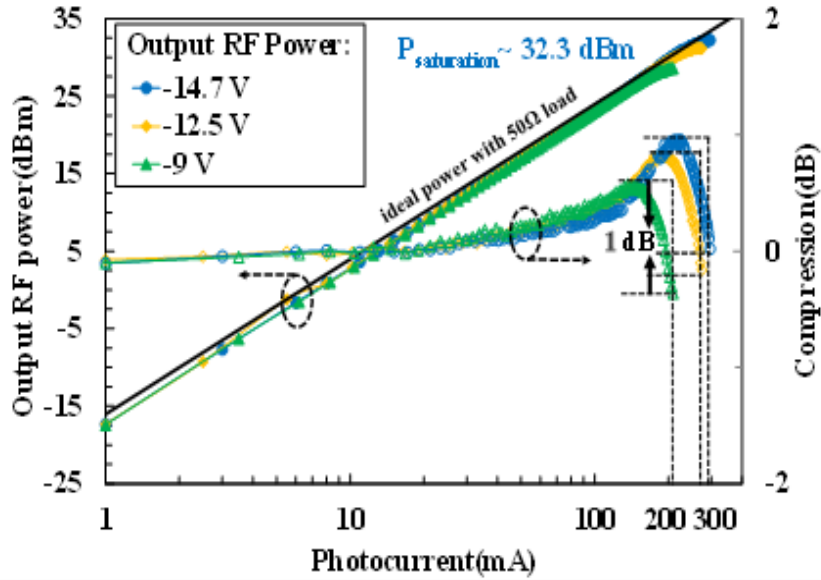


Figure 4-5. RF output power of 50 μm diameter device versus average photocurrent for different bias voltages at 10 GHz.

It is well known that thermal failure is the primary performance limitation for MUTC photodiodes under CW illumination. In contrast, the photodiodes under pulsed-illumination can handle higher bias voltage and achieve higher output peak voltage pulses since the generated heat does not have enough time to build up [88]. Generated heat can be dissipated from the junction to the submount between the pulses.

4.3 Impulse Response

A femtosecond Erbium-doped laser with pulse width < 50 fs and 100 MHz repetition rate was used to measure the pulse response. Figure. 4-6 shows normalized output waveforms of the pulse photoresponse measured at -17 V and -36 V. The output peak voltage increases linearly with increasing optical power before saturation as shown in the inset of Figure. 4-7, and the waveform

does not significantly change until it reaches the saturation point due to the space charge effect. MUTC photodiodes produce a 22 ps fall time (80 %-20 %) [94] at average photocurrent of 1 mA and 25 ps at 2.1 mA at -17 V. The fall time remains the same at -36 V as input power increases. The fall time of the photoresponse does not significantly increase due to the fast response of electrons in the depletion layer [95]. When the device reaches saturation, the pulse width increases and the frequency response degrades gradually with increasing photocurrent. At -17 V, the photodiode starts to saturate and the pulse exhibits broadening after an average photocurrent of 1 mA. The pulse experiences larger shape distortion at 2.1 mA. The space-charge induced saturation and concomitant pulse shape distortion can be mitigated by higher bias voltage. At -36 V, the waveform remains unchanged at an average photocurrent of 2.1 mA.

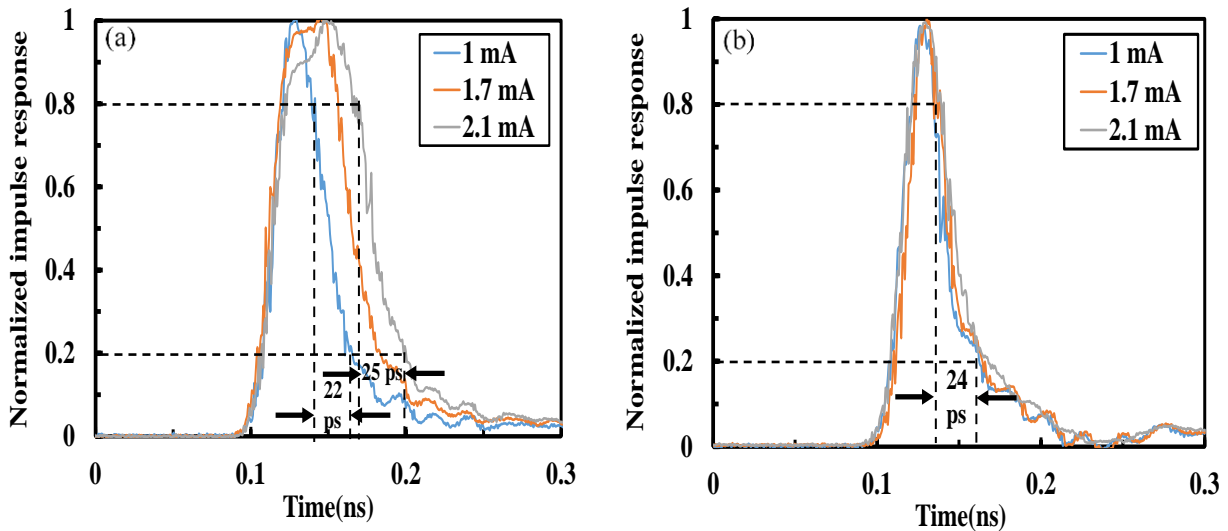


Figure 4-6. Normalized impulse response for different average photocurrents at (a) -17 V and (b) -36 V.

In order to measure the maximum peak voltage, the input optical power and corresponding average photocurrent were increased until the impulse response completely saturated. Figure. 4-7 shows the maximum peak voltage versus bias voltage for a 50- μm device at room temperature. The slope is approximately 1. The inset plot is the output peak voltage versus optical power at

-39.5 V bias voltage. The peak voltage reaches 38.3 V at average photocurrent of 4.6 mA, while the FWHM stays at 30 ps. The peak voltage (38.3 V) and corresponding peak power (29.3 W) are the highest reported for photodiodes with similar bandwidths at 1550 nm [95, 96]. The peak voltage is 6 V higher than the previous reported MUTC photodiodes [88]. Even though pulsed operation suppresses thermal degradation, the maximum operating voltage is primarily thermal limited instead of avalanche breakdown.

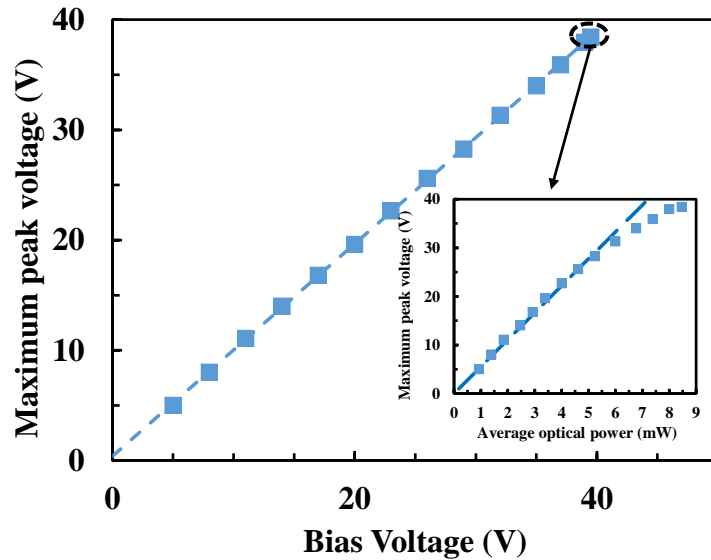


Figure 4-7. Maximum peak voltage versus bias voltage. Inset: Output peak voltage versus average optical power at -39.5 V.

4.4 Pulsed Microwave Signal Generation

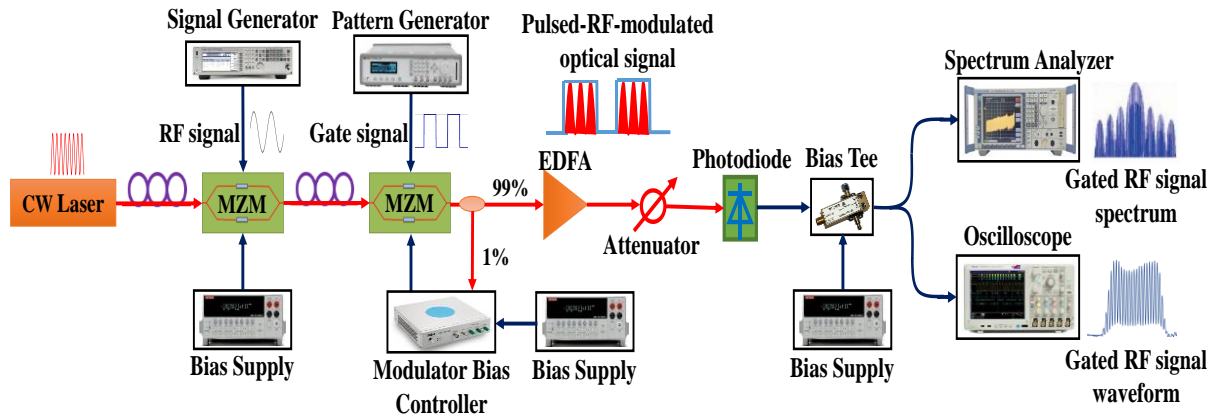


Figure 4-8. Experimental setup for pulsed microwave signals generation.

Figure 4-8 shows the pulsed microwave signal generation setup. A high power and narrow linewidth CW fiber laser working at 1550 nm was used as the source. The first MZM was driven by an RF signal with power of 17 dBm. The modulator was biased at quadrature bias point. The gated RF signal was modulated on optical signal by the second modulator. A bias controller was used to ensure that the second MZM was locked at its null point and the RF signal was limited within the pulse duration. The pulsed optical signal was amplified by an EDFA and the output optical intensity was controlled by a digital optical attenuator. The pulsed RF modulated optical signal was converted to a pulsed RF electrical signal by a high power MUTC photodiode. The output signal was then measured by a spectrum analyzer and an oscilloscope simultaneously after a bias tee. A microwave attenuator was used before the oscilloscope and spectrum analyzer due to the power limitations of those instruments. The waveform and spectrum of the pulsed RF signal are also shown in Figure. 4-8.

The individual spectral components of the pulse RF signal were measured with the spectrum analyzer. The peak power can be calculated using the equation [97]:

$$P_{\text{peak}} = P_{\text{in}} - 20 \log(\tau/T) \quad (4.1)$$

where τ is pulse width, T is pulse period, and P_{in} is the measured power at the central line of the main lobe in the spectrum. The peak power can also be calculated based on the peak voltage read from oscilloscope. The scheme can guarantee the RF signal was 100 % modulated and was perfectly confined in the gate. In addition, MUTC photodiodes can handle high power gated signal within a short period of time. High-power pulsed microwave signals can be generated using the setup.

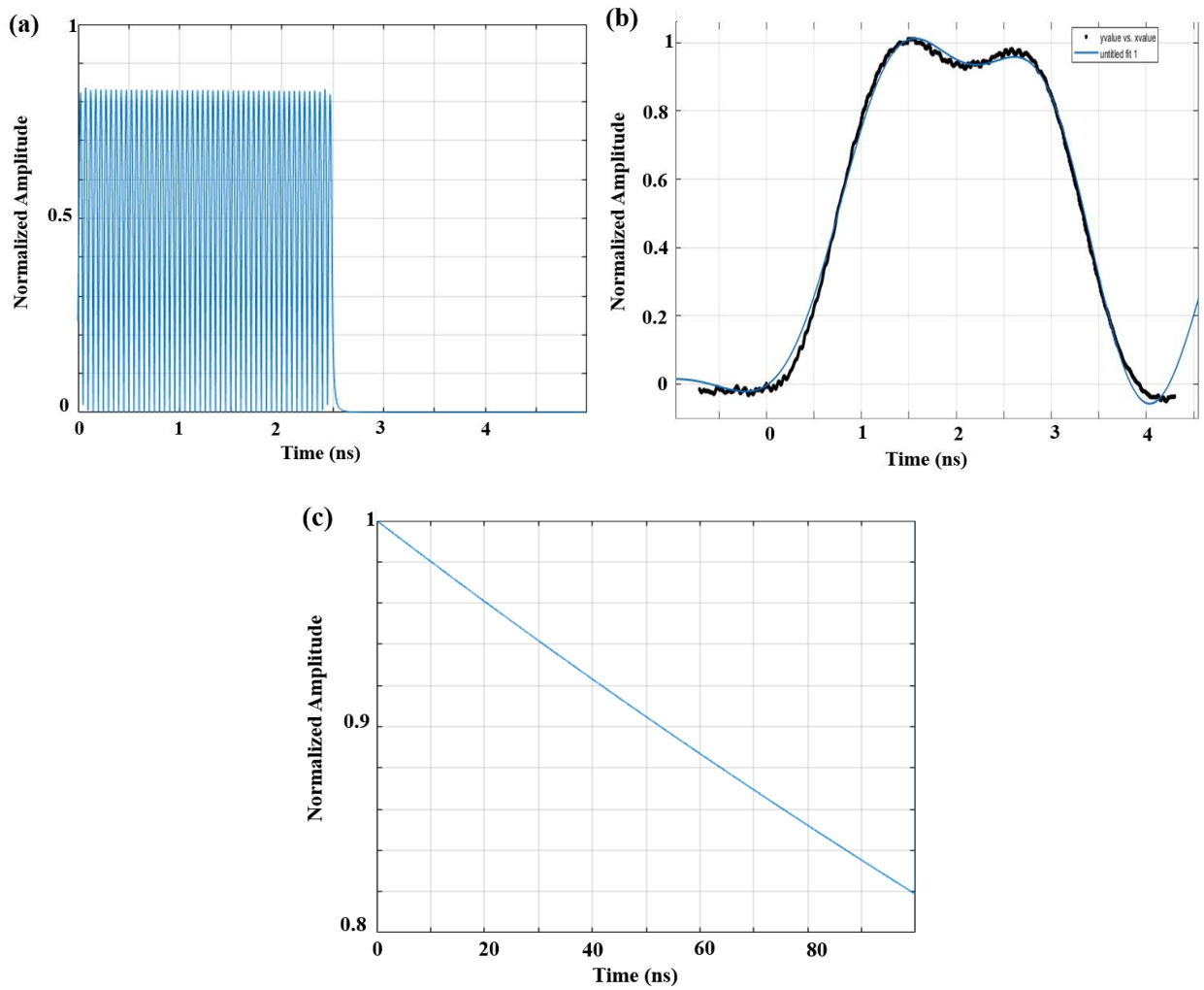


Figure 4-9. Normalized shape of (a) rectangle waveform; (b) pattern generator output waveform and (c) EDFA transient waveform.

To estimate the received waveform and spectrum on an oscilloscope and spectrum analyzer,

the whole process was simulated in Matlab. The ideal periodic rectangle waveform can be generated as shown in Figure 4-9 (a). However, when it generates a very short pulse, the pattern generator will induce some distortion due to the speed limitation of the electrical components. Our pattern generator output waveform was obtained and fitted with a higher-order function. The electrical signal was converted to an optical signal with a MZM and the signal was amplified by an EDFA.

For an EDFA, short and high-power pulses typically cause input signal saturation, which effectively decreases the population inversion by stimulating ions to lower energy levels in large numbers, hence causing the gain to decrease. When the input pulse is removed, the population inversion and gain return to the initial state. This effect is known as saturation induced gain modulation [98]. As shown in [99], EDFA transient effects can be modeled using the following equation:

$$\frac{P_{out}}{P_{in}} = K_1 \exp [\exp(-K_2 t)] \quad (4.2)$$

where K_1 and K_2 are constants that can be extracted from the measured output waveform of the EDFA [88]. The calculated normalized shape of the EDFA transient waveform is shown in Figure 4-9 (c). Then, the simulated signal after the EDFA in the time domain was converted to signal in frequency domain by fast Fourier transform (FFT) and some centralization/normalizing operations. It should be noted the current signal needs to be transformed to a power signal. After multiplying with the transfer function of the photodiode, which is shown in Figure. 4-4, the simulated spectrum can be obtained. Based on that, the time domain waveform can be calculated by shift/normalizing operations and inverse fast Fourier transform (IFFT).

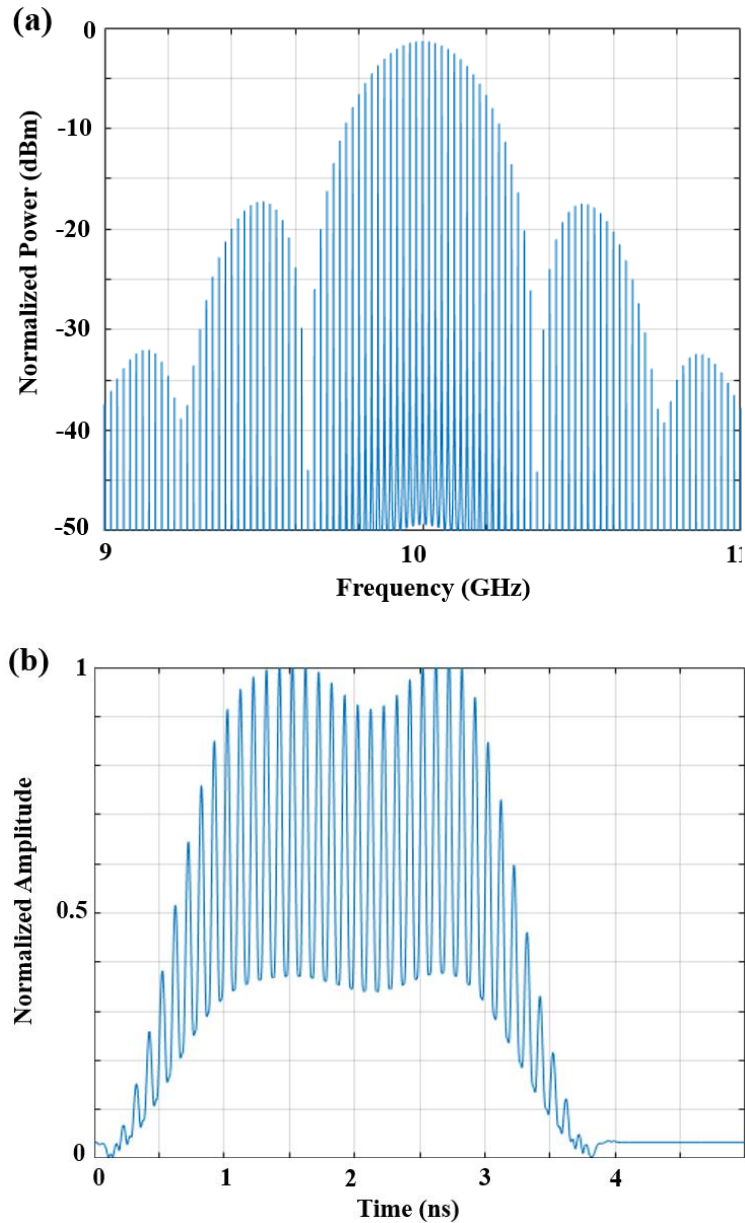


Figure 4-10. Normalized output signal in (a) frequency domain and (b) time domain.

The simulated output with 10 GHz RF carrier signals is shown in Figure 4-10, when the repetition rate is fixed at 20 MHz and the duty cycle is 5 %. To obtain the peak power, the simple way is to measure the power of the central line at the main lobe in the spectrum and then calculate according to equation (4.1) if we assume the gate signal is perfect. However, the gate signal applied on the optical signal differs slightly from a periodic rectangle waveform due to the pattern

generator distortion and EDFA saturation. The accurate way is to integrate all power lines in the power spectrum to obtain the average power and divide by the duty cycle. I calculated the peak power both ways for 10 MHz, 20 MHz and 30 MHz repetition rates. The deviation is less than 0.2 dB, which is negligible. Therefore, we calculated the peak power in the first way during the measurement.

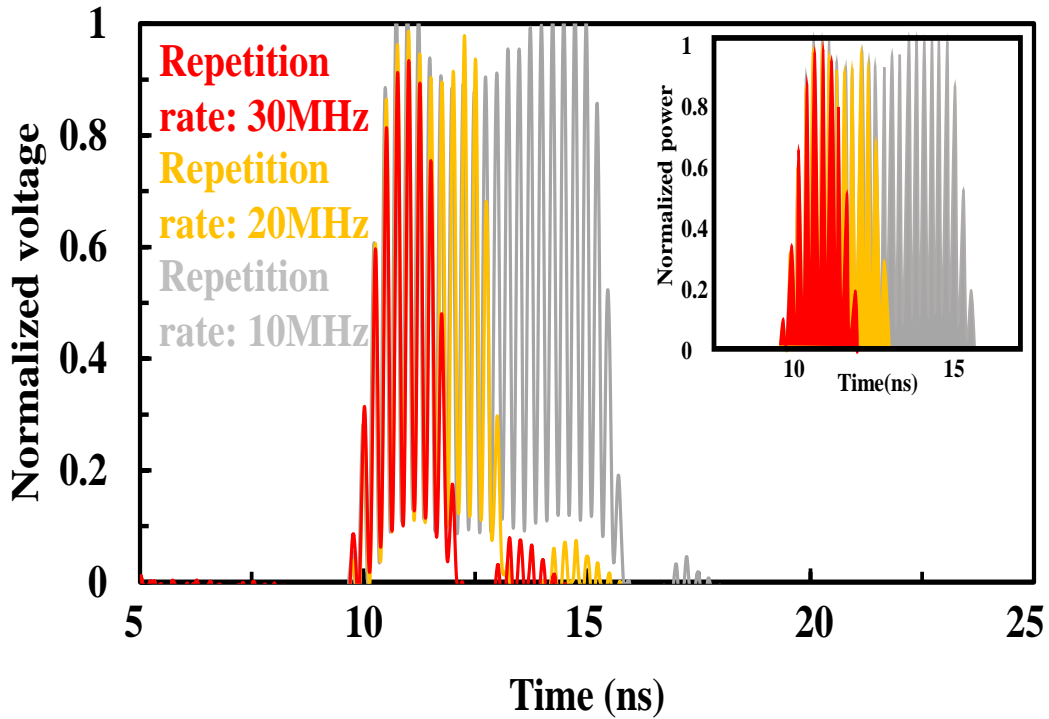


Figure 4-11. Waveform of the pulsed RF signal at 4 GHz. Inset: Waveform of input optical signal.

The normalized waveforms of the measured pulsed signals with 4 GHz RF carrier signals are shown in Figure. 4-11. The corresponding input optical signals are shown in the inset. Three pulse repetition rates were used: 30 MHz, 20 MHz, and 10 MHz with a 5 % fixed duty cycle. The corresponding pulse widths were 1.7 ns, 2.5 ns, and 5 ns, respectively. The waveforms were measured at reverse bias of -8 V and the average photocurrent of 2 mA. Note that a bias point controller was used to remove the bias point shift and mitigate signal oscillation in the off state.

The pulse distortion is primarily due to the pattern generator waveform distortion, cable loss and EDFA saturation [99].

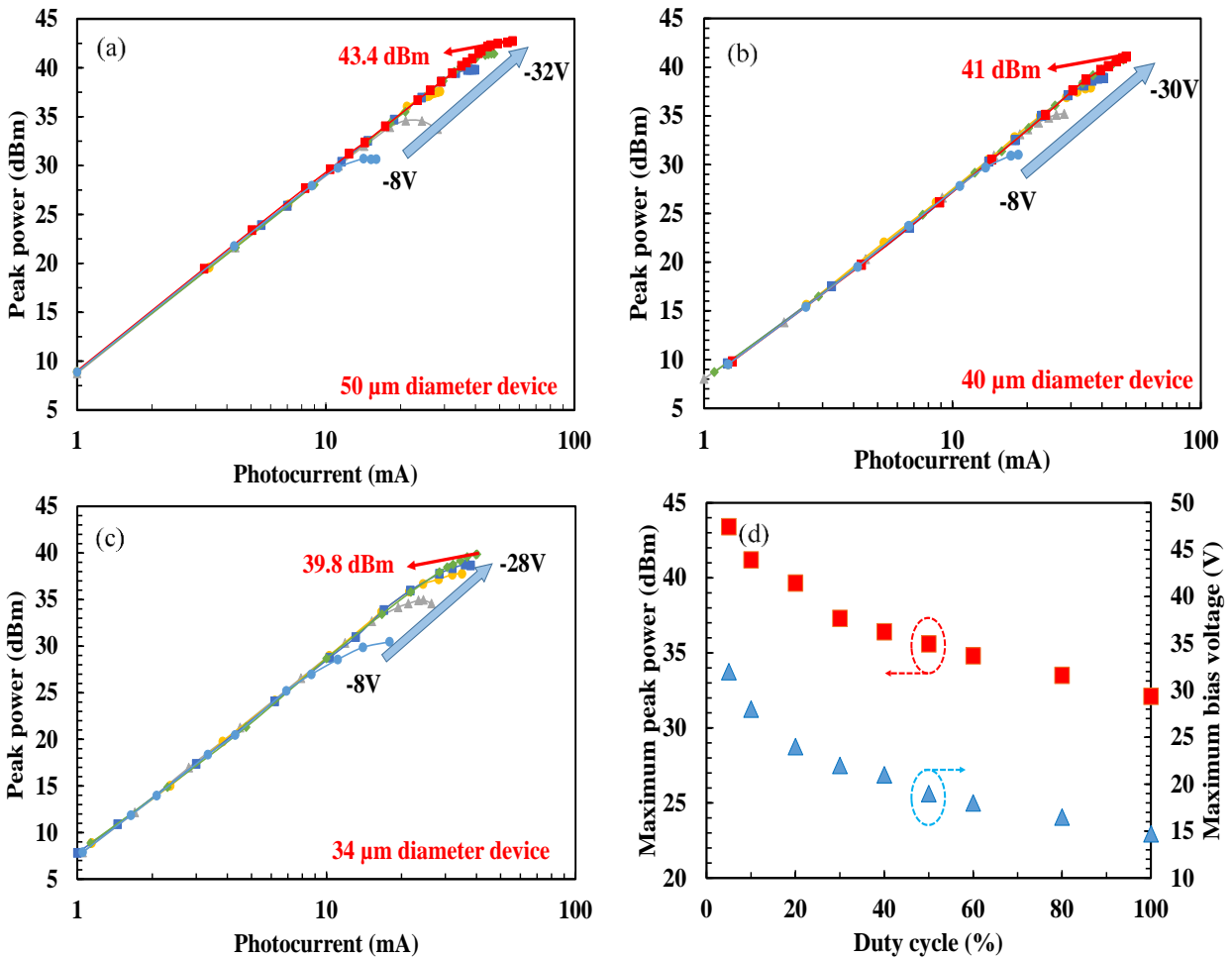


Figure 4-12. Peak power measured at (a) 10 GHz, (b) 17 GHz and (c) 22 GHz with 30 MHz repetition rate for different photocurrents at room temperature; (d) Maximum peak power and bias voltage at different duty cycles.

Figure 4-12 (a), (b) and (c) shows the peak powers of the pulsed 10, 17 and 22 GHz RF signals versus average photocurrent with different diameter devices. The experiments were conducted at room temperature at voltages in the range from -8 V to -32 V. The pulse repetition rate was fixed at 30 MHz and the duty cycle was 5 %. The peak power increases quadratically with the photocurrent before reaching saturation, which is primarily due to the space-charge effect. For a 50-μm photodiode, the peak power begins to saturate at -8 V and 11 mA average photocurrent as

shown in Figure. 4-12 (a). When the bias increases to -32 V, the maximum average photocurrent reaches 56 mA and the corresponding output peak power is 43.4 dBm. Larger bias voltage helps to mitigate the space-charge effect and thus enhances the peak power. The peak powers for gated modulation at 17 and 22 GHz are 41 dBm and 39.8 dBm for 40- μ m and 34- μ m photodiodes, respectively. The lower peak power at high frequencies is due to the larger current densities in smaller photodiodes. All the photodiodes failed before -32 V. Since avalanche breakdown for this device occurs at bias > -43 V as shown in the simulations, we concluded that the devices are limited by the thermal degradation rather than avalanche phenomena at 5 % duty cycle.

Figure 4-12 (d) shows the maximum peak power and bias voltage versus different duty cycles with 30 MHz repetition rate at room temperature. The maximum peak powers were obtained by increasing the photocurrent and the bias voltage until the devices failed. It can be observed that the bias voltage is higher at failure with the lower duty cycle. As duty cycle increases from 5 % to 100 %, the maximum peak power decreases by 11.3 dB and the maximum bias voltage decreases by 17.3 V. It can be concluded that thermal degradation is mitigated and the peak power is enhanced with decreasing duty cycle.

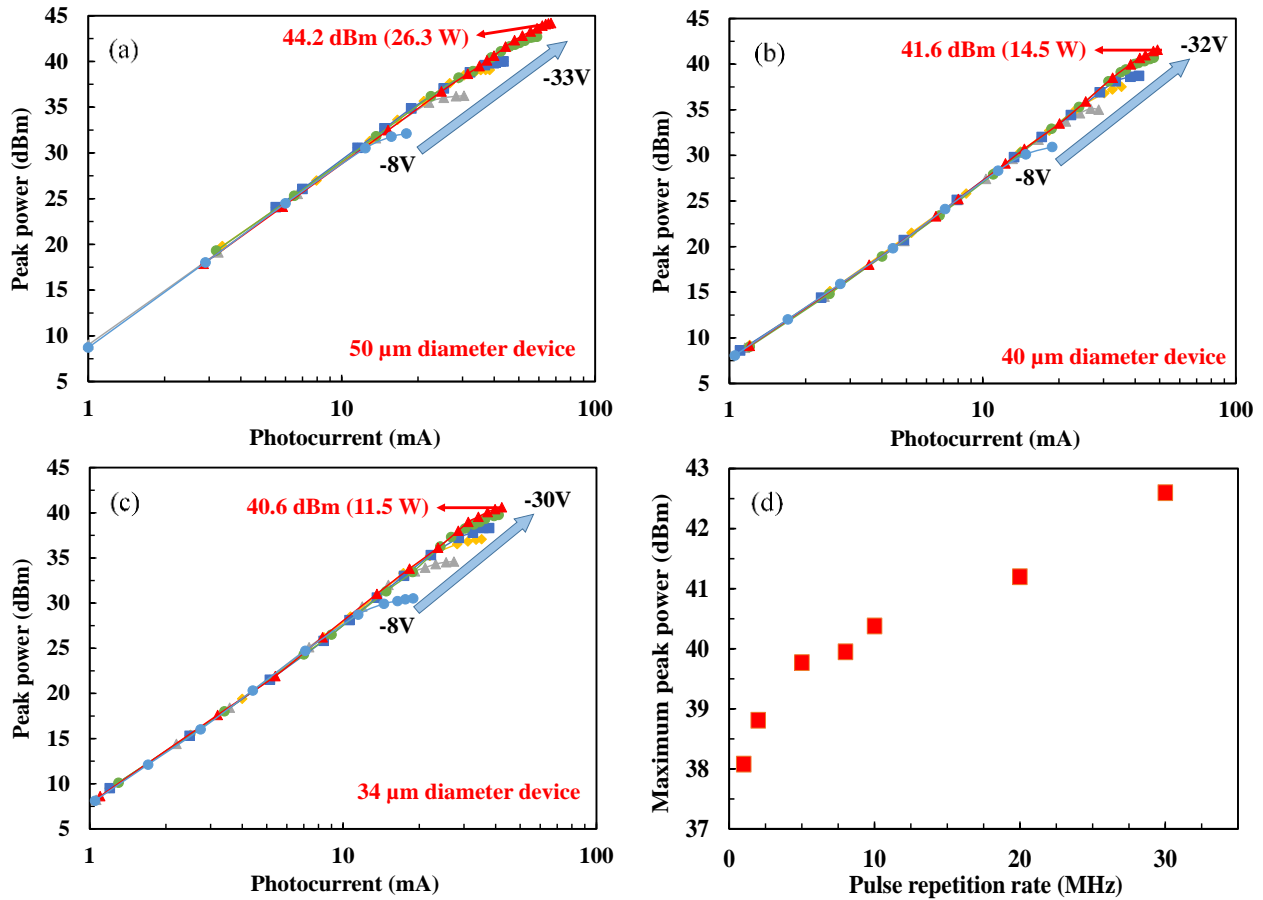


Figure 4-13. Peak power measured at (a) 10 GHz, (b) 17 GHz and (c) 22 GHz with 30 MHz repetition rate for different photocurrents at -10°C ; (d) Maximum peak power at different repetition rate.

In order to verify the above assumption that the peak power is limited by thermal degradation, the pulsed RF power was measured at -10°C using a thermoelectric cooler. Figure. 4-13 (a), (b) and (c) show the peak powers for different photocurrent at -10°C . The photodiodes with $50\ \mu\text{m}$, $40\ \mu\text{m}$ and $34\ \mu\text{m}$ diameter achieve peak powers of $44.2\ \text{dBm}$ ($26.3\ \text{W}$), $41.6\ \text{dBm}$ ($14.5\ \text{W}$) and $40.6\ \text{dBm}$ ($11.5\ \text{W}$) at 10, 17 and 22 GHz, respectively. The peak power increases at low temperature. For duty cycle of 5 % and repetition rate of 30 MHz, the thermal degradation of photodiodes is more significant than junction breakdown.

The relationship between maximum peak power and pulse width/repletion rate was also

studied. As shown in Figure. 4-13 (d), the maximum peak power increases from 38 dBm to 42.6 dBm when the pulse repetition rate increases from 1 MHz to 30 MHz at -28 V and 5 % duty cycle for the 50 μm -diameter device. The peak power performance is improved with increasing repetition rate and decreasing pulse width because the shorter pulses forestall thermal failure and experience less gain saturation in the EDFA . The pulse width of the gate signal, the heat dissipation capacity and the saturation characteristics of the EDFA limit the maximum peak power.

4.5 Conclusion

In this chapter, we have demonstrated photonic microwave generation of high-power pulsed signals using flip-chip bonded MUTC photodiodes. The photodiodes were designed with avalanche breakdown voltage higher than 43 V. The pulse photoresponse of these photodiodes achieved peak voltage of 38.3 V and FWHM of 30 ps. The peak powers were 44.2 dBm (26.3 W), 41.6 dBm (14.5 W) and 40.6 dBm (11.5 W) at 10, 17 and 22 GHz, respectively. These powers are the highest among literature.

Chapter 5 High-Power and High-Linearity Photodiodes at 1064 nm

5.1 Introduction

In recent years, the 1064 nm wavelength has been widely used in quantum optical systems, coherent detection, medical treatments and photonic analog links, which benefit from the availability of ultra-stable and ultra-low noise Nd:YAG lasers [37, 38, 100]. In addition, ytterbium-doped fiber amplifiers with broad gain bandwidth can boost output power to very high levels, offering the potential to build high-gain, low-noise 1064 nm analog optical links [39, 40] in which photodiodes with high bandwidth, high linearity, and high saturation current would be key components [101]. In order for these photodiodes to operate at high power, it is necessary to suppress the space-charge effect, which can cause the electric field in the depletion region to collapse. In addition, the generated heat at high bias and high current flow will lead to heating related performance degradation. At room temperature the photocurrent is typically much higher than the dark current. However, at high power level, dark current increases with temperature and the increased current then results in higher temperature, which can lead to thermal runaway [59]. Reducing the dark current is beneficial for high power operation. Linearity at high frequency is also critical for high-performance analog links in order to guarantee large spurious-free dynamic range. One figure of merit for linearity is the OIP3. The equivalent circuit analysis in [102] and [103] shows that the nonlinearities of MUTC photodiodes can be explained by the variation of the capacitance and responsivity with photocurrent and voltage. Previously, UTC photodiodes with OIP3 as high as 30 dBm at 39 GHz and 1550 nm wavelength have been reported [104]. However, comparable performance at 1064 nm has not been reported.

In this chapter I described two groups of back-illuminated charge-compensated MUTC photodiodes designed for operation at 1064 nm. The epitaxial designs and experimental results of the photodiodes are demonstrated. Bandwidth and linearity limiting factors are analyzed using an equivalent circuit model that extracts the parameters from S_{11} and Z_{11} measurements. Strong photocurrent- and voltage-dependence of the OIP3 is observed.

5.2 1st Group of Photodiodes

5.2.1 Device Design

The epitaxial-layer structure of the back-illuminated photodiodes is shown in Figure. 5-1. The InGaAsP/InP wafers were grown by MOCVD on 2 inch-diameter semi-insulating InP substrate. First, a 1000 nm heavily n-doped ($1 \times 10^{19} \text{ cm}^{-3}$) contact layer was grown. This was followed by a 100 nm InP layer. A lightly doped drift layer with a thickness of 400 nm was deposited to reduce the junction capacitance. After the drift layer, an InP cliff layer was grown to tailor the electric field profile in the drift layer and the depleted absorber. In contrast to previous InGaAs/InP MUTC photodiode designs [64], InGaAsP was used as the absorber to decrease the dark current. The doping in the undepleted absorber was step-graded ($5 \times 10^{17} \text{ cm}^{-3}$, $1.1 \times 10^{18} \text{ cm}^{-3}$, $2 \times 10^{18} \text{ cm}^{-3}$) to create a quasi-field that aids carrier transport. After another InGaAsP quaternary smoothing layer, a 100 nm InP cap layer was incorporated to block electrons. The top contact layer was p-type InGaAs with $2.0 \times 10^{19} \text{ cm}^{-3}$ Zn concentration.

Contact layer InGaAs, p+, Zn, 2×10^{19} , 50nm
InP, p+, Zn, 1.5×10^{18} , 100nm
Grading InGaAsP, Q1.1, p+, Zn, 2×10^{18} , 15nm
Un-depleted absorber InGaAsP, Q1.3, p+, Zn, 2×10^{18} , 100nm
Un-depleted absorber InGaAsP, Q1.3, p+, Zn, 1.1×10^{18} , 150nm
Un-depleted absorber InGaAsP, Q1.3, p+, Zn, 5×10^{17} , 150nm
Depleted absorber InGaAsP, Q1.3, n-, Si, 1×10^{16} , 100nm
Grading InGaAsP, Q1.1, n-, Si, 1×10^{16} , 15nm
Cliff layer InP, n-, Si, 4×10^{17} , 50nm
Drift layer InP, n-, Si, 1×10^{16} , 400nm
InP, n+, Si, 1.0×10^{18} , 100nm
InP, n+, Si, 1.0×10^{19} , 1000nm
InP, semi-insulating substrate

Figure 5-1. Epitaxial layer configuration of InGaAsP/InP photodiode.

The MUTC photodiodes were fabricated as double-mesa photodiodes using ICP etching. To avoid thermal failure and further increase the power handling capability of the photodiode, after wafer dicing, the chips were flip-chip bonded to AlN submounts with gold-plated coplanar waveguides.

5.2.2 Device Characterization

Devices with diameters from 10 μm to 28 μm were fabricated and the corresponding dark current versus bias voltage curves are shown in Figure. 5-2. The dark current for the 10 μm -diameter device was < 1 nA at -8 V. Compared to the traditional InGaAs absorber, the larger bandgap of InGaAsP is beneficial for reducing the dark current. The fact that the dark current varies linearly with the mesa diameter indicates that surface leakage is the dominate dark current mechanism.

The capacitance was measured with an LCR meter at 100 kHz before bonding. The

capacitance consists of the junction capacitance (C_{pn}) and parasitic capacitance (C_{st}). Figure. 5-3 shows the measured and calculated capacitance for different mesa areas. The capacitance measured at -8 V exhibits a linear relationship with area, which means the junction capacitance, C_{pn} , dominates the total capacitance. The parasitic capacitance, C_{st} , obtained from the intercept is 4.2 fF. C_{pn} agrees with the calculated capacitance when C_{st} is subtracted from the measured data.

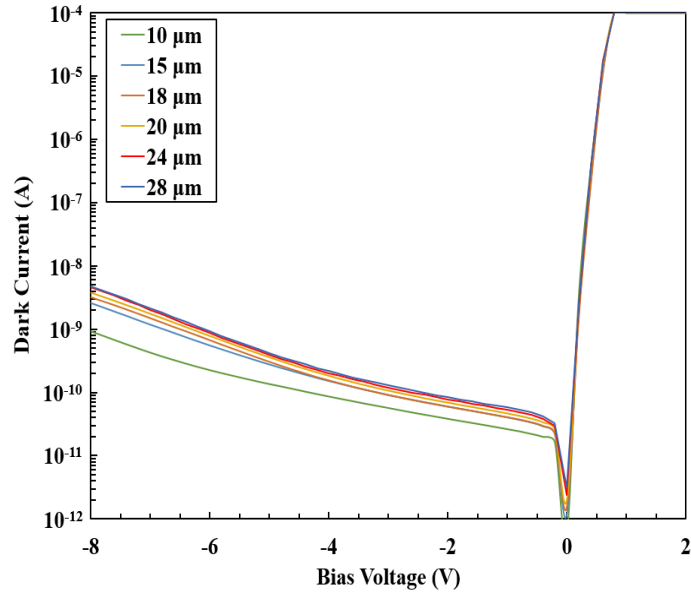


Figure 5-2. Dark current versus bias voltage curves of devices with diameters from 10 μm to 28 μm .

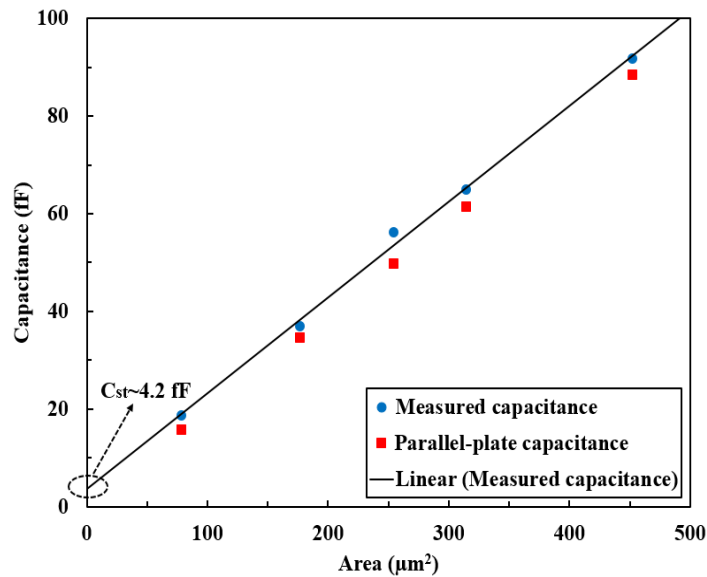


Figure 5-3. Measured and calculated capacitances.

The scattering parameter S_{11} was measured up to 50 GHz with a vector network analyzer (VNA) and a ground-signal-ground (GSG) probe. A photodiode circuit model in Keysight ADS software was used to simulate the frequency response. CPWs incorporated with high impedance transmission lines were simulated by electromagnetic analysis in ADS and were included in the model.

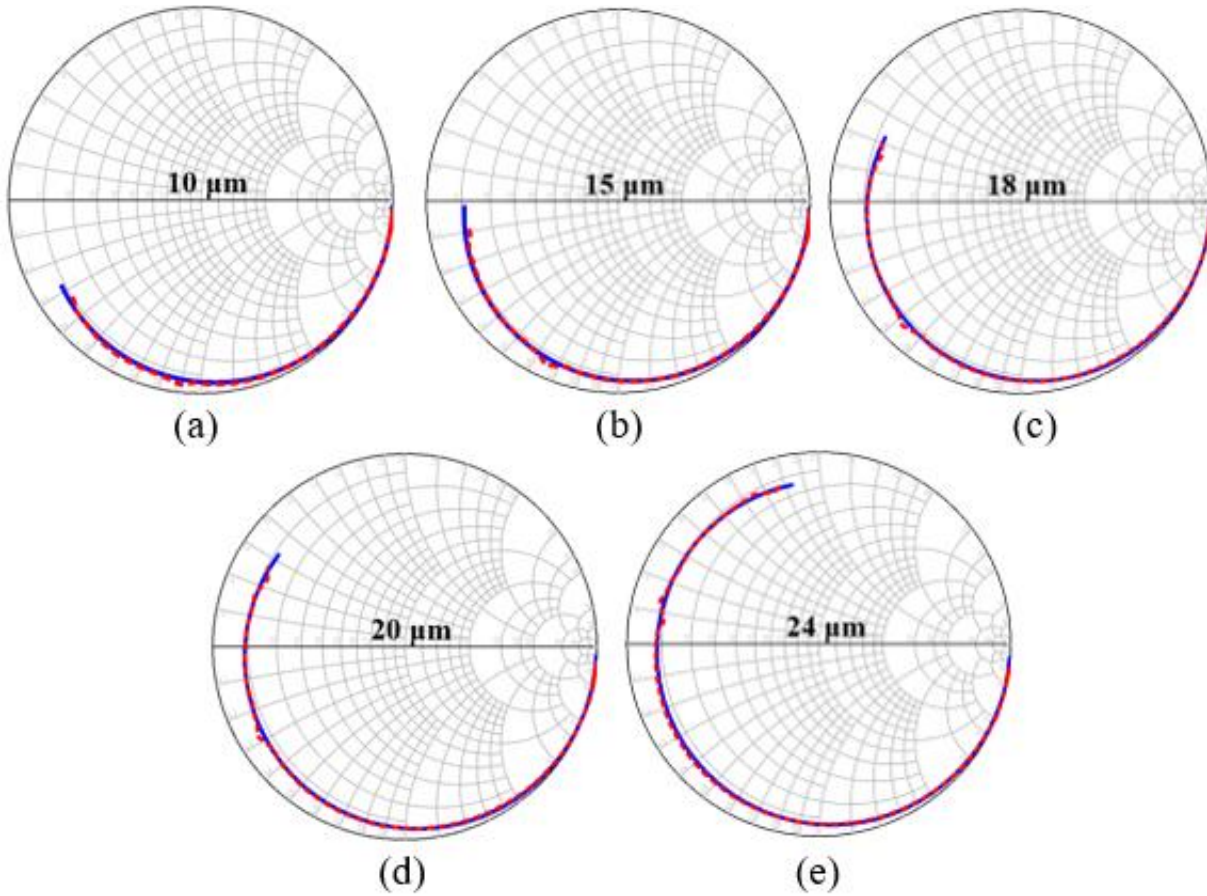


Figure 5-4. Measured S_{11} and fitting curves for photodiodes with: (a) 10 μm diameter; (b) 15 μm diameter; (c) 18 μm diameter; (d) 20 μm diameter; (e) 24 μm diameter.

The measured S_{11} (dotted lines) and fitted results (solid lines) for devices of different diameters at -6 V agree well on Smith Charts. A summary of the parameters that were measured, calculated, and extracted from fitting is shown in Table I.

Table 5-1. Measured and fitted parameters.

Diameter (μm)	10 μm	15 μm	18 μm	20 μm	24 μm
Calculated Capacitance (fF)	15.7	34.6	49.8	61.5	88.6
Measured Capacitance (fF)	19.79	38.03	56.1	65	91.8
Capacitance from S11 fitting (fF)	21	39	54	65	93
Series resistance from S11 fitting (Ω)	10	10	8	7.8	7.5

Note that measured and extracted capacitance consist of the junction and parasitic capacitance.

An optical heterodyne setup was used for the bandwidth measurement. The flip-chip bonded devices were mounted on a copper sink with a temperature of 20°C for the bandwidth measurements. The measured responsivity was 0.46 A/W at 1064 nm. The bandwidth was measured at -6 V, where the junction is fully depleted. As shown in Figure. 5-5, the photodiodes with diameters of 15 μm , 18 μm , 20 μm , 24 μm and 28 μm exhibit 3-dB bandwidth of 55, 41, 32, 27 and 22 GHz with 40 mA photocurrent, respectively. The ripples in the measured frequency response are from the multiple reflections of the signal at the GSG probe, the bias-tee, and the RF sensor head [105]. They affect the measurement more at high frequencies. Figure. 5-6 shows the frequency response for the 18 μm -diameter photodiode with 10 mA, 20 mA, and 40 mA photocurrent. Figure. 5-7 shows the simulated and measured bandwidths versus diameter. The transit time for this structure was obtained from the Apsys Crosslight Software and is 8 ps when the electric field is 100 kV/cm. The corresponding electron drift velocity is 0.95×10^7 cm/s in the InGaAsP depleted absorber. The overall simulation results (dash-dot line) take the high impedance transmission lines into consideration and match the measured bandwidth very well. The RC

component limits the bandwidth when the diameter is $> 15 \mu\text{m}$. There are two approaches that can be used to increase the bandwidth. The first is to decrease the RC product by increasing drift layer thickness. The second is to suppress the electric field in the depleted InGaAsP absorber by adjusting the cliff layer doping concentration, which would enable the electrons to travel at the overshoot velocity.

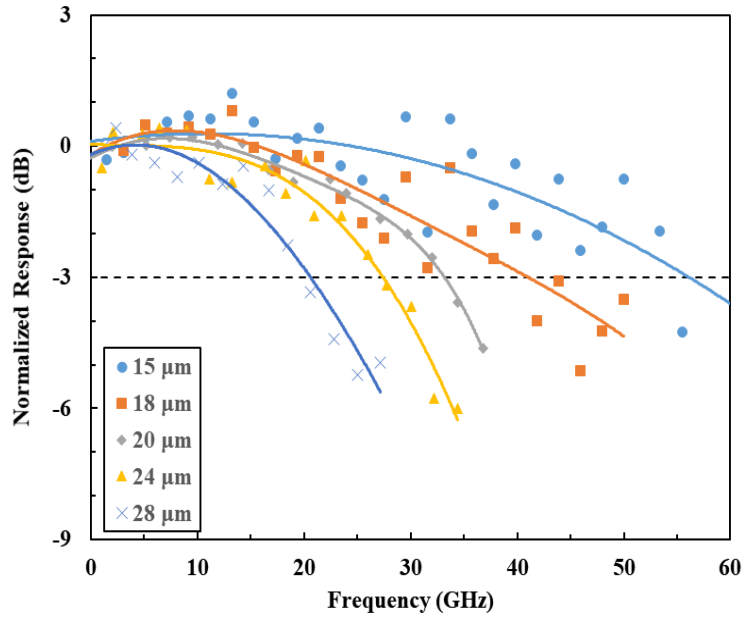


Figure 5-5. Measured frequency response of photodiodes with different diameters.

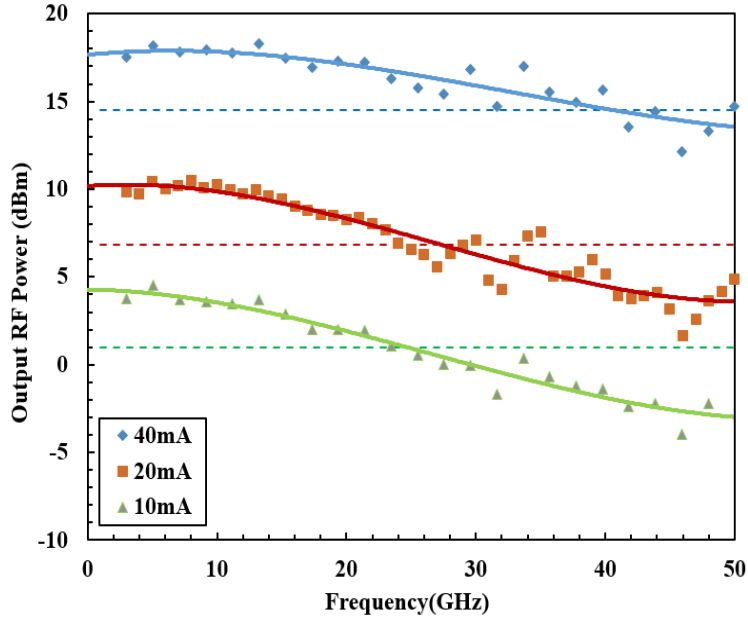


Figure 5-6. Measured frequency response of 18 μm -diameter photodiode at different photocurrent.

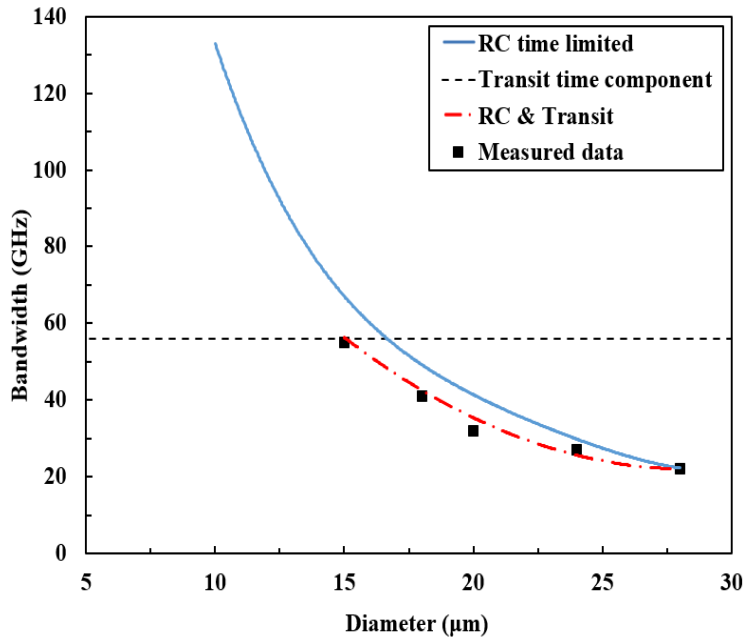
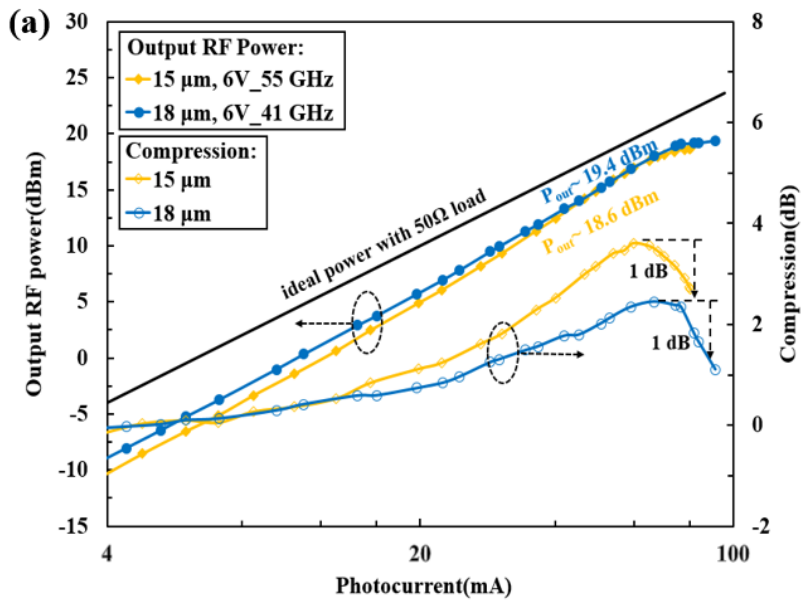


Figure 5-7. Measured and simulated frequency response.

The saturation characteristics were measured using the bandwidth setup described above. As shown in Figure. 5-8, the photodiodes with 15 μm -, 18 μm -, 20 μm - and 24 μm -diameter achieve saturation current of 80, 90, 127 and 139 mA at 55, 41, 32 and 27 GHz, respectively. All

measurements were conducted at -6 V. The corresponding RF saturation powers are 18.6, 19.4, 23.4 and 24.4 dBm, respectively. As the photocurrent increases before saturation, the RF output power moves close to the ideal power because the self-induced field results in higher bandwidth. For many devices, the saturation phenomenon is due to the space charge effect, which causes the field to collapse in the depleted region. Higher bias voltage can suppress the space charge effect but also leads to higher power density. It should be noted that the 20 μm -diameter photodiodes die due to thermal failure before reaching 1 dB compression. This could be alleviated somewhat if the devices were bonded on diamond with higher thermal conductivity [64].



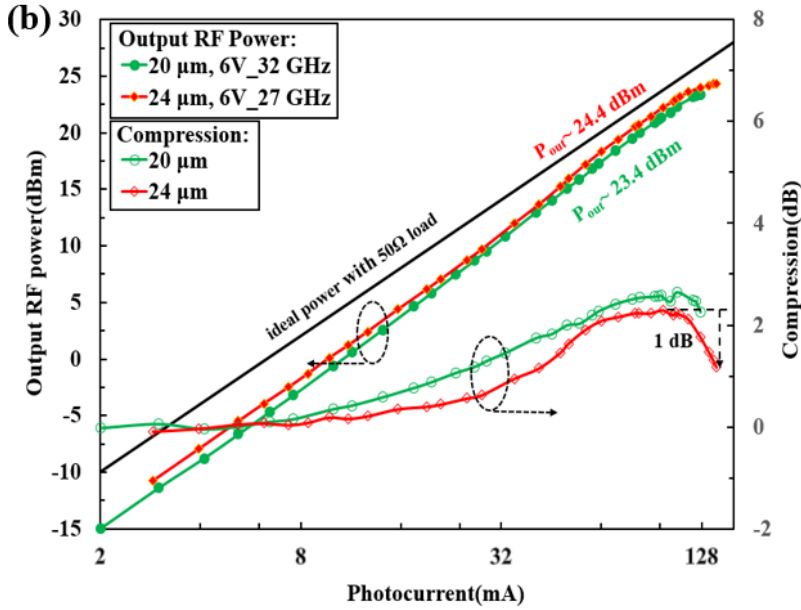


Figure 5-8. Output RF power and power compression at -6 V bias voltage for photodiodes with: (a) $15 \mu\text{m}$ and $18 \mu\text{m}$ diameter; (b) $20 \mu\text{m}$ diameter and $24 \mu\text{m}$ diameter.

5.3 2nd Group of Photodiodes

5.3.1 Device Design

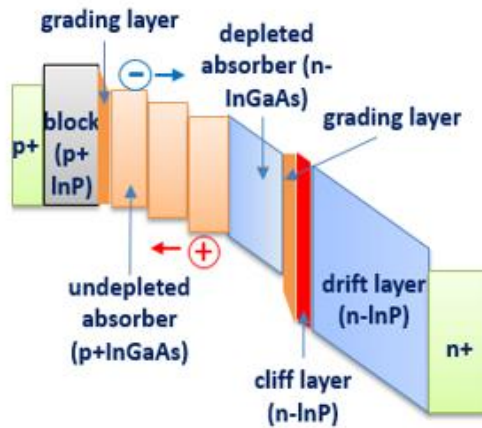
The back-illuminated MUTC photodiode structure was grown on a semi-insulating InP substrate by MOCVD. The epitaxial layers and band diagram are shown in Figure. 5-9 (a) and Figure. 5-9 (b). The growth began sequentially with 900 nm n-type doped InP contact layer, 250 nm ($1 \times 10^{16} \text{ cm}^{-3}$) and 200 nm ($1.5 \times 10^{16} \text{ cm}^{-3}$) lightly n-doped drift layers. The double drift layer design was adopted to mitigate the space charge effect at high photocurrent level and thus improve the saturation power [106]. A 50 nm -thick InP cliff layer and two InGaAsP quaternary layers were incorporated between the InGaAs absorption region and the InP drift. The InGaAs absorbing region with a total thickness of 750 nm consists of a 200 nm lightly-doped layer and three undepleted absorber layers with step graded doping of $1 \times 10^{18} \text{ cm}^{-3}$, $2.4 \times 10^{18} \text{ cm}^{-3}$ and 5

$\times 10^{18} \text{ cm}^{-3}$. A 100 nm InP blocking layer and a 50 nm p-type doped InGaAs contact layer complete the structure.

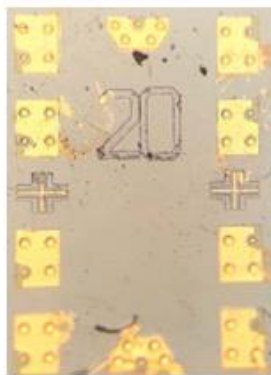
Since the material demonstrates larger absorption coefficient to light at 1064 nm compared to 1550 nm, there is strong absorption in the depleted absorber near the heterojunction at the side of incidence, which means that holes have longer transit time and holes transport limits the frequency response. To overcome this challenge, we have changed the thickness of the depleted and undepleted absorber sections to decrease the hole transit-time-limited bandwidth. The OIP3 will change with wavelength due to the change in the photo-generated carrier distribution profile, which will affect the photocurrent-dependent capacitance and thus affect the linearity. Using Matlab simulations, the doping and thicknesses of the cliff layer and the absorber were modified to achieve high linearity. With respect to the responsivity, the absorption coefficient and photon energy at 1064 nm are key design considerations. Crosslight simulations were used to design the absorber thickness and doping profile to ensure a responsivity of 0.63 A/W at 1064 nm. In summary, the thickness and doping of each layer were designed to optimize responsivity, bandwidth and linearity at 1064 nm.

Contact layer InGaAs, p+, Zn, 2×10^{19} , 50nm
InP, p+, Zn, 2×10^{18} , 100nm
Grading InGaAsP, Q1.1, p+, Zn, 5×10^{18} , 15nm
Grading InGaAsP, Q1.4, p+, Zn, 5×10^{18} , 15nm
Un-depleted absorber InGaAs, p+, Zn, 5×10^{18} , 150nm
Un-depleted absorber InGaAs, p+, Zn, 2.4×10^{18} , 200nm
Un-depleted absorber InGaAs, p+, Zn, 1×10^{18} , 200nm
Depleted absorber InGaAs, n, Si, 1×10^{18} , 200nm
Grading InGaAsP, Q1.4, n, Si, 1×10^{18} , 15nm
Grading InGaAsP, Q1.1, n, Si, 1×10^{18} , 15nm
Cliff layer InP, n, Si, 2.8×10^{17} , 50nm
Drift layer InP, n, Si, 1.5×10^{16} , 200nm
Drift layer InP, n, Si, 1×10^{16} , 250nm
InP, n+, Si, 1.0×10^{18} , 100nm
InP, n+, Si, 1.0×10^{18} , 900nm
InP, semi-insulating substrate, Double side polished

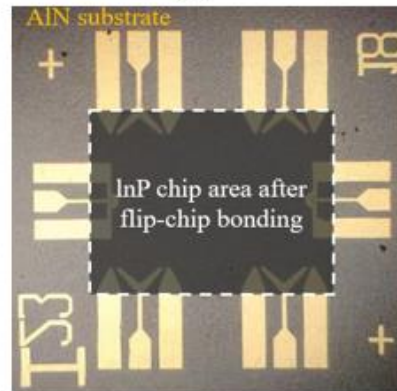
(a)



(b)



(c)



(d)

Figure 5-9. (a) Schematic cross section of InGaAs-InP MUTC photodiodes. (b) Band diagram of MUTC photodiodes. (c) Photomicrograph of photodiodes. (d) Photomicrograph of an AlN submount with CPW pads.

Devices with diameters from 10 μm to 20 μm were fabricated using a double mesa method. The first mesa etch stopped at the n-contact layer, which defined the p-mesa. The second mesa was etched into the semi-insulating InP substrate. As shown in Figure. 5-9(c), the p-contact is a single metal contact pillar while the n-contact consists of several isolated contact pillars distributed evenly on the n-mesa. Figure. 5-9 (d) is a photograph of an AlN submount with six sets of CPWs corresponding to two photodiodes and four balanced-photodiode pairs on the InP chip. The white

dashed lines indicate the position of the InP chip after flip-chip bonding. The bonding contact design decreases the overlap between the RF signal pads on the AlN submount and the n-contact layer on the device and thus reduces the parasitic capacitance.

5.3.2 Device Characterization

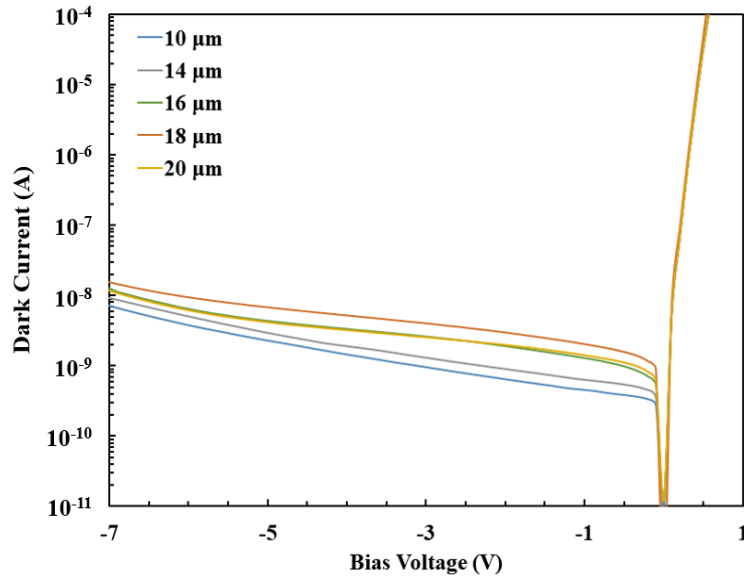


Figure 5-10. Dark current versus voltage for photodiodes with diameters from 10 to 20 μm .

Figure. 5-10 shows the dark current versus bias voltage characteristics. The dark current were in the range $10^{-9} \sim 10^{-7}$ A at -7 V.

Figure 5-11 shows measured responsivity of a 10 μm -diameter photodiode when the input power increases from 1 mW to 20 mW. The measured responsivity is 0.63 A/W at 1064 nm and is independent of photodiode diameter when the bias is -7 V at room temperature.

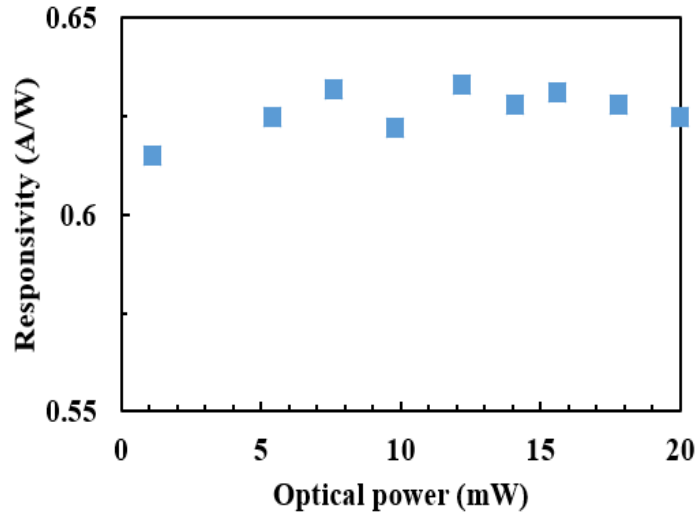


Figure 5-11. Measured responsivity of a 10 μm -diameter photodiode.

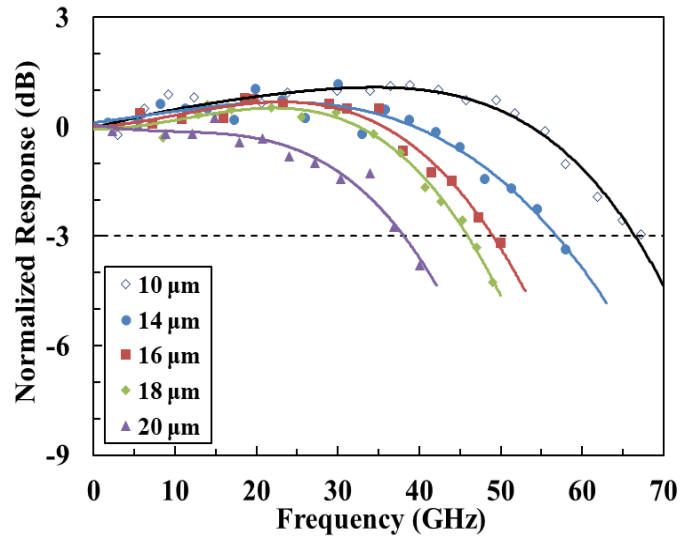


Figure 5-12. Measured frequency response of photodiodes with various diameters.

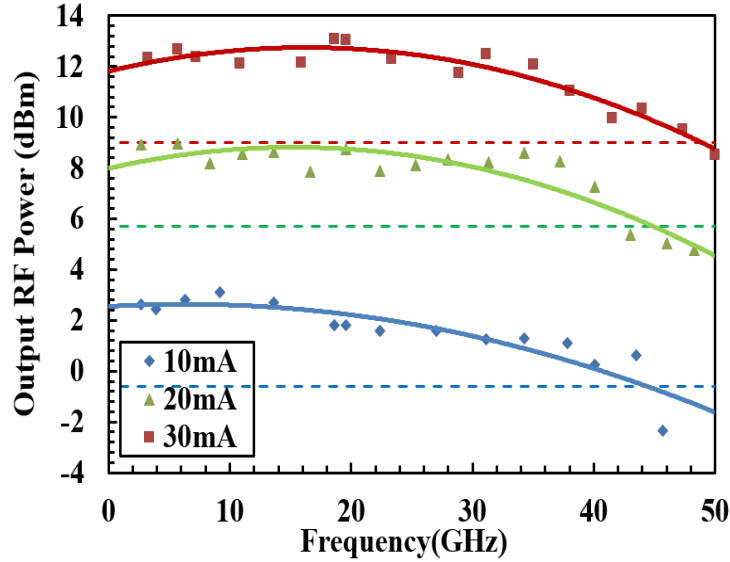


Figure 5-13. Measured frequency response of a 16 μm -diameter photodiode.

All devices under test were placed on a copper head sink. The frequency response was measured at -7 V at room temperature. As shown in Figure. 5-12, the 10 μm -, 14 μm -, 16 μm -, 18 μm - and 20 μm -diameter photodiodes exhibit 3 dB bandwidths of 65 GHz, 58 GHz, 49 GHz, 46 GHz, and 39 GHz, at 20 mA, 30 mA, 40 mA, 45 mA, and 50 mA photocurrent levels, respectively. The smaller devices exhibit larger peaking due to the high impedance transmission line. The frequency responses of the 16 μm -diameter photodiode for various photocurrents are shown in Figure. 5-13. One important figure of merit for photodiodes is the bandwidth efficiency product (BEP), which is the product of 3 dB bandwidth and quantum efficiency. The photodiode with 10 μm -diameter exhibits a record high bandwidth efficiency product of 41 GHz at 1064 nm.

As shown in Figure. 5-14, the photodiodes with 10 μm -, 14 μm -, 16 μm -, 18 μm - and 20 μm -diameters exhibit 15 dBm, 17.1 dBm, 17.6 dBm, 18.9 dBm and 21.7 dBm RF output power, respectively, at -10 °C. The measured saturation characteristics are summarized in Table 5-2. It can be observed that the compression increases initially with the photocurrent due to the self-induced field and then drops due to saturation. The smaller devices exhibit larger current-induced field in

the absorption layer. It was shown that the potential gradient induced by the electric field is inversely proportional to the device active area [82].

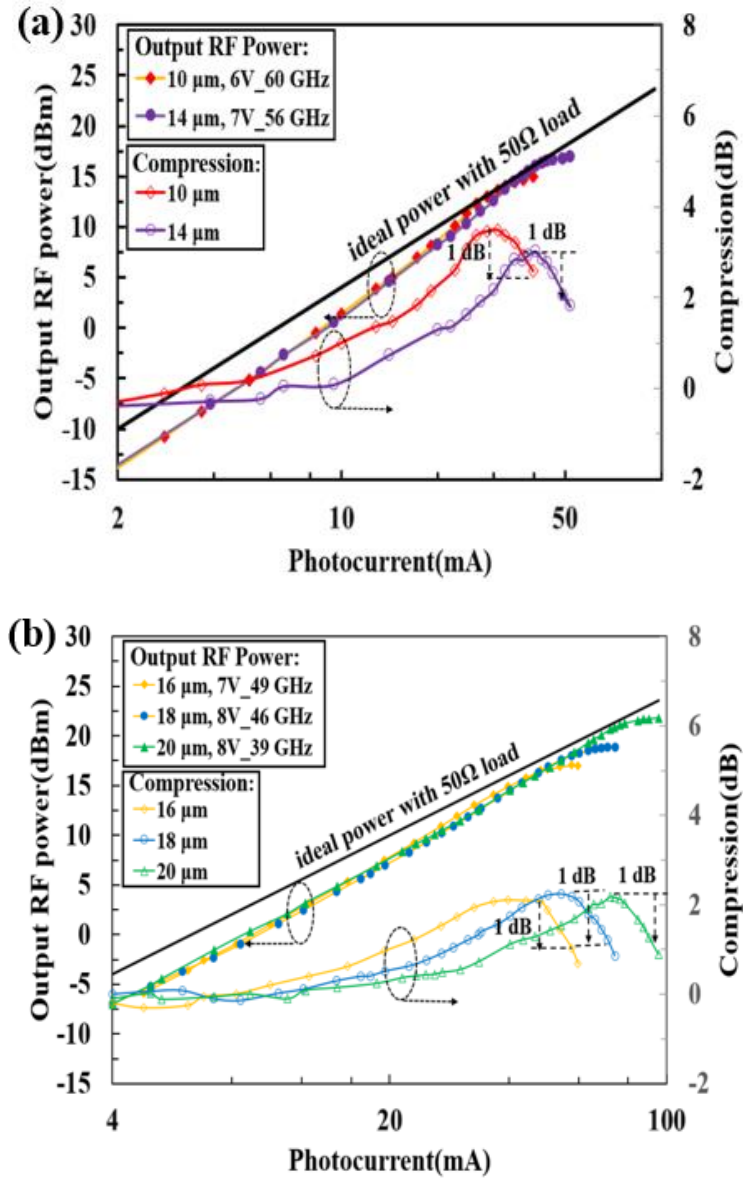


Figure 5-14. RF output power and power compression versus photocurrent for photodiodes with: (a) 10 μm -, 14 μm -, (b) 16 μm -, 18 μm - and 20 μm - diameters.

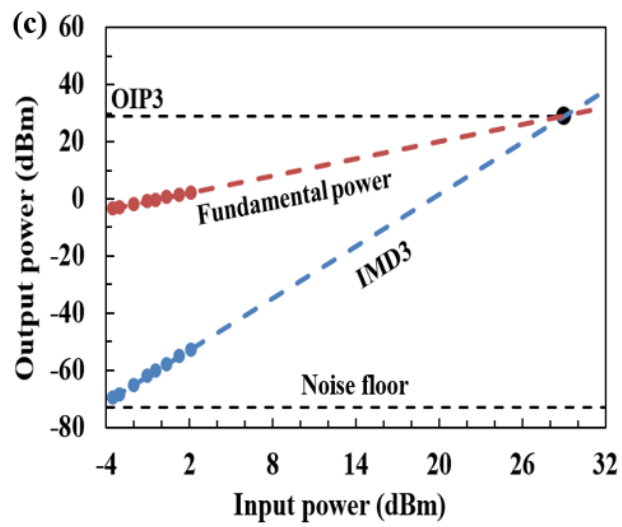
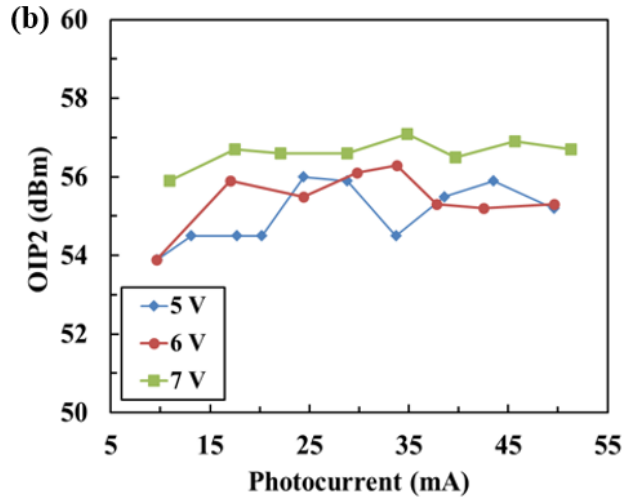
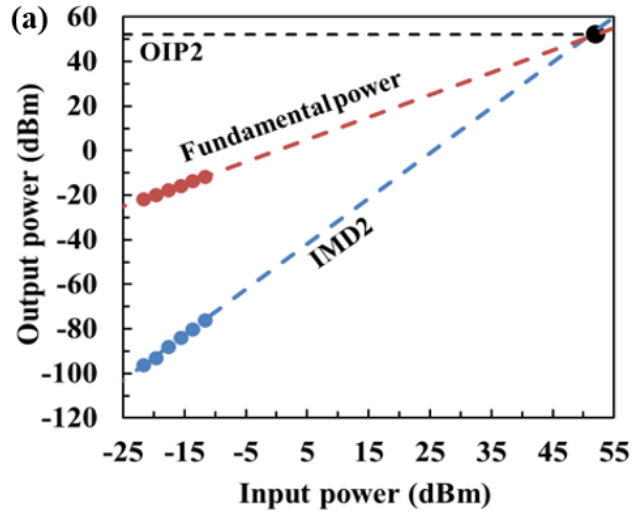
Table 5-2. Saturation characteristics.

Diameter	Measured frequency	Saturation current	Saturation power
10 μm	60 GHz	40 mA	15 dBm
14 μm	56 GHz	50 mA	17.1 dBm
16 μm	49 GHz	59 mA	17.6 dBm
18 μm	46 GHz	72 mA	18.9 dBm
20 μm	39 GHz	95 mA	21.7 dBm

The second-order and third-order intermodulation distortion was measured with a two-tone setup. The optical signal at 1064 nm was externally modulated at frequencies of f_1 and f_2 by Mach–Zehnder modulators. The modulation depth was kept at a low value and the modulators were accurately biased at the quadrature point to minimize the nonlinear response of the modulators. The output fundamental signal at f_1 and f_2 , the IMD2 signal at f_2+f_1 and the IMD3 signal at $(2f_2-f_1)$ and $(2f_1-f_2)$ were detected by a spectrum analyzer.

As shown in the Figure. 5-15, the measured fundamental power increases with the input power at a slope of 1, IMD2 increases with the input power at the slope of 2 and the IMD3 increases with the input power at the slope of 3. As shown in the Figure. 5-15 (a), the intercept power of linear extrapolations of IMD2 and fundamental power lines is defined as the OIP2. At 20 GHz, the 16 μm -diameter photodiode achieves peak OIP2 value of 57 dBm at voltage of -7 V and photocurrent of 35 mA.

The photocurrent-dependent OIP3 values under bias voltages of -5 V, -6 V and -7 V at 40 GHz are shown in the Figure. 5-15 (d). When the photocurrent is 29 mA, the 16 μm -diameter photodiode achieves peak OIP3 value of 33 dBm at -6 V.



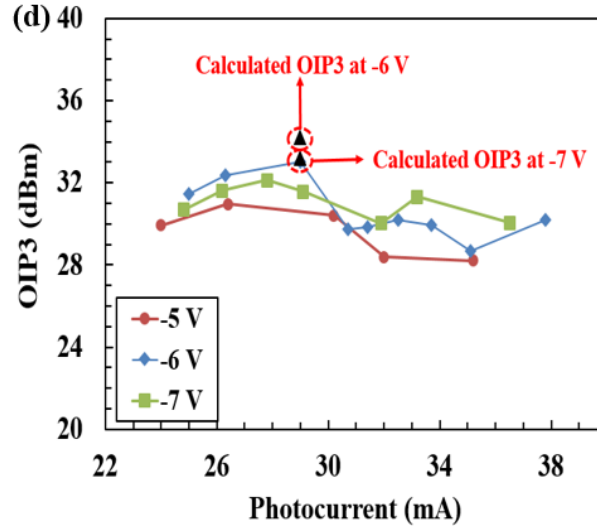
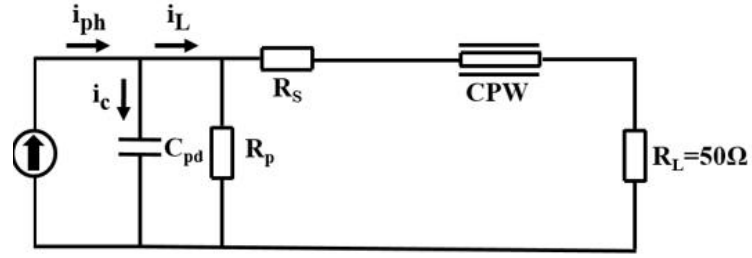


Figure 5-15. (a) Measured fundamental power and IMD2 versus input power; (b) measured OIP₂ versus photocurrent at 20 GHz for different bias; (c) measured fundamental power and IMD3 versus input power; (d) calculated and measured OIP₃ versus photocurrent at 40 GHz for different bias.

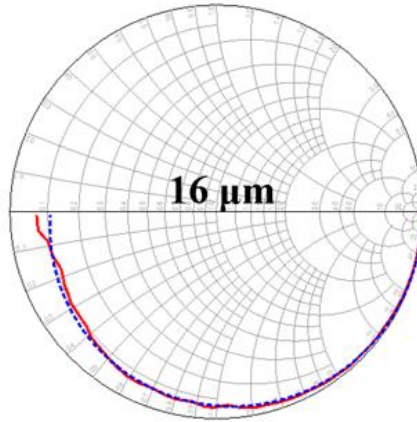
5.3.3 Nonlinear Analysis

In order to evaluate the photocurrent- and voltage-dependent nonlinear effects, a theoretical model based on equivalent circuit analysis has been developed [107]. The 1-port S-parameters without illumination were measured with a vector network analyzer up to 50 GHz and a ground-signal-ground probe. Figure. 5-16 (a) shows a photodiode circuit model developed in Advanced Design System software that includes the CPW simulation profile and the RC component. The C_{pd} , R_s , R_p , and R_L parameters represent the junction capacitance, series resistance, junction resistance and load resistances, respectively.

The measured S_{11} (solid lines) and fitted results (dotted lines) for a 16 μm -diameter photodiode from 100 Hz to 50 GHz agree well on Smith Charts. In the dark situation, the extracted R_s and C_{pd} are 10 Ω and 32 fF, respectively. It should be noted that the extracted capacitance is the same as the calculated value using the parallel-plate capacitance formula.

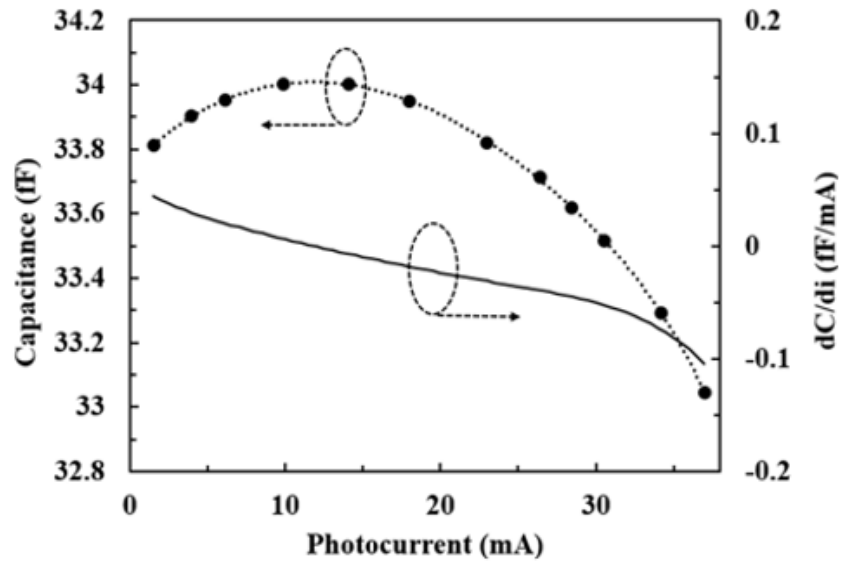


(a)



(b)

Figure 5-16. (a) Equivalent circuit of the flip-chip bonded photodiodes. (b) Measured S11 (solid line) and fitting curves (dotted line) for a 16 μm -diameter photodiode.



(a)

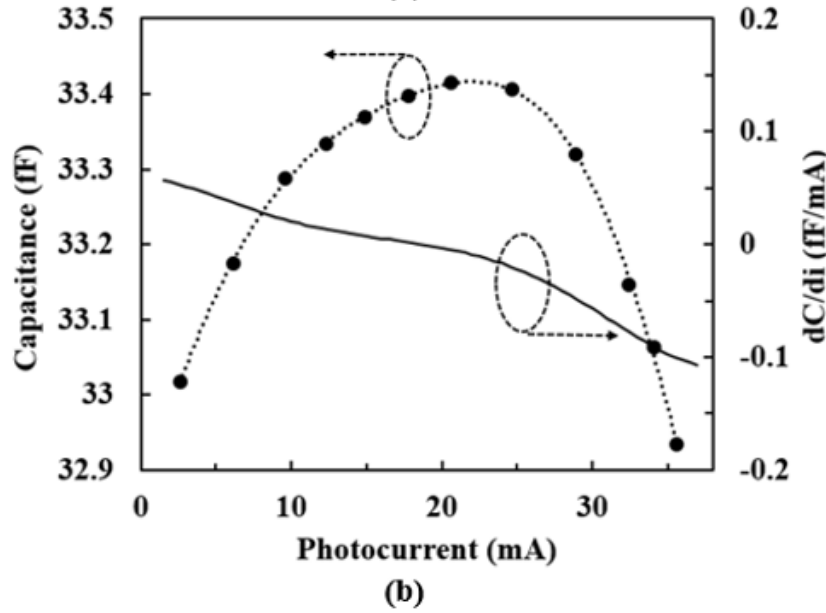


Figure 5-17. Calculated capacitance (left axis) and differential capacitance (right axis) from the imaginary part of the 16 μm -diameter photodiode impedance versus photocurrent at 40 GHz and bias voltages of: (a) -6 V and (b) -7 V.

Figure. 5-17 shows the 16 μm -diameter photodiode capacitance obtained from the imaginary part of the Z-parameter versus photocurrent at 40 GHz. The 1 port Z-parameter was characterized with the same setup as the S-parameter. The influence of the CPW was excluded from the impedance of the photodiode using Mason's rule. The differential capacitance was obtained using polynomial fitting to the measured data. Initially the capacitance increases and then decreases, which means the current differential capacitance changes from positive to negative. The photocurrent increase will reduce voltage across the photodiode because the voltage drop across the series resistance becomes a larger portion of the total voltage, resulting in an increase of voltage-controlled capacitance. Therefore, the positive differential capacitance is observed due to the significant voltage drop caused by the series resistance. Under high optical illumination, the negative differential capacitance can be explained as the screening of the space-charge field within the depleted region. The photo-generated carriers in the depleted area screen the ionized donor and

acceptor charge. According to Poisson's equation, the depletion region needs to penetrate into the high-doped region. We observe a differential capacitance of -0.05 fF/mA and -0.052 fF/mA at -6 V and -7 V at 29 mA, respectively. .

The 16 μm-diameter photodiode capacitance versus voltage at 40 GHz was also measured and is shown in Figure. 5-18. The voltage-dependent capacitance is due to the low doping concentration of the InGaAs absorption and InP drift layers. The large dependence of capacitance on voltage is attributable to Zn diffusion in the InGaAs layer. The voltage differential capacitance at -6 V is 0.2 fF/V.

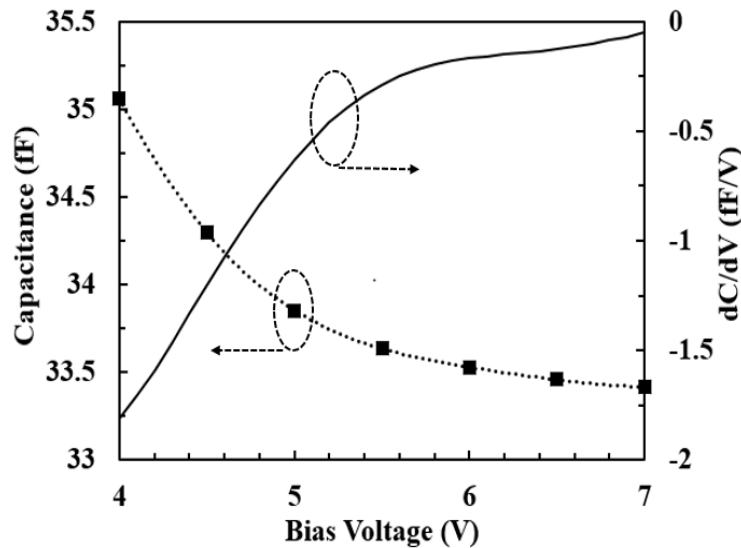


Figure 5-18. Calculated capacitance (left axis) and differential capacitance (right axis) from the imaginary part of the 16 μm-diameter photodiode impedance versus bias voltage at 40 GHz and photocurrent of 29 mA.

According to the circuit model in Figure. 5-16 (a), the current in the photodiode can be calculated from the following equation:

$$I_{ph} = I_L + \frac{d}{dt}(C_{pd} \times I_L R) \quad (5.1)$$

where I_L is the current across the load and R is the sum of the series and load resistances. The one-tone setup was adopted in the circuit analysis for simplification [102] and the AC photocurrent

is given as: $I_{ph} = I_0 e^{j\omega t}$, where I_0 is the product of the responsivity, the average optical input power, and the modulation depth. It has been previously reported [103] that the effect on OIP3 caused by voltage- and photocurrent-dependent responsivity is negligible at high frequency. To take the voltage- and photocurrent-dependent capacitance into consideration, the junction capacitance is defined as $C_{pd} = C_0 + \frac{\partial C}{\partial V} \times \Delta v + \frac{\partial C}{\partial i} \times \Delta i = C_0 + \frac{\partial C}{\partial V} \times (i_L R) + \frac{\partial C}{\partial i} \times \Delta i_{ph}$ with static capacitance C_0 . The current equation based on the circuit model can be obtained by substituting the photocurrent across the photodiode and the junction capacitance into (5.1). I_L can be expressed in a harmonic series of $i_1 e^{j\omega t} + i_2 e^{2j\omega t} + i_3 e^{3j\omega t} + \dots$. Matching both sides of the terms with the same frequency, the fundamental, second-order harmonic and third-order harmonic current components can be expressed as:

$$I_1 = \frac{I_0}{1 + j\omega R C_{pd}} \quad (5.2)$$

$$I_2 = -2j\omega \times \frac{i_1^2 R^2 \frac{\partial C_{pd}}{\partial V} + i_1 I_0 R \frac{\partial C_{pd}}{\partial i}}{1 + 2j\omega R C_{pd}} \quad (5.3)$$

$$I_3 = -3j\omega \times \frac{2i_1 i_2 R^2 \frac{\partial C_{pd}}{\partial V} + i_2 I_0 R \frac{\partial C_{pd}}{\partial i}}{1 + 3j\omega R C_{pd}} \quad (5.4)$$

The measured IMD3 with the two-tone setup is 9.6 dB larger than the ideal simulated result with the one-tone setup because the coefficient of $\cos(2\omega_2 - \omega_1)$ after expanding $[\cos(\omega_1) + \cos(\omega_2)]^3$ is 3 times as large as the coefficient of $\cos(3\omega_1)$. In order to compare with the measured two-tone OIP3, a factor of 4.8 dB should be subtracted from the simulation result. The calculated OIP3 based on (5.2)-(5.4) due to the capacitive effect is 34.2 dBm and 33.2 dBm under -6 V and -7 V at 29 mA, respectively. The third-harmonic distortion calculation achieves close agreement with the measurement. The slight difference can be explained as the variation of the S-parameter of the CPW and the difference between the inductive peaking design and the device fabrication.

The above analysis indicates that the voltage- and photocurrent-dependent capacitance are two primary factors that impact the linearity of this MUTC structure. The nonlinear characteristics can be further improved by increasing the doping concentration in the undepleted absorber and reducing Zn diffusion into the depleted absorber, which will reduce the change in depletion depth and capacitance with voltage. Additionally, a small series resistance is helpful to minimize the photocurrent-controlled capacitance and can thus enhance the OIP3.

5.4 Conclusion

In this Chapter, two groups of high-speed, high-power and high-linearity photodiodes working at 1064 nm were designed and investigated. The photodiodes in the 1st group exhibited responsivity of 0.46 A/W and low dark current of 1 nA at -8 V. The 15 μm -, 18 μm -, 20 μm - and 24 μm -diameter photodiodes achieved bandwidths of 55, 41, 32 and 27 GHz with saturation RF power of 18.6, 19.4, 23.4 and 24.4 dBm, respectively. Frequency response analysis using parameters extracted from S_{11} measurements showed that the RC component is the primary limiting factor for devices with diameter $> 15 \mu\text{m}$.

Based on the analysis of the 1st device group, the redesigned 2nd group showed a higher responsivity of 0.63 A/W and improved bandwidth. The photodiode exhibited a record high bandwidth efficiency product of 41 GHz at 1064 nm. The RF output power and bandwidth of photodiodes in the 2nd group with diameters of 10 μm and 20 μm were 15 dBm at 60 GHz and 21.7 dBm at 39 GHz, respectively. The measured third-order output intercept point showed a high linearity of 33 dBm at 40 GHz. A circuit analysis based on Z-parameter extraction indicated that voltage-dependent and photocurrent-dependent capacitance components are major nonlinear mechanisms.

Chapter 6 High-Performance Analog Photonic Link

6.1 Introduction

Analog photonic links are promising alternatives to coaxial cable systems commercial wireless telecommunication networks, fiber-optic antenna remoting, and phased-array radar systems since optical fibers provide large bandwidth, low loss, superior immunity to electromagnetic interference, and reduced size [1, 2]. In recent years, the 1064 nm wavelength has attracted attention for photonic systems as a result of the availability of ultra-low noise Nd:YAG lasers and high-power ytterbium-doped fiber amplifiers. These devices offer the potential for high-gain and low-noise 1064 nm analog optical links [39, 40]. For 5G mobile networks [108, 109] and remote sensing [110, 111] applications, the Ka frequency band (26.5–40 GHz) has been increasingly used due to the large available bandwidth and capability of high-resolution radar. Previously, a 1064 nm RF photonic link with gain of -15 dB was demonstrated at 30 GHz [112].

The intensity modulation with direct detection scheme with an external intensity optical modulator is commonly used in analog photonic links. For IM/DD links, much work has been done to improve the gain, the noise figure, and the spurious free dynamic range [113-115], which are three key figures of merit of an analog photonic link. In order to reduce noise, balanced detection can be used to cancel the relative intensity noise from the laser and the amplified spontaneous emission noise from a YDFA [41]. In addition, balanced detection has advantages in suppression of even-order harmonics and doubling the optical power handling capability of a photonic link [44, 116]. Another approach to reduce noise and enhance signal-to-noise ratio (SNR) is the low-bias modulation technique, which can suppress the optical carrier power [117, 118]. In [119], this approach achieved record noise figure and gain in the 6–12 GHz band. However, it should be noted

this improvement is achieved at the price of increased even-order distortion. In order to improve linearity and the link SFDR, methods to suppress intermodulation distortion, such as optical carrier band processing [120], parallel Mach–Zehnder modulators [121] and digital signal post-processing [122], have been demonstrated in IM/DD links. However, the gain and noise figure usually significantly degrade due to the loss contributed by the additional components.

High-power photodiodes are key components in analog photonic links as the figures of merit of the link are generally improved at high photocurrent. Linearity at high frequency is also critical in order to achieve large SFDR.

In this chapter, I demonstrate two analog photonic links with different noise reduction techniques without electronic amplification. In the first link, I use balanced detection with a quadrature-biased Mach–Zehnder modulator for noise cancellation. The second link works at low bias modulation for improved signal-to-noise ratio with a single photodetector.

6.2 Figures of Merit

Several figures of merit are used to determine a high-performance photonic link, which include link gain, noise figure and dynamic range. The definitions and measurement techniques of these figures of merit are introduced in this section.

6.2.1 Link Gain

Link gain substantially impacts the noise figure and dynamic range. It is defined as the ratio of the output RF signal power from the photodetector to the input RF signal power into the optical modulator. For a photonic link using an intensity modulator, the small-signal RF gain g can be expressed as [2]:

$$g = \frac{P_{RF,out}}{P_{RF,in}} = \frac{\beta^2 I_{dc}^2 \sin^2(\phi_{dc}) Z_o Z_{in} \pi^2}{V_\pi^2 [1 + \beta \cos(\phi_{dc})]^2} |H_{pd}|^2 \quad (6.1)$$

where I_{dc} , ϕ_{dc} , Z_o , Z_{in} , V_π and $|H_{pd}|$ are the dc photocurrent, phase shift created by the DC bias on the MZM, load impedance, input impedance of the MZM, halfwave voltage of the MZM, and transfer function of the photodetector, respectively. β is related to the extinction ratio (δ) of the MZM as $\beta = \frac{\delta-1}{\delta+1}$, Equation (6.1) illustrates that the gain increases quadratically with the photocurrent for a given value of V_π and bias point of the modulator.

When the modulator is biased away from quadrature toward its null point, the RF gain for the low-biased link is higher than that for the quadrature-biased link as shown in (6.1).

During the measurement, the RF signal is generated by a signal generator. The output of the signal after photodiodes is measured by an electrical spectrum analyzer. Then, RF link gain can be calculated according to (6.1). It should be noted that the cable loss between signal generator and MZM and loss between ESA and the probe need to be calibrated.

6.2.2 Noise Figure

The noise figure, NF, is a measure of the degradation of the signal-to-noise ratio. NF can be expressed as [65]:

$$NF = 10 \log \left(\frac{N_{out}}{g k T_s B} \right) \quad (6.2)$$

where k , T_s , B , g and N_{out} are Boltzmann's constant, standard noise temperature, the resolution bandwidth, link gain, and total output noise of the photodiode, respectively. The total noise consists of thermal noise from the photodiodes, amplified thermal noise, shot noise, RIN from laser, and ASE noise from the YDFA. It can be expressed as [2]:

$$N_{out} = (1 + g) k T_s B + 2q I_{dc} Z_o |H_{pd}|^2 B$$

$$+ \left[RIN_{Laser} + \frac{2hf_0F_0}{P_{in}} + \left(\frac{hf_0F_0}{P_{in}} \right)^2 B_0 \right] I_{dc}^2 Z_o |H_{pd}|^2 B \quad (6.3)$$

where RIN_{Laser} , h , f_0 , F_0 , P_{in} and B_0 are laser RIN, Planck's constant, optical frequency, noise factor of the YDFA, optical input power into the YDFA, and optical bandwidth, respectively.

The first term on the right-hand side is the total thermal noise including amplified input thermal noise and the thermal noise generated in the photodiode. The second term represents the shot noise. The laser RIN, YDFA noise due to signal-spontaneous beating, and YDFA noise due to spontaneous-spontaneous beating are included in the third term. In our experiment, the laser noise is relatively low. A narrow bandwidth optical filter was used to suppress the spontaneous-spontaneous beat noise from the YDFA. Therefore, the primary excess noise was the signal-spontaneous beat noise. It should be noted that the noise from the YDFA can be mitigated by high input optical power. Balanced detection can reduce the common-mode noise, but it relies on matching of the two optical paths. In addition, both the shot-noise-induced and RIN-induced noise components can be reduced by the low bias technique due to high gain as shown in (6.2).

Typically, there are three methods to measure the noise figure, the noise figure meter method, the gain method and the Y factor method. In this work, the gain method was adopted to measure the noise figure as RF gain is known at a fixed current in the analog photonic link.

The thermal noise power at the input of the link can be expressed as: $P_{in} = kT_s B$. At room temperature (290 K), the noise power spectral density is -174 dBm/Hz. The equation (6.2) can be simplified as following:

$$NF = N_{out} + 174 \text{ dBm/Hz} - g \quad (6.4)$$

where N_{out} is the measured total output noise power spectral density and g is the link RF gain in unit of dB.

6.2.3 Spurious Free Dynamic Range

The SFDR characterizes the range of output powers over which all spurious signals are less than or equal to the output noise floor. The SFDR depends on the output noise, nonlinearity of the MZM, and the linearity of the photodiodes. The SFDR₃ is important because the third-order intermodulation distortion signal is commonly within the bandwidth of the narrow electrical filter in a suboctave system and it can be expressed as:

$$SFDR_3 = \left(\frac{OIP3}{N_{out}} \right)^{\frac{2}{3}} \quad (6.5)$$

where OIP3 is the third-order intercept point. If the nonlinearity of the photodiode is taken into consideration, the cascade OIP3 for two nonlinear devices is given as [2]:

$$OIP3 = \left(\frac{[1+\beta\cos(\phi_{dc})]^2}{4\beta^2 I_{dc}^2 \sin^2(\phi_{dc}) Z_o |H_{pd}|^2} + \frac{1}{OIP3_{pd}} \right)^{-1} \quad (6.6)$$

where $OIP3_{pd}$ is the OIP3 for photodiode. Equation (6.6) describes the impact that a nonlinear photodiode with third-order output intercept points will have on an IM/DD system. The intercept point of a particular photodiode will be a function of dc photocurrent and bias voltage. The OIP3 depends on the bias point of the modulator, the link gain, and linearity of photodiode.

The measurement method for OIP3 has been shown in Chapter 3. With the OIP3 value and measured output noise power spectral density, the SFDR₃ can be calculated according to equation (6.5).

6.3 Balanced Photodiodes Performance

6.3.1 Device Design

To cancel the common mode noise in the photonic link, I designed balanced photodiodes as

shown in Figure. 6-1, using the same epi as shown in Figure. 5-9 (a). For this work, the photodiode chips are flip-chip-bonded to diamond submount by thermo-compression Au-Au bonds with coplanar waveguides.

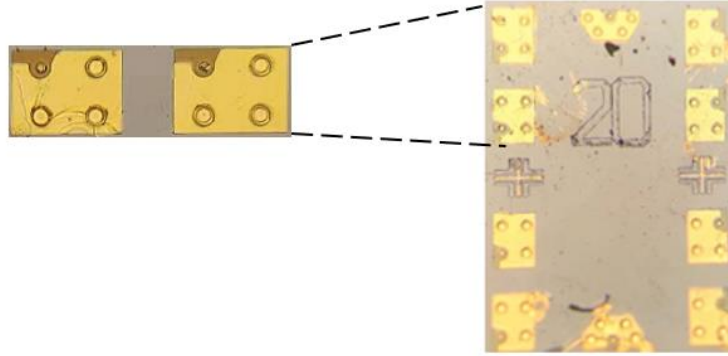


Figure 6-1. Photomicrograph of balanced photodiodes.

For balanced detection, when the input signals are in differential mode, the output signals are added. When the input signals are in common mode, the output signals are cancelled. As shown in the photomicrograph, the distance between the two photodiodes is $250\ \mu\text{m}$, which matches the distance between lenses of the fiber array. Compared to two discrete photodiodes connected with an external circuit, the monolithic integration provides compact size, better RF performance and higher common mode suppression ratio.

CMRR is an important figure of merit, which is defined as the difference between the differential mode and common mode RF output power [123]. It is used to characterize the similarity of the two photodiodes in a balanced configuration and how well the common mode noise can be cancelled in a photonic link. The asymmetrical parts in the device design or the RF probe design usually cause the differences of the frequency response for two devices. Therefore, the symmetrical design of the coplanar waveguide and the chip is required for high CMRR.

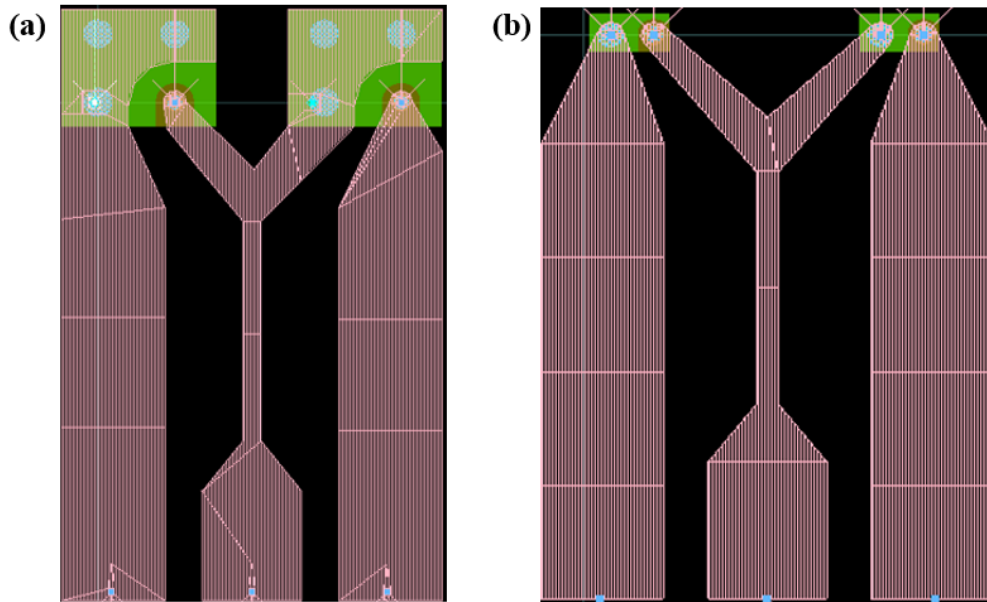


Figure 6-2. (a) Old version CPW design for our balanced photodetector; (b) New version CPW design for the balanced photodetector.

In the old version, the CPW design in Figure. 6-2 (a), both the RF grounds and the RF signals are not symmetric. To improve the similarity and RF performance of our balanced photodetector at high frequency, I designed a new CPW for the balanced photodetector. In the new design, the structure of the CPW is symmetric.

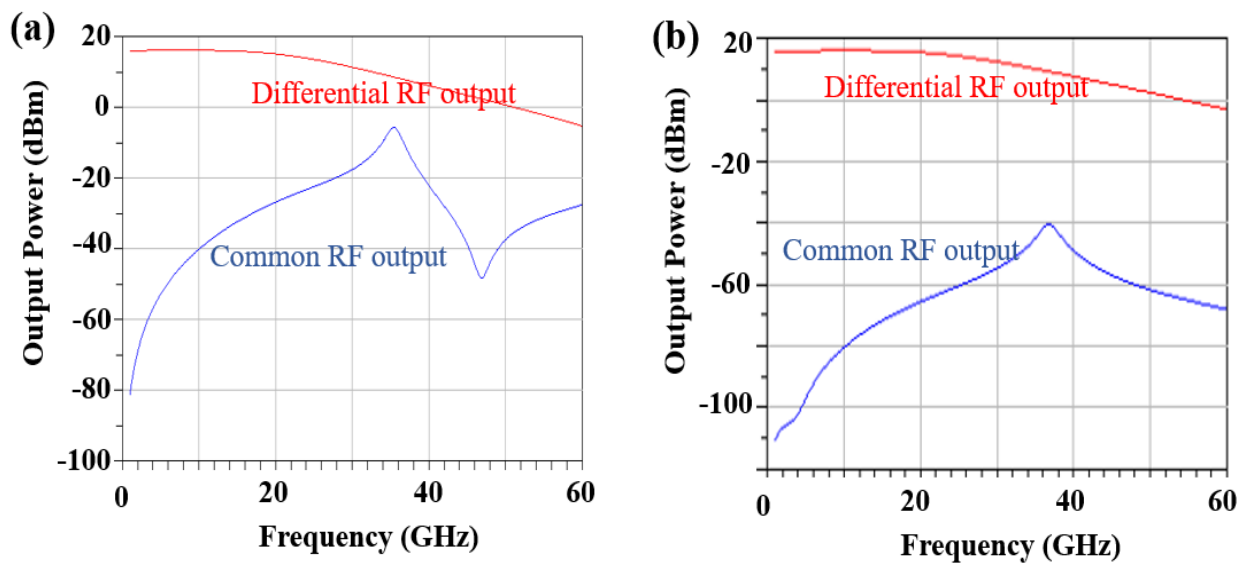


Figure 6-3. Simulated RF output power for (a) Old version CPW design; (b) New version CPW design.

To verify that, the simulation for the differential mode and common mode RF output power were conducted in ADS. As shown in Figure 6-3, the common mode RF output is lower for the new version of the CPW design at different frequency and thus the CMRR is higher. Therefore, the symmetric design was adopted to improve the noise cancellation ability at high frequency.

6.3.2 Device Characterization

The frequency response for balanced photodiodes was measured using an optical heterodyne setup. Light from two lasers near 1064 nm wavelength was used to generate a beat signal with ~100% modulation depth. The beat frequency was tuned by changing the temperature and thus the wavelength of one laser. The signal was then split into two branches. The signal was monitored by a commercial photodiode and a spectrum analyzer at the first branch. The second output branch was amplified by an YDFA and the output signal power was adjusted by an optical attenuator. The signal was then divided equally to feed the balanced pair of photodiodes via a coupler. A variable optical delay line (ODL) in one of the paths was used to control the phase difference of the optical signals. The RF power from the photodiode was detected by an RF power meter. All devices under test were placed on a copper heat sink at room temperature. The measured responsivity for a discrete photodiode was 0.63 A/W at 1064 nm when the bias was -7 V as shown in Chapter 5..

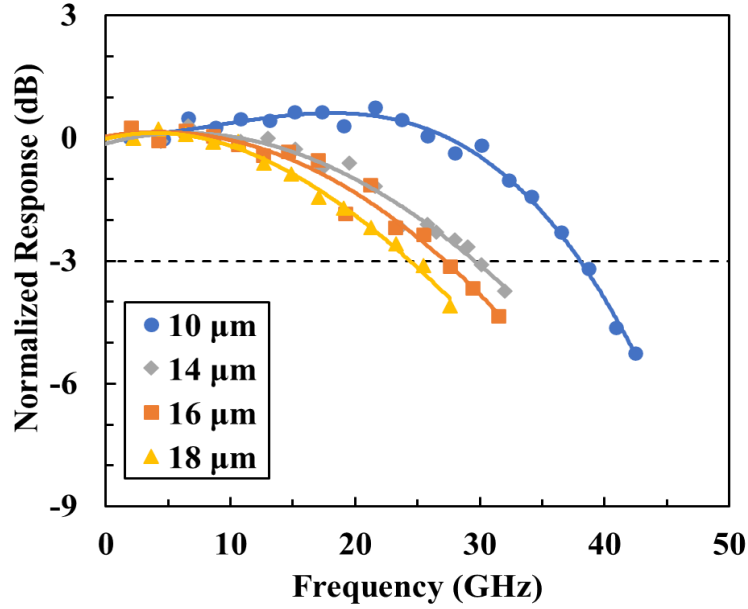


Figure 6-4. Measured frequency response of photodiodes with various diameters.

The bandwidth was measured at -7 V, where the device was fully depleted. As shown in Figure. 6-4, the $10\ \mu\text{m}$ -, $14\ \mu\text{m}$ -, $16\ \mu\text{m}$ -, and $18\ \mu\text{m}$ -diameter balanced photodiodes exhibit 3-dB bandwidths of 38 GHz, 29 GHz, 27 GHz and 24.5 GHz, respectively, at 20 mA photocurrent level. The smaller devices exhibit larger inductive peaking due to the high impedance transmission line. The bandwidths of $14\ \mu\text{m}$ -, $16\ \mu\text{m}$ - and $18\ \mu\text{m}$ -diameter photodiodes are approximately half the bandwidths of the discrete photodiodes with the same diameters. This is due to the fact that the balanced design has twice the capacitance of a single photodiode and the bandwidth of these photodiodes is primarily RC limited.

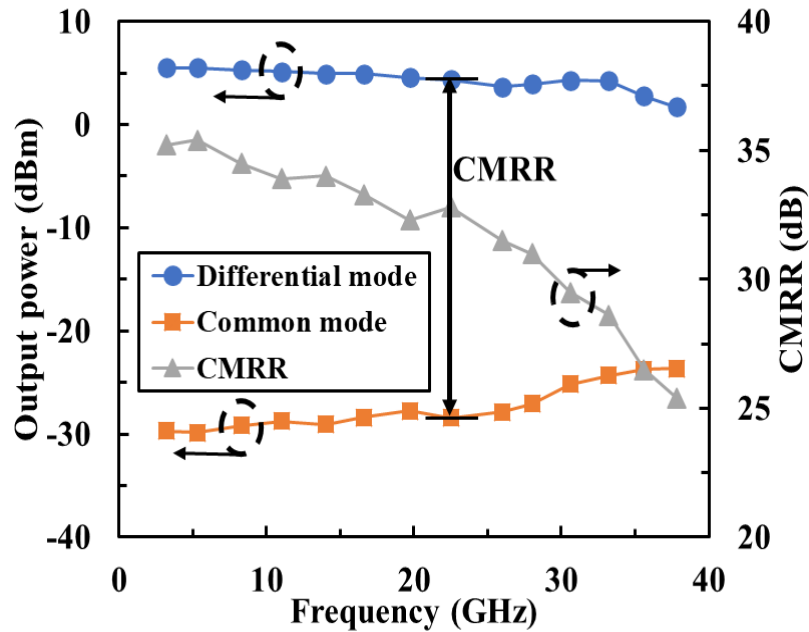


Figure 6-5. Measured frequency response of photodiodes with various diameters.

Figure. 6-5 shows the differential mode and common mode RF output power of a 10 μm -diameter balanced device at -7 V bias voltage and 6 mA photocurrent level. The CMRR remains above 30 dB for frequencies up to 30 GHz and is close to 25 dB at 38 GHz. The CMRR drops as the frequency increases due to the decrease of the RF output power and increasing divergence of the two photodiodes.

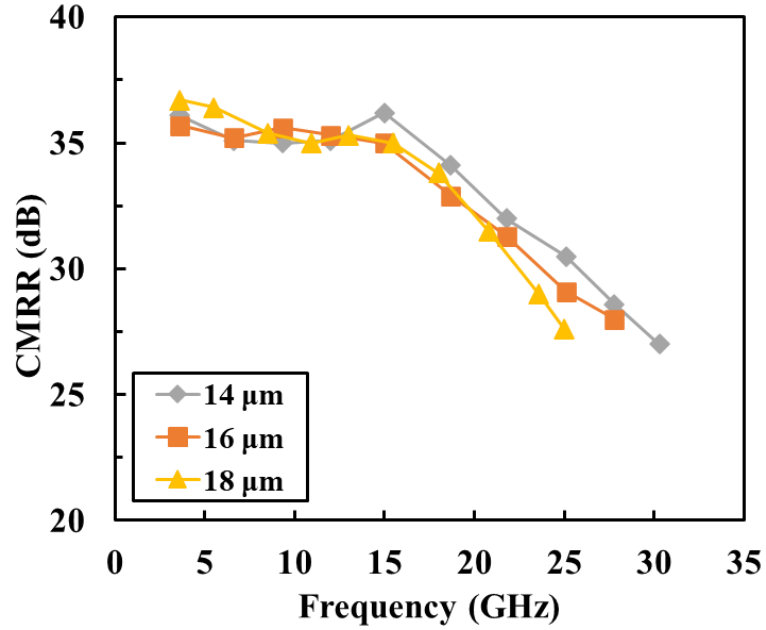
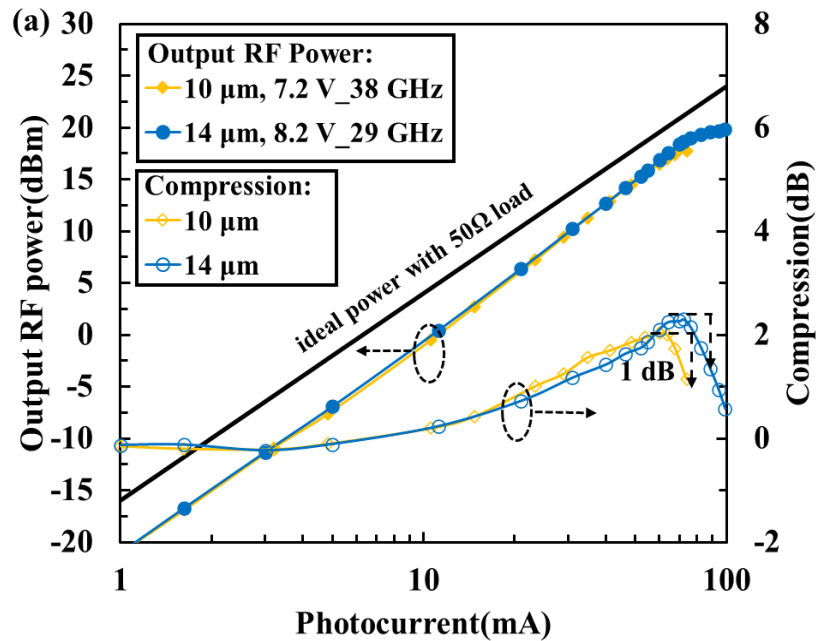


Figure 6-6. CMRR for devices with 18 μm -, 16 μm - and 14 μm -diameter.

For balanced photodiodes with 18 μm -, 16 μm - and 14 μm -diameter, CMRR is close to 35 dB at low frequency and remains above 25 dB for frequencies below the 3 dB bandwidth point as shown in Figure. 6-6.



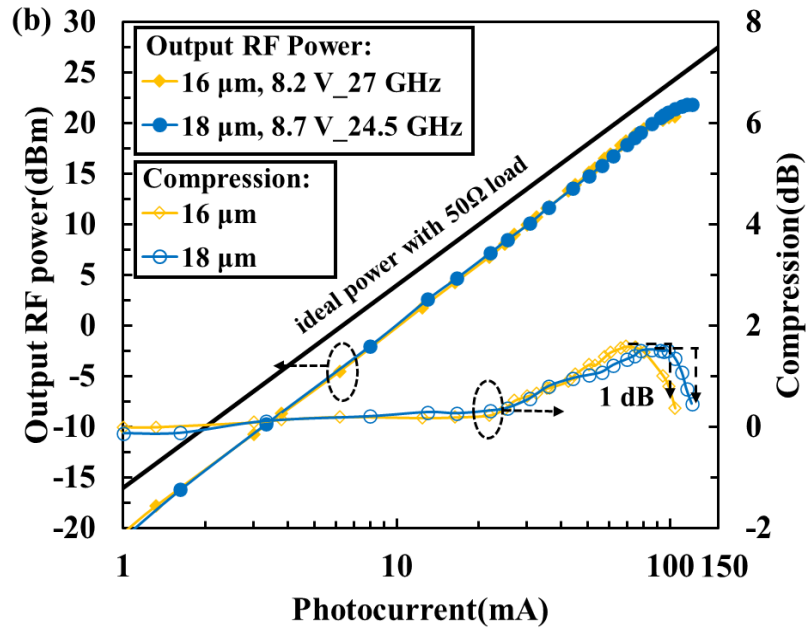


Figure 6-7. RF output power and power compression versus total photocurrent for balanced photodiodes with: (a) 10 μm -, 14 μm -, (b) 16 μm - and 18 μm -diameters.

The RF saturation characteristics were measured using the heterodyne setup described above. The saturation power was measured where the RF output power deviates 1 dB from the ideal square relationship between output power and photocurrent. As shown in Figure. 6-7, the photodiodes with 10 μm -, 14 μm -, 16 μm -, and 18 μm -diameter achieve 17.7 dBm, 19.8 dBm, 20.7 dBm and 22 dBm RF output powers with 74 mA, 98 mA, 104 mA and 120 mA saturation currents at 38, 29, 27 and 24.5 GHz, respectively. The current value is the total photocurrent flowing in the balanced photodiodes.

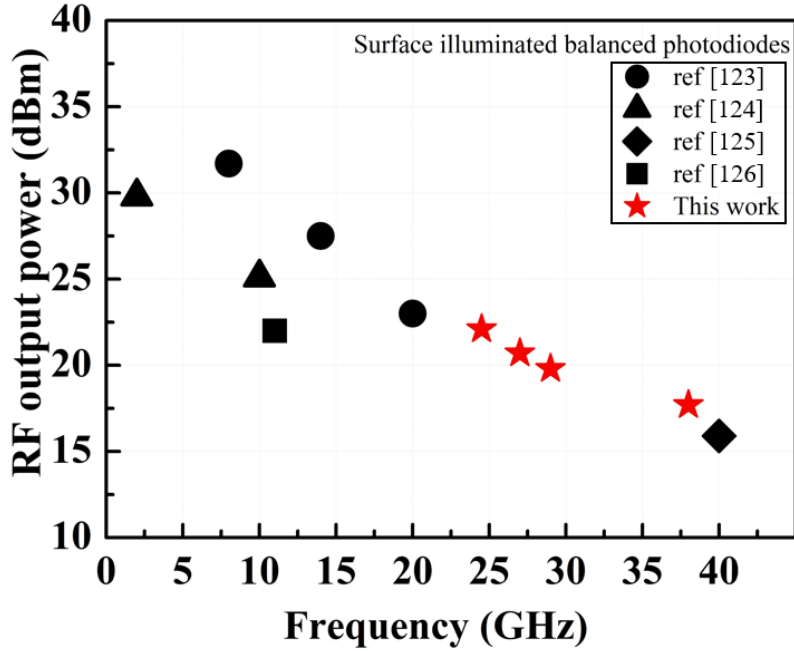


Figure 6-8. State-of-the-art maximum RF output power for balanced photodiodes versus frequency.

Figure. 6-8 shows the state-of-the-art RF output power versus frequency of balanced photodiodes [123-126]. The balanced photodiodes with optimized design in this work exhibit record-high RF output power in the Ka frequency band.

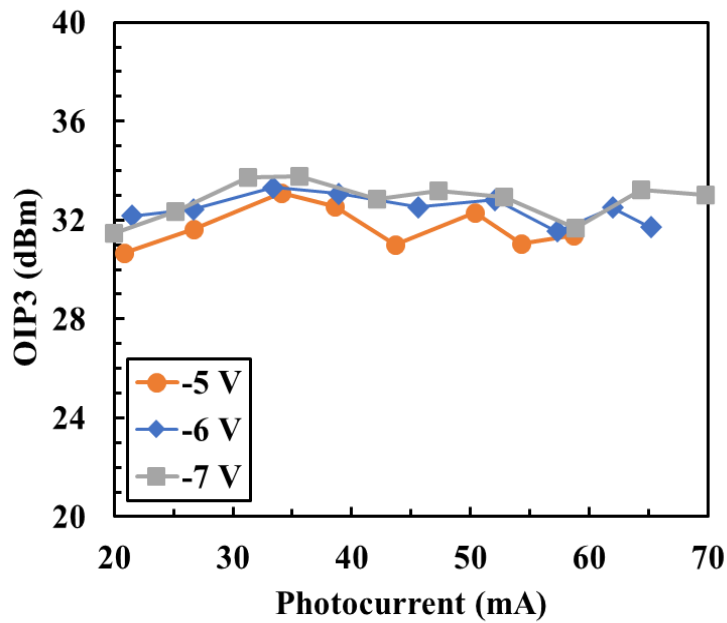


Figure 6-9. Measured OIP3 of balanced photodiodes at 38 GHz.

A two-tone OIP3 measurement setup was used for linearity characterization. During the measurement, the modulators were accurately biased at the quadrature point and the modulation depth was kept at a low value to avoid nonlinear influence from the modulators. The fundamental and third-order intermodulation distortion signals were measured with a spectrum analyzer.

The photocurrent dependence of OIP3 under reverse bias voltages of 5 V, 6 V, and 7 V at 38 GHz is shown in Figure. 6-9. At a bias voltage of -7 V, OIP3 was higher than 30 dBm for total currents up to 70 mA, and a peak value of 34 dBm was measured at photocurrent of 36 mA. According to the previous analysis, the voltage- and photocurrent-dependent capacitance dominate the linearity of this MUTC structure at high frequency.

6.4 Balanced Link Configurations

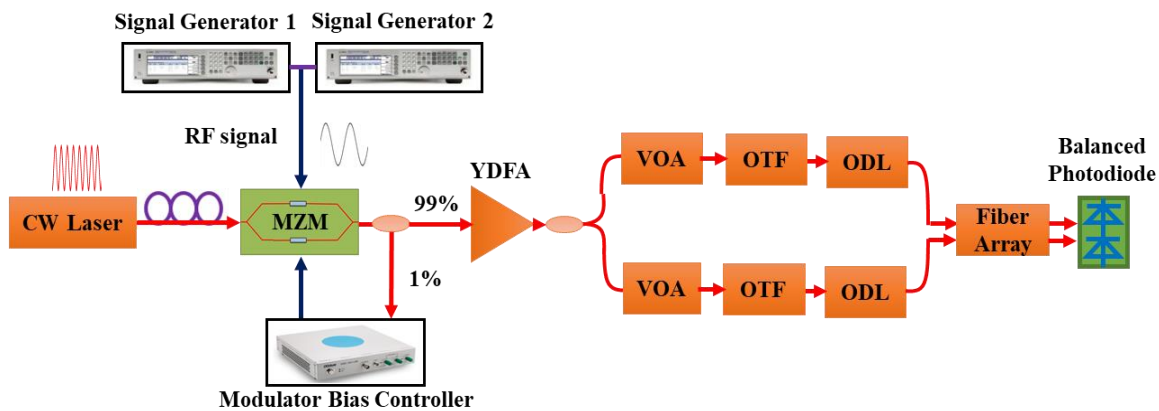
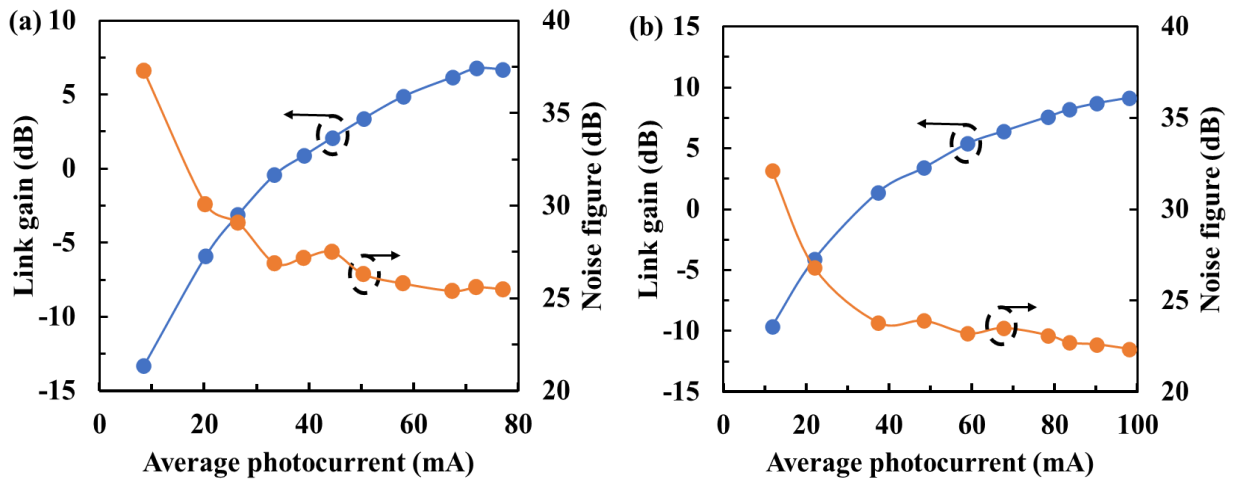


Figure 6-10. Experimental setup for balanced analog photonic link.

Figure 6-10 shows the experimental setup of the IM/DD balanced analog link that uses balanced detection. A high-power and narrow-linewidth CW laser working at 1064 nm was used as the source. The maximum output power of the laser is 20 dBm and its maximum RIN is -160 dBc/Hz. After a polarization controller, the light was coupled into an MZM. The V_{π} of this MZM is 4 V and its bandwidth is 40 GHz. A bias controller was used to ensure that the MZM was locked

at its quadrature point. The light was then amplified by a YDFA and split into two branches. In each branch of the link, an optical tunable filter (OTF) was used to remove spontaneous-spontaneous beat noise and an optical delay line was used to adjust phase. Light was coupled into the balanced photodiode with a fiber array. The output RF signal was measured by an electrical spectrum analyzer.

An ideal IM/DD link using a dual-output MZM has the potential to cancel RIN from the laser and ASE noise from the YDFA. However, a dual-output MZM that can handle high-power and high-speed optical signals at 1064 nm was not available. One concern for this link is the mismatch between the two optical paths in differential mode. This can degrade the common-mode noise cancellation.



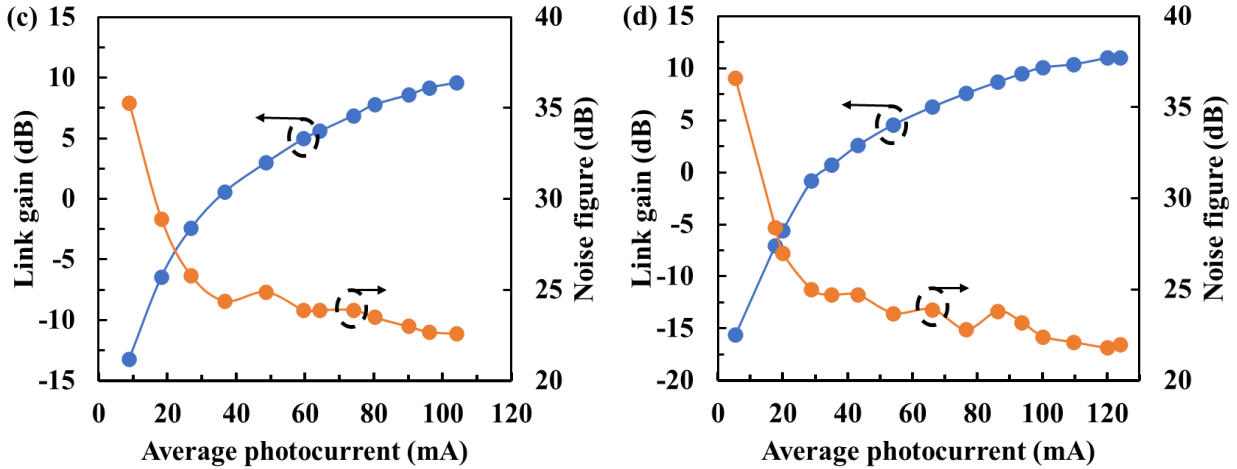


Figure 6-11. Noise figure and gain versus total photocurrent for balanced links using photodiodes with: (a) 10 μm -, (b) 14 μm -, (c) 16 μm - and (d) 18 μm -diameters.

The links using balanced photodiodes with 10 μm -, 14 μm -, 16 μm - and 18 μm -diameters were characterized at their 3 dB bandwidth point as shown in Figure. 6-11. For the link using 10 μm -diameter devices as shown in Figure. 6-11 (a), the link gain increases with the increasing photocurrent, and then saturates due to the space charge effect. The noise figure decreases as the photocurrent increases from 10 mA to 50 mA. For photocurrent greater than 50 mA, the noise figure is relatively constant owing to the increase of output noise. When the bias voltage is -7 V, the link gain is 6.8 dB and the noise figure is 25.8 dB at 38 GHz and 72 mA. The links utilizing 14 μm -, 16 μm - and 18 μm -diameter balanced photodiodes exhibit link gain of 9.2 dB, 9.6 dB and 11 dB and noise figure of 22.6 dB, 22.4 dB and 21.8 dB at 29 GHz, 27 GHz and 24.5 GHz, respectively.

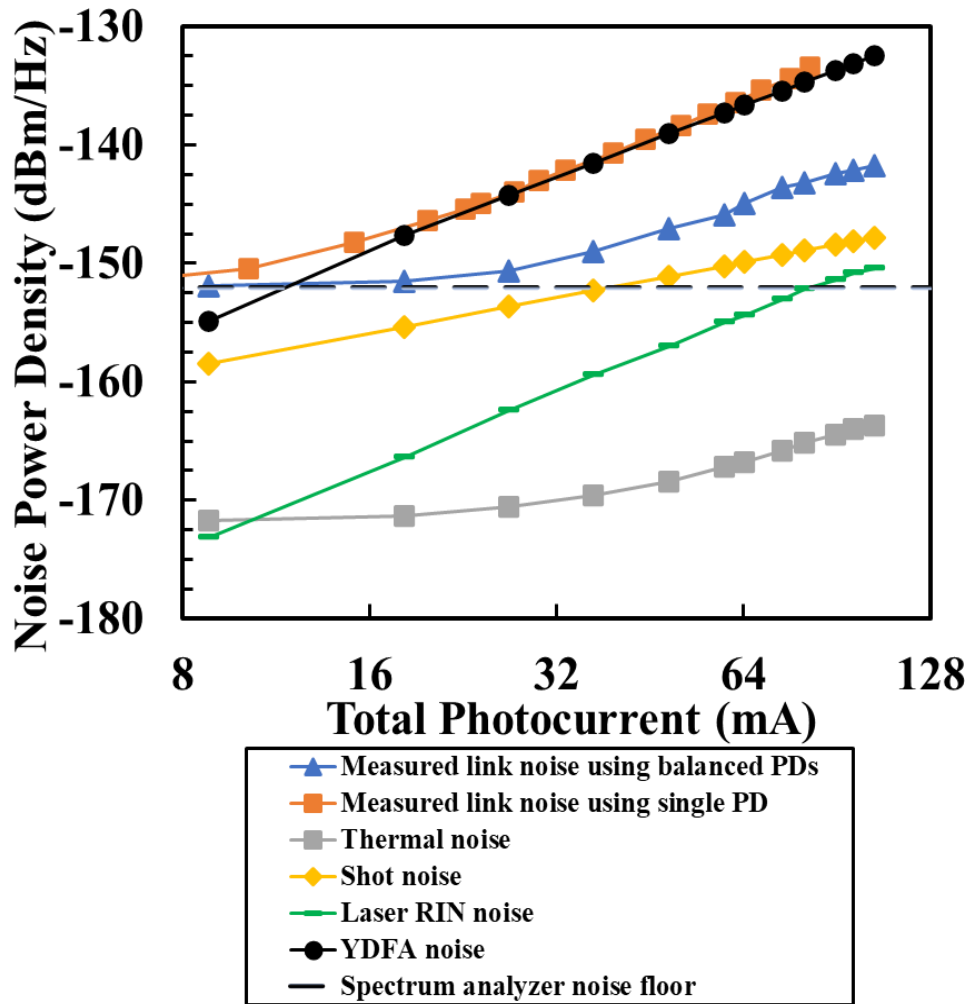


Figure 6-12. Calculated thermal noise, shot noise and laser noise powers and measured noise power spectral density at different photocurrents at 24 GHz.

Figure 6-12 shows the power spectral density of the calculated thermal noise, shot noise, laser noise, YDFA noise [2], and the measured noise. The thermal noise in the link includes the photodiode thermal noise and amplified thermal noise. The amplifier thermal noise gradually begins to dominate at high photocurrent due to high RF gain. The total thermal noise is approximately 13 dB lower than the spectrum analyzer noise floor at 100 mA. The RIN of our laser is less than -160 dBc/Hz at frequencies beyond 100 MHz and the calculated noise is much lower than the YDFA ASE noise. In addition, the value and increasing rate of shot noise are both

lower than the ASE noise. Since most of the spontaneous-spontaneous beat noise was filtered, we believe that the signal-spontaneous ASE beat noise from the YDFA dominates the link noise. It can be verified that the measured noise for the link using discrete photodiodes is close to the calculated ASE noise. It should be noted that noise for the balanced link is lower than for the link using a discrete photodiode. This is because part of common mode noise is cancelled by the balanced detection. However, the noise is not totally suppressed despite the high CMRR for the balanced photodiode due to the differences in the optical paths in the link setup.

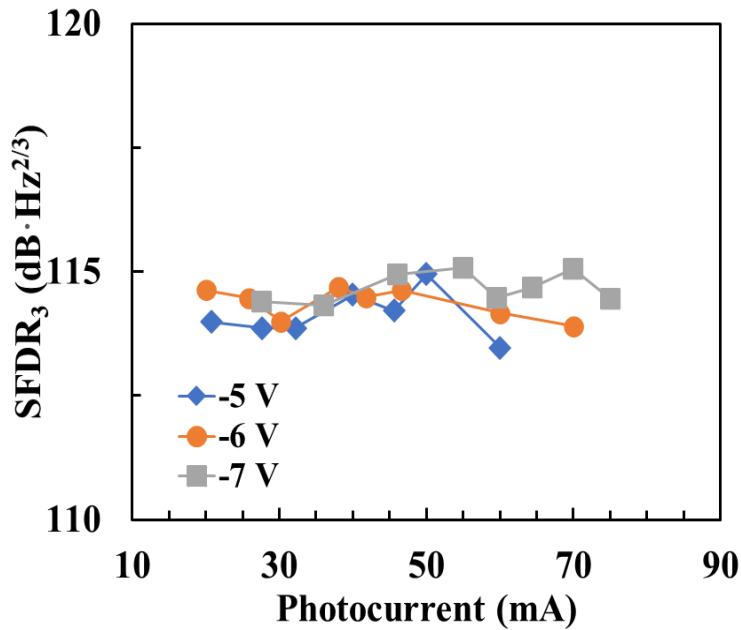


Figure 6-13. The link SFDR at 38 GHz versus bias voltages and photocurrents.

To characterize the linearity of the balanced photonic link using 10 μm -diameter photodiodes, the OIP3 was measured at 38 GHz and SFDR₃ was calculated according to (6.5). SFDR₃ remains near 114 dB·Hz^{2/3} at -5 V, -6 V and -7 V as shown in Figure. 6-13. The SFDR₃ is relatively independent of photocurrent because the link noise is primarily limited by ASE noise. For a common-mode noise-limited link, the SFDR₃ only depends on the relative intensity noise value and $V\pi$ of the modulator as shown in [2].

6.5 Low-Biased Link Configurations

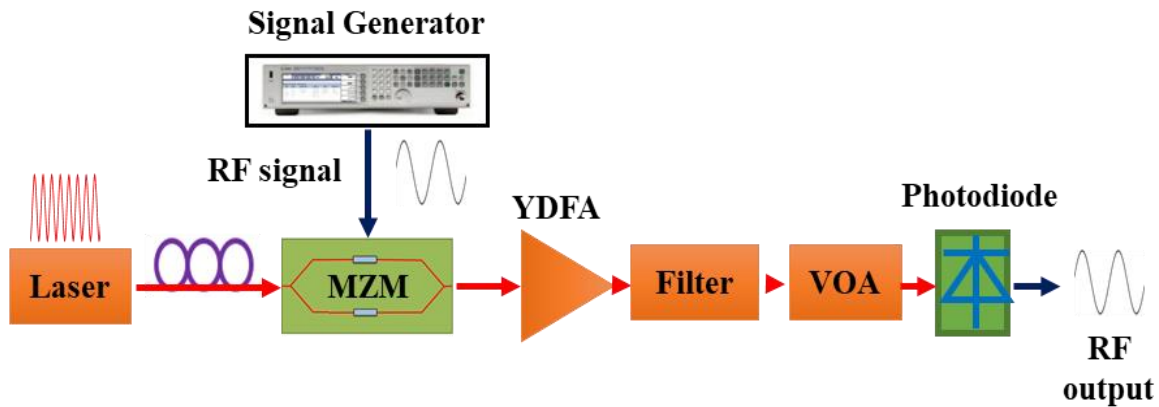


Figure 6-14. Experimental setup for low-bias photonic link.

An experimental setup for a low-bias analog photonic link is shown in Figure. 6-14. A high-power laser working at 1064 nm was used as the source. The RF signal was created by the MZM, which was biased at a low-bias point. The low-bias modulation technique improves the SNR at the cost of low output optical power after the MZM. A YDFA with maximum output power of 30 dBm was used to compensate the optical loss from the modulator. The excess noise of the YDFA was reduced with narrow bandwidth optical. Following the YDFA, an optical attenuator controlled the optical power input to the photodiode. The output noise power spectral density was measured with a spectrum analyzer.

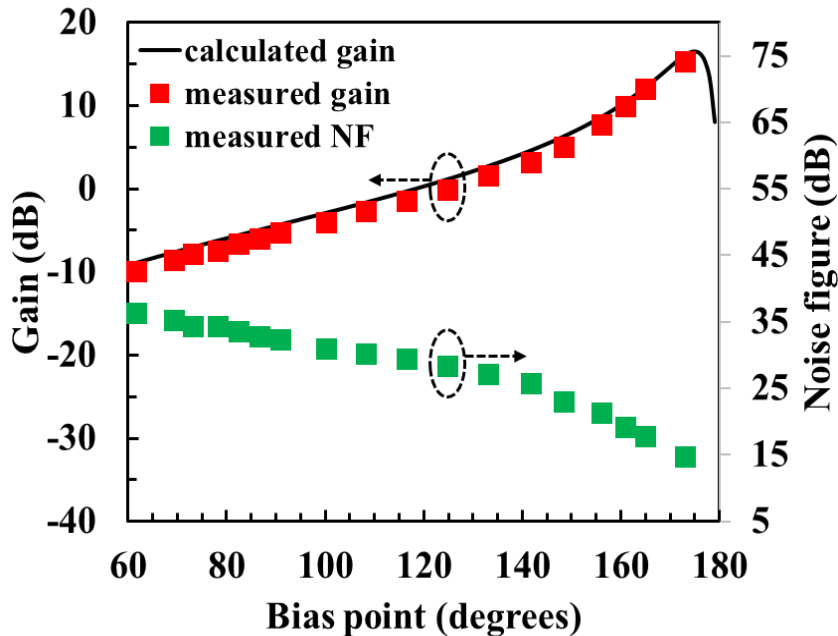


Figure 6-15. Gain and noise figure at 25 GHz and 20 mA photocurrent versus bias point.

In order to demonstrate the gain improvement that can be achieved using the low-bias scheme, the link gain and noise figure were measured at different bias points as shown in Figure. 6-15. The photocurrent and frequency of the input RF signal were fixed at 20 mA and 25 GHz, respectively. The ASE noise from the YDFA dominates under these conditions. From Figure. 6-15, the measured gain agrees well with the gain calculated using equation (6.1). The RF gain for the low-biased link is approximately 21 dB higher than that for the quadrature-biased link. The increased RF gain for the low-biased link is achieved at the cost of increased output noise power, owing to the decrease of optical input power into the YDFA according to (6.3). However, the RF gain increases faster than the noise, and the RF noise figure for the low-biased link is 17 dB lower than that for quadrature-biased link. When the bias point moves closer to the null point, the link gain degrades quickly.

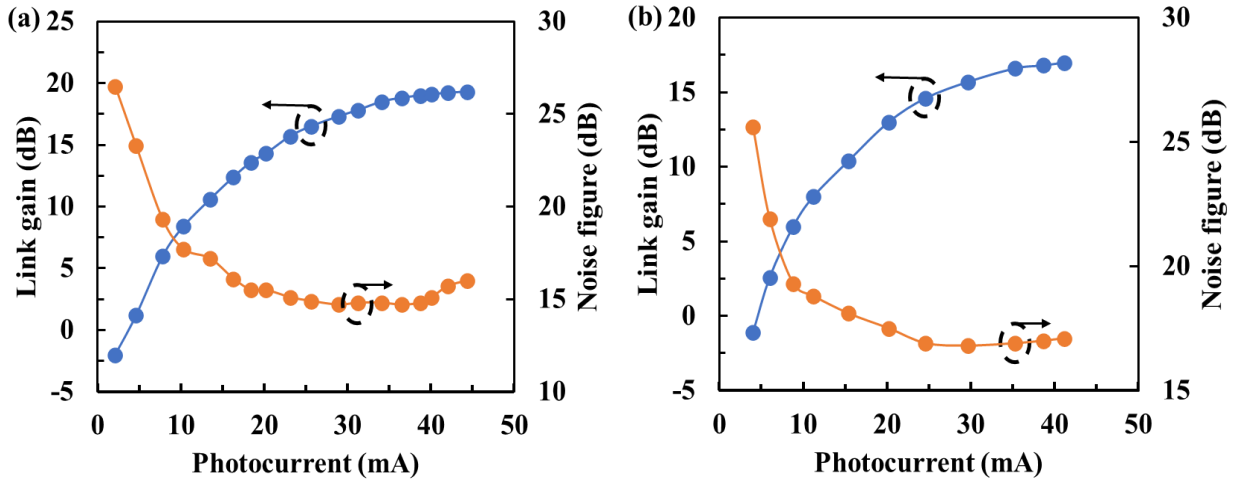


Figure 6-16. Noise figure and link gain versus photocurrents at: (a) 26 GHz and (b) 38 GHz.

The link performance was characterized at 26 GHz and 38 GHz by increasing the photocurrent. The modulator bias point was fixed at 172° to achieve the minimum input power for the YDFA as well as improved gain and noise figure. At 26 GHz and -8 V bias, the gain increases with increasing photocurrent and then saturates at ~ 40 mA. The low-biased link exhibits more RF power compression, and the gain begins to saturate at lower photocurrent [36]. This is attributed to the high modulation depth in the low-biased link. The link achieves gain of 19.3 dB and noise figure of 14.5 dB at 26 GHz. Lower gain is observed at 38 GHz. The lower gain at higher frequency is consistent with the photodiode characteristics. When the bias voltage is -8 V, the noise figure is 17 dB and the gain is 17 dB at 38 GHz.

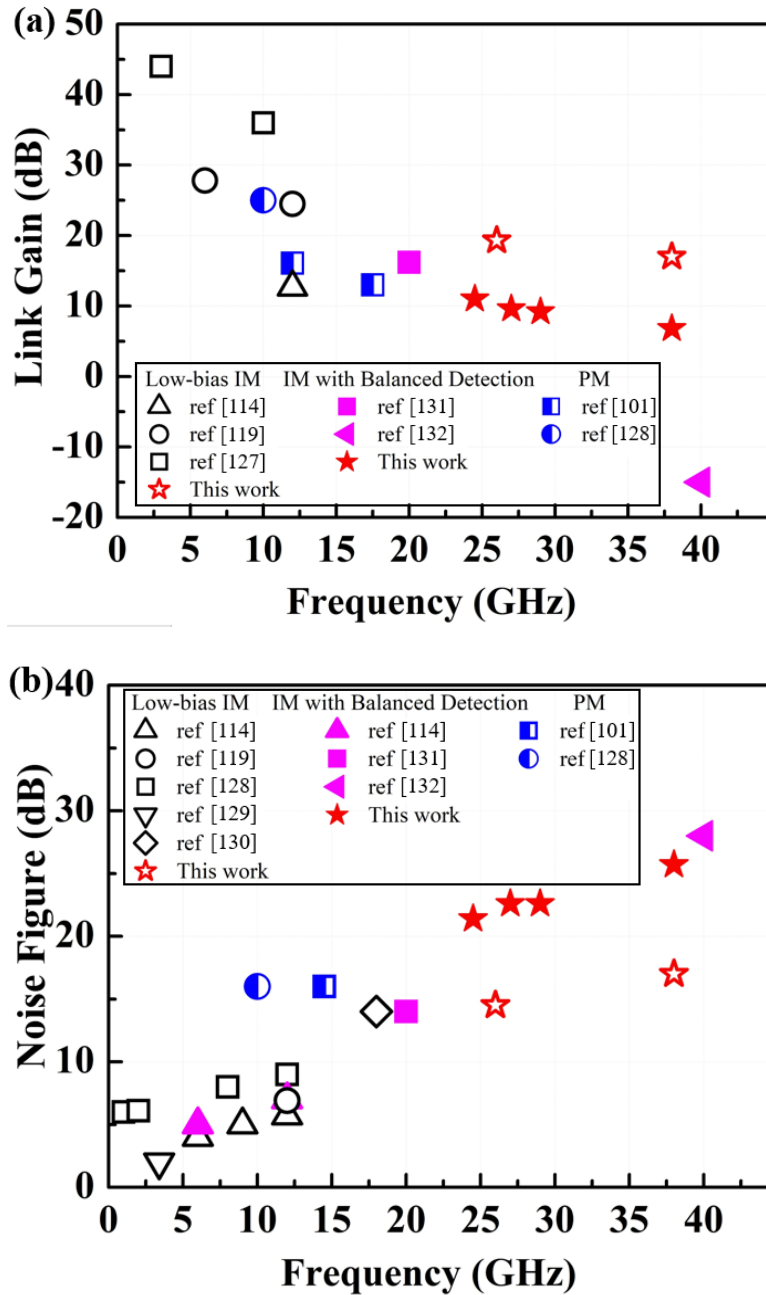


Figure 6-17. State-of-the-art (a) link gain and (b) noise figure as a function of frequency at 1550 nm and this work at 1064 nm. Hollow markers: low-biased intensity-modulated links; solid markers: quadrature-biased intensity-modulated links with balanced detection; half-filled markers: phase-modulated (PM) links. The links are amplifierless analog photonic links.

Figure. 6-17 summarizes gain and noise figure results for analog photonic links, including low-biased IM links [114, 119, 127-130], quadrature-biased IM links with balanced detection [114,

131, 132], and PM links [101, 128]. Our low-biased links achieve record-high link gain and low noise figure in the Ka frequency band. A distinct disadvantage of biasing the modulator away from quadrature is that it results in strong generation of second-order distortion, thereby limiting the operational bandwidth. Balanced detection can provide a higher dynamic range with slightly lower link gain and higher noise figure. Low-biased IM links are suitable for suboctave systems while the IM links with balanced detection can achieve wideband operation.

6.6 Conclusion

In this chapter, high-power balanced MUTC photodiodes and their performance in analog fiber photonic links have been demonstrated at 1064 nm. The RF output power and bandwidth of balanced photodiodes with diameters of 10 μm and 18 μm were 17.7 dBm at 38 GHz and 22 dBm at 24.5 GHz, respectively. These photodiodes also demonstrated high OIP3 of 34 dB and CMRR of 25 dB at 38 GHz. A quadrature-biased balanced link achieved gain of 6.8 dBm, noise figure of 25.8 dB and SFDR₃ of 114 dB·Hz^{2/3} at 38 GHz. Under low-bias modulation, the analog fiber photonic link achieved record 17 dB gain and 17 dB noise figure at 38 GHz.

Chapter 7 Conclusions and Future Work

7.1 Conclusions

The primary focus of my work has been to improve the performance of the CC-MUTC photodiodes and demonstrate their capabilities in analog photonic links. Photonic generation of high-power CW and pulsed RF signal is shown. Besides work at 1550 nm, the 1064 nm has been exploited as the promising operating wavelength for photonic links.

To mitigate heating issue at high power level, I have extended a flip-chip bonding technique using CVD diamond. The CC-MUTC photodiodes flip-chip bonded on diamond submounts exhibited 22.3 dBm output power at 50 GHz and 24.3 dBm output power at 41 GHz. These devices achieved record high RF output in frequency range from 30 GHz to 50 GHz. Compared with previously reported “champion” results, the devices on diamond submounts achieved ~57% higher RF output power and ~36 % higher failure power.

For pulsed illumination, the photodiodes were designed and demonstrated with a high avalanche breakdown voltage as well as suppressed space charge effect. The pulse photoresponse without RF modulation of these photodiodes achieved peak voltage of 38.3 V and full width at half maximum of 30 ps. The peak powers levels for gated modulation were 44.2 dBm (26.3 W), 41.6 dBm (14.5 W) and 40.6 dBm (11.5 W) at 10, 17 and 22 GHz, respectively. These powers are the highest among literature.

Two groups of back-illuminated high-speed, high-power and high-linearity photodiodes were designed and investigated at 1064 nm. The photodiodes in the 1st group exhibited relatively low responsivity of 0.46 A/W and low dark current of 1 nA at -8 V. The photodiodes with diameters of 15 μm , 18 μm , 20 μm and 24 μm from achieved 3 dB bandwidths of 55, 41, 32 and 27 GHz with

saturation RF power of 18.6, 19.4, 23.4 and 24.4 dBm, respectively. Analysis using a simple equivalent circuit model based on extracted parameters from S_{11} fitting data suggests that the bandwidths of the photodiodes are limited by the RC component with diameter $> 15 \mu\text{m}$. Based on the analysis of the 1st device group, the redesigned 2nd group showed a higher responsivity of 0.63 A/W and improved bandwidth. The 2nd group photodiode exhibited a record high bandwidth efficiency product of 41 GHz at 1064 nm. The device with diameters from 10 μm to 20 μm achieved saturation power from 15 dBm to 21.7 dBm at frequency from 60 GHz to 39 GHz. The measured third-order output intercept point showed a high linearity of 33 dBm at 40 GHz. A circuit analysis based on Z-parameter extraction indicates that voltage-dependent and photocurrent-dependent capacitance components are two major nonlinear mechanisms.

The balanced photodiodes with diameters from 10 μm to 18 μm delivered saturation power from 17.7 dBm to 22 dBm at frequency from 38 GHz to 24.5 GHz. These photodiodes also demonstrated high OIP3 of 34 dB and CMRR of 25 dB at 38 GHz. These high-power photodiodes were used to demonstrate a high-gain, low-noise figure, and high-linearity analog photonic link at 1064 nm. Two configurations with different noise reduction techniques without electronic amplification in the Ka-band were demonstrated. A quadrature-biased balanced link achieved gain of 6.8 dB, noise figure of 25.8 dB and SFDR₃ of 114 dB·Hz^{2/3} at 38 GHz. The low-bias fiber photonic link achieved record 17 dB gain and 17 dB noise figure at 38 GHz.

7.2 Future Work

7.2.1 High-Power RF Signals Generation

Chapter 4 demonstrates the optical generation of high-power pulsed RF signals. The peak power of the entire system is primarily limited by the performance of photodiodes. In order to

enhance the power handling capability of our photodetector, one approach is further optimization of the epitaxial layer design. Another promising method is to integrate a group of independent photodiode units and distribute the incident optical power to them. Previously, a parallel connection of multiple photodiodes to form an array has been deployed [133]. However, improvement in output power usually comes at the cost of reduced RC-limited bandwidth, since total photodiode capacitance scales linearly with the number of photodiodes. The traveling wave photodetector (TWPD) can be utilized to overcome this trade-off [134,135]. In a TWPD, the photodiode becomes a distributed device where the photocurrents from each photodiode along the transmission line add constructively.

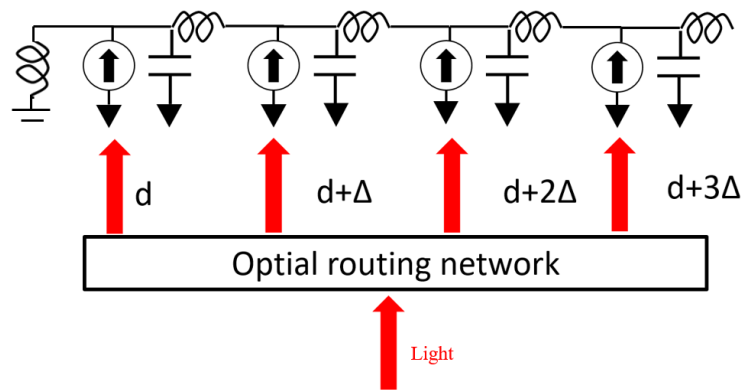


Figure 7-1. Schematic of TWPD.

Figure. 7-1 shows a schematic of the TWPD. The optical input signals are coupled into photodiodes through fiber array. The electrical signal propagation delay caused by the LC circuit and optical signal propagation delay in free space are carefully designed to match each other, so that the current from each photodiode adds constructively. The designed characteristic impedance, $Z \approx \sqrt{\frac{L}{C_j}}$, needs to match 50Ω in order to eliminate reflections. Through rough calculation, I have determined that the L should be ~ 630 pH and the free space delay is ~ 13 ps. The lumped elements are utilized here instead of CPW because it is hard to design such a large inductance to match with

the large photodiode capacitance.

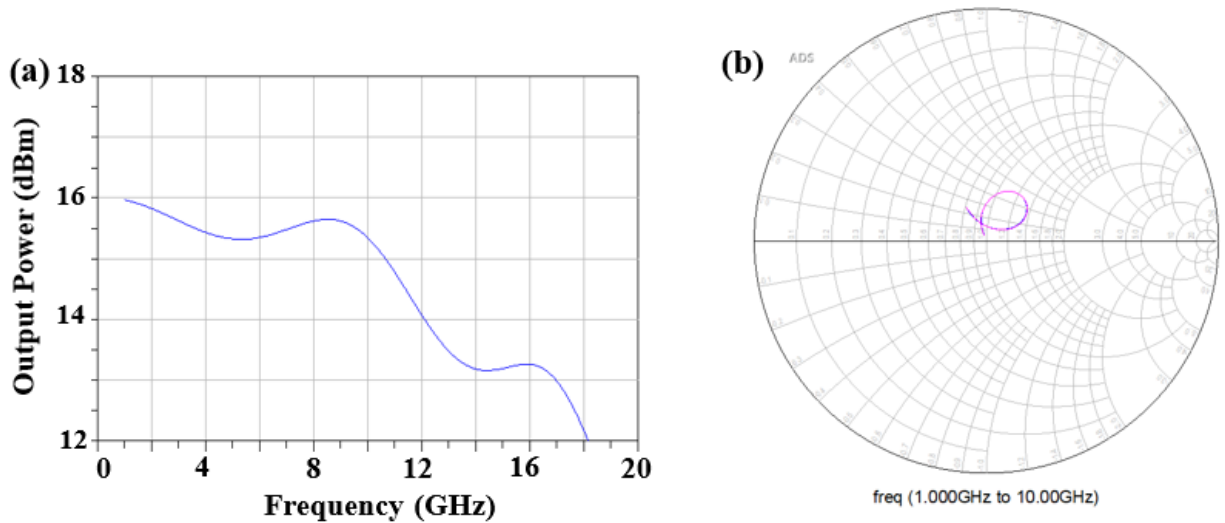


Figure 7-2. Simulated (a) bandwidth and (b) S₁₁.

The equivalent circuit model of the TWPD can be built in ADS. Figure. 7-2 (a) shows that a TWPD composed of 4 photodiodes with 50 μm -diameter can achieve 17 GHz bandwidth which is even higher than the bandwidth of a single photodiode. The electrical phase matches well with the optical phase. The S₁₁ at the terminal shows the impedance can be matched to 50 Ω using the calculated parameters.

An intrinsic issue for the TWPD is that a matching impedance should be placed at the input terminal of the photodiodes so as to eliminate the reflection of the back-propagating RF signals. A matching impedance would inevitably shunt half of the total photocurrent and consume considerable DC power. To solve this issue and further enhance output power, a distributed TWPD with an open input port formed by loading the photodiode array aperiodically is proposed. The circuit model is shown in Figure. 7-3 (a). The inductance, capacitance and resistance are different for each section. All the parameters can be optimized in ADS for a higher output power. By dedicated design, the current from each photodiode can be added constructively and impedance

matched to the load impedance. The inductance can be realized by a spiral inductor and capacitance can be realized by a metal-insulator-metal (MIM) capacitor. As shown in Figure. 7-3 (b), the aperiodic TWPD can achieve more than 10 dB higher output power than the single device.

It is promising to adopt a traveling-wave structure to improve the output power since several hundred watts peak power can be achieved with only a 4 photodiode array. If more devices can be integrated without sacrificing bandwidth, the photonic generated RF power could be comparable to that generated by conventional electronics. Finally, photonic links can be alternatives to all electrical cable systems. More design and further measurements are needed to verify this structure for high-power pulsed or CW signal generation.

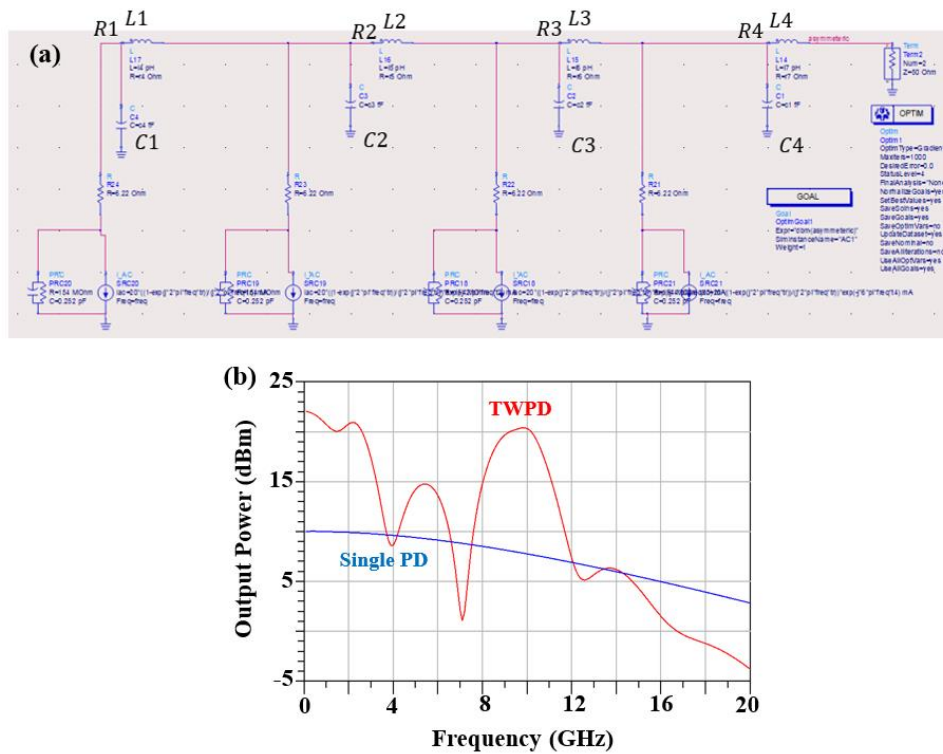


Figure 7-3. (a) Equivalent circuit model of aperiodic TWPD; (b) simulated RF output.

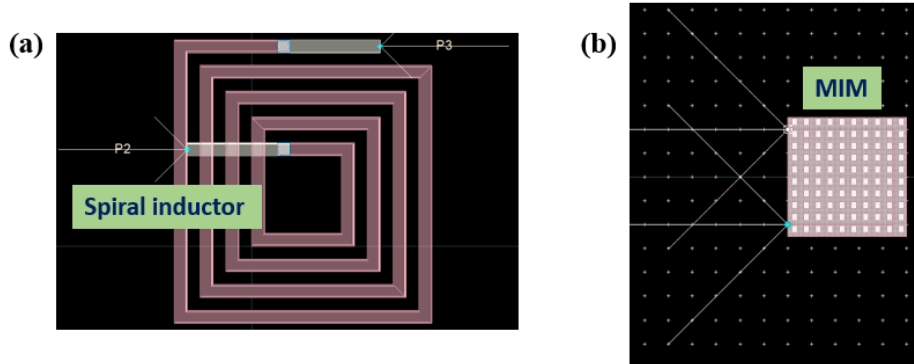


Figure 7-4. Layout of an (a) inductor and (b) capacitor.

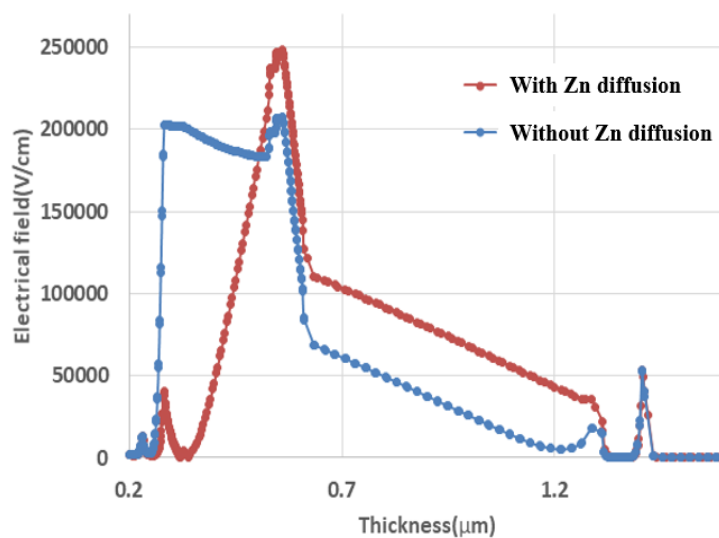


Figure 7-5. Electric field with and without Zn diffusion.

In addition, the performance of some of the photodiodes in this work is degraded by Zn diffusion as discussed in Chapter 3. Not only the linearity, but also the speed of device are limited by diffusion in the depleted absorber. As the simulated electric field in Crosslight shows, the space charge effect is more severe and the electric field is more likely to collapse in the absorber with Zn diffusion. If the Zn can be replaced by Beryllium for p-doping during material growth, the space charge effect can be mitigated and the frequency response can be enhanced. Therefore, the photodiode can be designed with a larger diameter and higher RF output power can be achieved.

7.2.2 Photonic Wireless Emitter

Recently, there has been increased interest in microwave photonic wireless emitters that tightly integrate a high-speed photodiode and an antenna [136, 137]. Based on the high-power pulsed signal generation described in the Chapter 4, further work can focus on incorporating an antenna to radiate high-power pulsed RF signals. In order to compensate for the attenuation of microwave radiation in the atmosphere, antennas with high directional gain are desired in order to direct the beam. Planar antennas are preferred for system miniaturization, planar integration, and wide bandwidth compared to bulky and incompatible commercial antennas [138]. In addition, a conjugate impedance match between the antenna and the photodiode needs to be achieved to reach maximum output power. The effect of impedance matching has recently been discussed in [139] and has been shown to have a significant effect on the radiation power.

The meander dipole antenna has the advantages of simple structure, compact footprint and planar profile, all of which are suitable for integration into large-scale phased arrays [140]. As shown in Figure, 7-6, using the commercial software ANSYS HFSS, the simulated impedance is 474Ω and gain is 2 dBi at 10 GHz. The footprint of the antenna is only $0.46 \text{ mm} \times 4.5 \text{ mm}$.

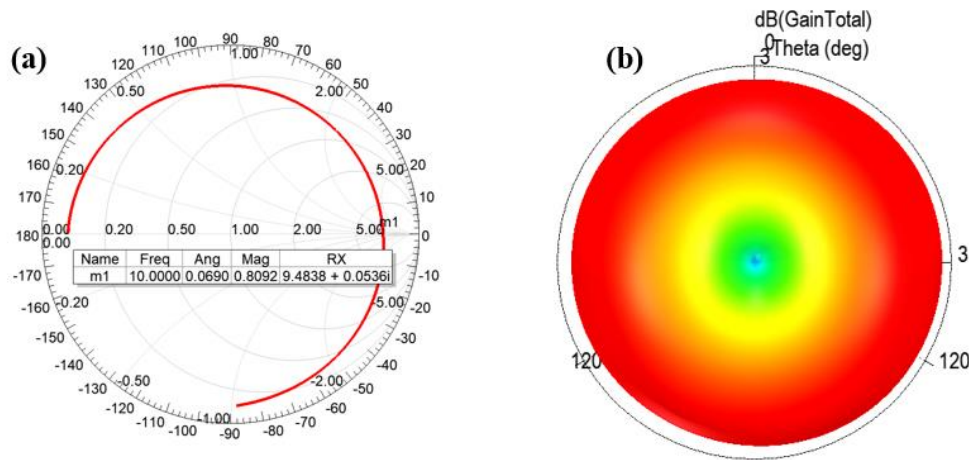


Figure 7-6. Simulated (a) S parameter and (b) gain of antenna.

The measured impedance for a 50- μm photodiode at 10 GHz is $5.1 \Omega - 43.15 j$. Since the photodiodes have capacitive impedances, an antenna with matching network should have an inductive input impedance to achieve conjugate matching. As shown in Figure. 7-7, a short stub resonant circuit can be adopted to realize an impedance-matching network. Specifically, the series inductor is realized by a high impedance transmission line and is series connected to the CPW center pad. The shunt capacitor can be accomplished using an MIM structure.

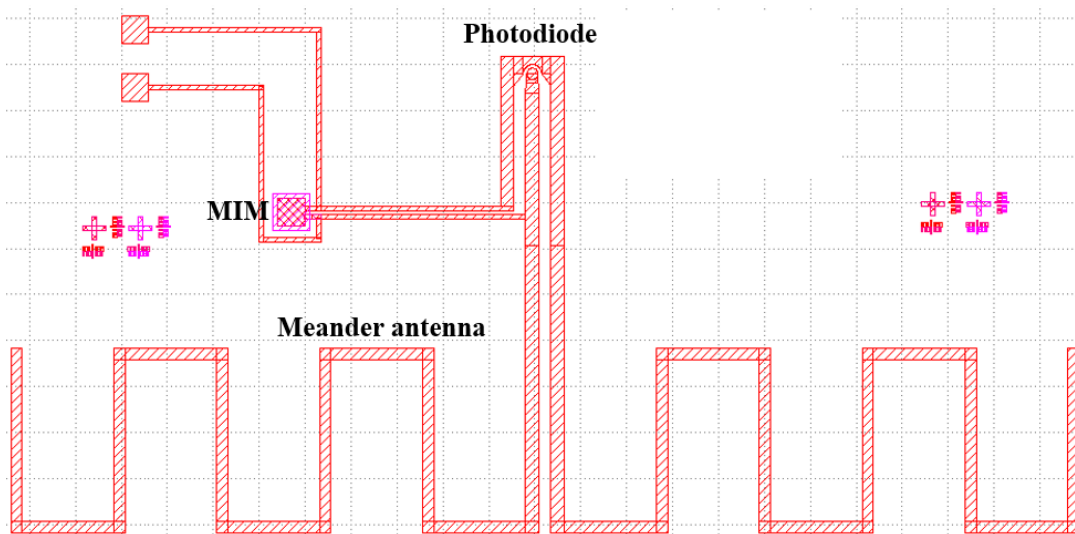


Figure 7-7. Layout of photonic wireless emitter.

One issue is that the planar antenna has a distorted radiation pattern due to the substrate on which it is placed as shown in [141]. Therefore, in the simulation it is necessary to place a superstrate on top of the antenna, which equalizes the electromagnetic wave propagation velocity on both sides for distortion suppression.

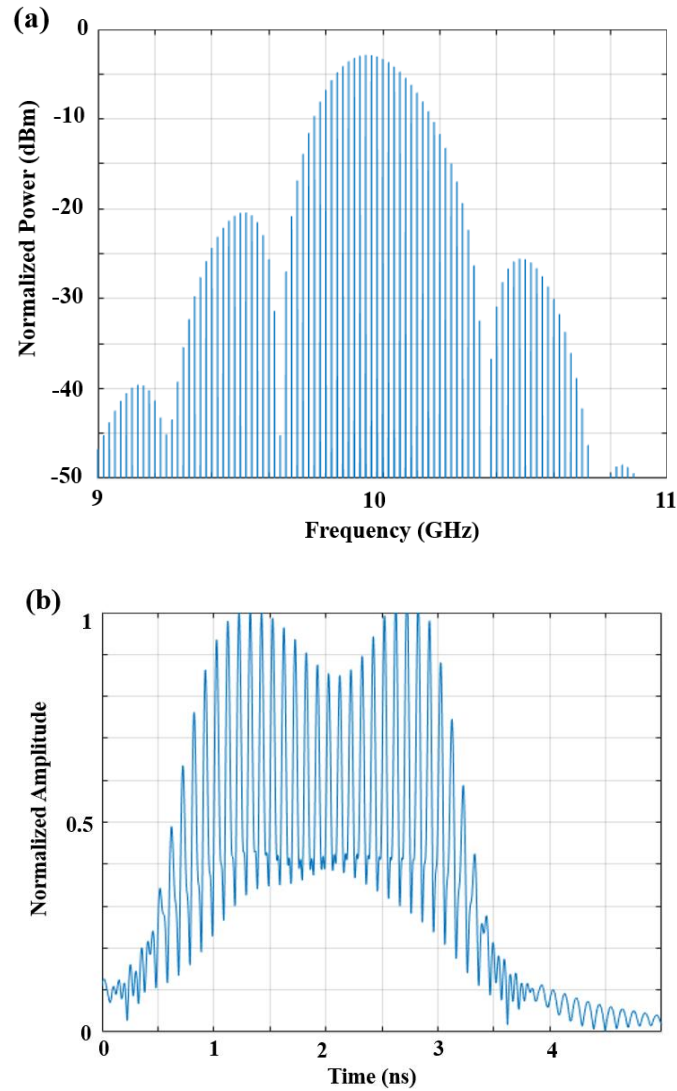


Figure 7-8. Normalized output signal in (a) frequency domain and (b) time domain.

Using the method shown in Chapter 4, the simulated output in Matlab with 10 GHz RF carrier signals is shown in Figure 7-8, when the repetition rate is fixed at 20 MHz and the duty cycle is 5 %. It can be observed that the pulse response and waveform are distorted due to the limited bandwidth of antenna and matching network. The peak power can be obtained based on the peak voltage read from an oscilloscope. The estimated peak effective isotropic radiated power (EIRP) for a single photonic emitter can reach up to 46.2 dBm, which significantly exceeds all reported results.

Based on that, the phased array can also be designed for radiation angle steering and high gain. Figure. 7-9 shows the simulated gain for 1×4 phased array. The radiation is more confined, and 11 dBi gain can be achieved. This work can demonstrate the performance of the pulsed photonic emitter for radar-type applications.

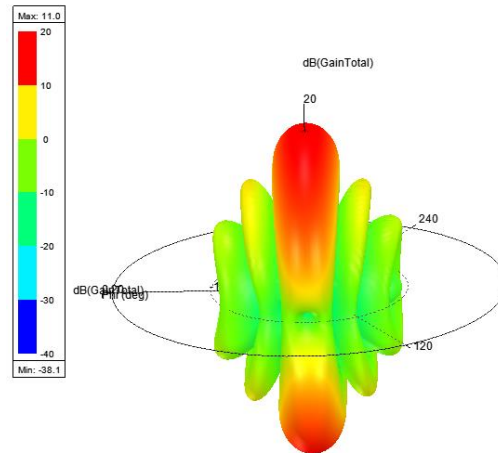


Figure 7-9. Simulated gain of phased array.

7.2.3 Phase Modulated Photonic Links

In Chapter 6, I have demonstrated high-performance an IM/DD link. Recently, there has been an increasing interest in phase modulated photonic links with interferometric detection. Phase modulated links are more efficient and are less susceptible to fiber nonlinearity compared to intensity modulated links [142, 143]. In addition, these links inherently can achieve a larger RF gain and lower noise figure compared to the conventional IM/DD link [2]. Another advantage is the fact that the phase modulator does not require a bias control circuit at the transmitter side. These make the phase modulated link a promising candidate for biosensors, 5G advanced optical communication and remoting systems [144, 145].

Our photodiodes, as shown in Chapter 5, achieved excellent power and linearity performance

and balanced photodiodes demonstrated high CMRR at high frequency at 1064 nm. They are suitable for phase modulated photonic links application.

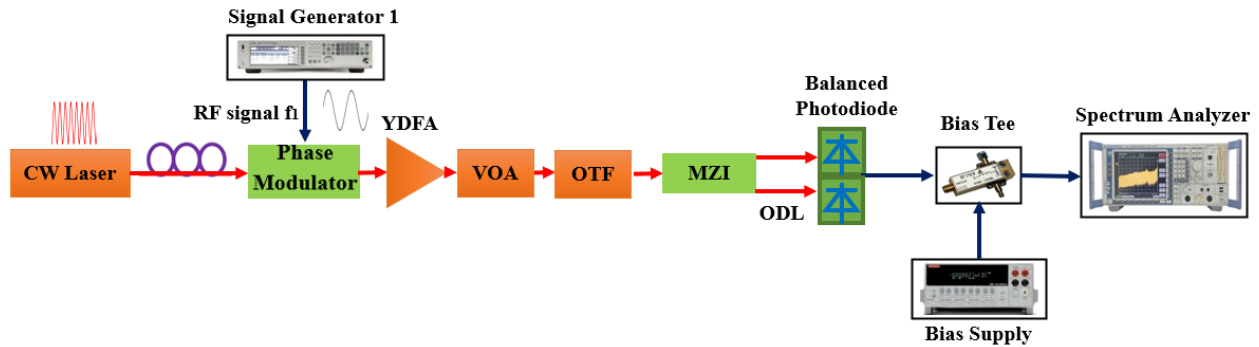


Figure 7-10. Experimental setup of phase modulated links with quadrature biased MZI and balanced photodiodes.

Figure. 7-10 shows the experimental setups for the phase modulated analog photonic links with high-power balanced photodiodes. A low-noise fiber laser at 1064 nm is followed by a polarization controller and a phase modulator. The output of the phase modulator is injected into a YDFA, followed by a variable optical attenuator, an optical tunable filter and a Mach–Zehnder interferometer (MZI). An optical delay line is used to match the phase of the two paths. Then the optical signal is down converted to the RF domain by photodetectors followed by an electrical spectrum analyzer.

In theory, the link gain of phase modulated links can be improved by 6 dB compared to an IM/DD link [2]. In addition, the noise figure can be reduced because it relates to the gain. Therefore, if my photodiodes are used in phase modulated links, the highest gain and lowest noise figure are projected.

References

- [1]. J. P. Yao, "Microwave photonics," *J. Lightw. Technol.*, vol. 27, no. 3, pp. 314–335, Feb. 2009.
- [2]. V. J. Urick, J. D. McKinney and K. J. Williams, "Fundamentals of Microwave Photonics," Wiley Series in Microwave and optical engineering, first edition, published in 2015.
- [3]. W. A. Gambling, "The rise and rise of optical fibers," *IEEE J Sel Top Quantum Electron*, vol. 6, no. 6, pp. 1084-1096, 2000.
- [4]. C. DeCusatis, ed. Handbook of fiber optic data communication: a practical guide to optical networking. Academic Press, 2013.
- [5]. E. Sisinni, et al. "Industrial internet of things: Challenges, opportunities, and directions." *IEEE Trans Industr Inform*, vol. 14, no. 11, pp. 4724-4734, 2018.
- [6]. A. S. Cacciapuoti, "Mobility-Aware User Association for 5G mmWave Networks." *IEEE Access*, Vol. 5, pp. 21497-21507, Sep. 2017.
- [7]. M. Kohler, et al., "Considerations for Future Automotive Radar in the Frequency Range Above 100 GHz." *German Microwave Conference Digest of Papers*, pp. 284-287, Mar. 2010.
- [8]. Sasan Bakhtiari, et al., "Compact Millimeter-Wave sensor for Remote Monitoring of Vital Signs." *IEEE Trans Instrum Meas*, vol. 61, no. 3, Mar. 2012.
- [9]. H. Darabi, et al. "A 2.4-GHz CMOS transceiver for Bluetooth." *IEEE Journal of Solid-State Circuits*, vol. 36, no. 12, pp. 2016-2024, 2001.
- [10]. IEEE 802 LAN/MAN Committee, IEEE Standard for Information Technology—Telecommunications and Information Exchange Between Systems—Local and Metropolitan Area Networks—Specific Requirements. Part 15.3: Wireless Medium Access Control (MAC) and Physical Layer (PHY) Specifications for High Rate Wireless Personal Area Networks (WPANs) Amendment 2: Millimeter-wave-based Alternative Physical Layer Extension, *IEEE Standard 802.15.3c*, IEEE Inc., New York (2009).
- [11]. G. R. Maccartney, et al. "Indoor office wideband millimeter-wave propagation measurements and channel models at 28 and 73 GHz for ultra-dense 5G wireless networks." *IEEE access*, vol. 3, pp. 2388-2424, 2015.
- [12]. S. Shakib, et al. "2.7 A wideband 28GHz power amplifier supporting 8× 100MHz carrier aggregation for 5G in 40nm CMOS." *2017 IEEE International Solid-State Circuits Conference (ISSCC)*. IEEE, 2017.
- [13]. T. J. Jackson, and T. J. Schmutge. "Passive microwave remote sensing system for soil moisture: Some supporting research." *IEEE Trans Geosci Remote Sens*, vol. 27, no. 2, pp. 225-235, 1989.
- [14]. I. H Woodhouse, Introduction to microwave remote sensing. CRC press, 2017.
- [15]. Wikipedia. Available at https://en.wikipedia.org/wiki/Remote_sensing.
- [16]. E. Alekseev, and D. Pavlidis. "GaN Gunn diodes for THz signal generation." *Microwave Symposium Digest. 2000 IEEE MTT-S International*. Vol. 3. IEEE, 2000.

- [17]. P. Mukherjee, and B. Gupta. "Terahertz (THz) frequency sources and antennas-A brief review." *International Journal of Infrared and Millimeter Waves*, vol. 29.no. 12, pp. 1091-1102, 2008.
- [18]. G. Gallerano, and S. Biedron. "Overview of terahertz radiation sources." *Proceedings of the 2004 FEL Conference*. no. 1. 2004.
- [19]. J. A. Nanzer, P. T. Callahan, M. L. Dennis and T. R. Clark Jr., "Photonic Signal Generation for Millimeter-Wave Communcatons." *John Hopkins APL Technical Digest*, Vol. 30, No.4, 2012.
- [20]. A. Seeds, et al., "Microwave Photonics: Present Status and Future Outlook." *International Topiocal Meeting on Microwave Photonics*, pp. 1-6, Oct. 2015.
- [21]. Z. Deng, and J. Yao. "Photonic generation of microwave signal using a rational harmonic mode-locked fiber ring laser." *IEEE Trans Microw Theory Tech*, vol. 54, no. 2, pp. 763-767, 2006.
- [22]. X. Chen, Z. Deng, and J. Yao. "Photonic generation of microwave signal using a dual-wavelength single-longitudinal-mode fiber ring laser." *IEEE Trans Microw Theory Tech*, vol. 54, no. 2, pp. 804-809, 2006.
- [23]. G. J. Simonis and K. G. Purchase, "Optical generation, distribution, and control of microwaves using laser heterodyne," *IEEE Trans. Microw. Theory Tech.*, vol. 38,no. 5, pp. 667-669, 1990.
- [24]. G. Qi, J. Yao, J. Seregelyi, S. Paquet, and C. Belisle, "Optical generation and distribution of continuously tunable millimeter-wave signals using an optical phase modulator," *J. Lightw. Technol.*, vol. 23, no. 9, pp. 2687- 2695, 2005.
- [25]. T. Fortier, F. Quinlan, A. Hati, C. Nelson, J. Taylor, Y. Fu, J. Campbell, and S. Diddams, "Photonic microwave generation with high-power photodiodes," *Opt. Lett.*, vol. 38, no. 10, pp. 1712-1714, 2013.
- [26]. M. I. Skolnik, "Radar handbook." (1970).
- [27]. E. Jacobset al. Considerations for application of RF-over-fiber to navy systems. *in Avionics, Fiber-Optics and Photonics Technology Conference, 2007 IEEE*.
- [28]. H. Chi, and Jianping Yao. "An approach to photonic generation of high-frequency phase-coded RF pulses." *IEEE Photon. Technol. Lett.* vol. 19. no. 10, pp. 768-770, 2007.
- [29]. P. Ghelfi, et al., A fully photonics-based coherent radar system. *Nature*, vol. 507, no.7492, p. 341-5, 2014.
- [30]. P. Ghelfi, F. Scotti, F. Laghezza, and A. Bogoni, "Photonic generation of phase-modulated RF signals for pulse compression techniques in coherent radars," *J. Lightw. Technol*, vol. 30, no. 11, pp. 1638-1644, 2012.
- [31]. J. D. McKinney, D. E. Leaird, and A. M. Weiner, "Millimeter-wave arbitrary waveform generation with a direct space-to-time pulse shaper," *Opt. Lett.*, vol. 27, no. 15, pp. 1345-1347, Aug. 2002.
- [32]. A. Dezfooliyan, and A. M. Weiner. "Photonic synthesis of high fidelity microwave arbitrary waveforms using near field frequency to time mapping." *Opt. Express*, vol. 21, no. 19, pp. 22974-22987, 2013.
- [33]. J. Hecht. *Understanding fiber optics*, 2015.

- [34]. J. Yao, "Microwave photonics," *J. Lightw. Technol.*, vol. 27, no. 3, pp. 314-335, 2009.
- [35]. A. J. Seeds, and K. J. Williams, "Microwave photonics," *J. Lightw. Technol.*, vol. 24, no. 12, pp. 4628-4641, 2006.
- [36]. V. J. Urick, et al., "Long-Haul Analog Photonics". *J. Lightw. Technol.* vol. 29, no. 8, pp. 1182-1205, 2011.
- [37]. Y. Jiang, S. Fang, Z. Bi, X. Xu, and L. Ma. "Nd: YAG lasers at 1064 nm with 1-Hz linewidth," *Appl. Phys. B*, vol. 98, no. 1, pp. 61-67, 2010
- [38]. K. Numata, M. Alalusi, L. Stolpner, G. Margaritis, J. Camp, and M. Krainak, "Characteristics of the single-longitudinal-mode planar-waveguide external cavity diode laser at 1064 nm," *Opt. Lett.*, vol. 39, no. 7, pp. 2101-2104, 2014.
- [39]. R. Paschotta, J. Nilsson, A. C. Tropper, and D. C. Hanna, "Ytterbium Doped Fiber Amplifiers," *IEEE J. Quantum Electron*, vol. 33, no. 7, pp. 1049-1056, July 1997.
- [40]. H. Xiao, P. Zhou, X. Wang, S. Guo, and X. Xu, "Experimental investigation on 1018-nm high-power ytterbium-doped fiber amplifier," *IEEE Photon. Technol. Lett*, vol. 24, no. 13, pp. 1088-1090, 2012.
- [41]. V. J. Urick, F. Bucholtz and K. J. Williams, "Noise penalty of highly saturated erbium-doped fiber amplifiers in analog links," *IEEE Photon. Technol. Lett*, vol. 18, no. 6, pp. 749-751, 2006.
- [42]. D. Marpaung, et al. "A photonic chip based frequency discriminator for a high performance microwave photonic link." *Opt. express*, vol. 18, no. 26, pp. 27359-27370, 2010.
- [43]. A. Karim and J. Devenport, "Noise figure reduction in externally modulated analog fiber optic links," *IEEE Photon. Technol. Lett*, vol. 19, no. 5, pp. 312-314, 2007.
- [44]. C. Middleton, and R. DeSalvo, "Improved microwave photonic link performance through optical carrier suppression and balanced coherent heterodyne detection," in *Enabling Photonics Technologies for Defense, Security, and Aerospace Applications VI*, vol. 7700, pp. 770008, 2010.
- [45]. G. P. Agrawal, "Fiber optic communication systems," vol. 222, John Wiley & Sons, 2012.
- [46]. D. Yu and H. Tan, "Engineering optics," Mechanical Industry Press, 314-316, 2006.
- [47]. H. K. Raut, V. A. Ganesh, A. S. Nair and S. Ramakrishna, "Anti reflective coatings: A critical, in depth review," *Energy & Environmental Science*, vol. 4, no. 10, pp. 3779-3804, 2011.
- [48]. J. Y. Kim, Y. K. Han, E. R. Kim and K. S. Suh, "Two layer hybrid anti reflection film prepared on the plastic substrates," *Current Applied Physics*, vol. 2, no. 2, pp. 123-127, 2002.
- [49]. K. Kato, S. Hata, K. Kawano, and A. Kozen, "Design of ultrawide-band, high-sensitivity p-i-n photodiodes," *IEICE Transactions on Electronics*, vol. E76-C, pp. 214-221, 1993.
- [50]. K. Kato, "Ultrawide-Band/High-Frequency Photodetectors," *IEEE Trans Microw Theory Techs*, vol. 47, no. 7, pp. 1265-1281, July 1999.
- [51]. D. M. Pozar, *Microwave Engineering* third edition, Wiley-John Wiley & sons, TK7876.P69 2005.
- [52]. T. Ishibashi, et al. "High-speed response of uni-traveling-carrier photodiodes." *Japanese journal of applied physics*, vol. 36.10R, pp. 6263, 1997.

- [53]. V. Balynas, A. Krotkus, A. Stalnionis, A. T. Gorelionok, N. M. Schmidt, J. A. Tellefsen, *Appl. Phys. A*, vol. 51, no.4, pp.357-360, 1990..
- [54]. T. Ishibashi, et al., "Uni-traveling-carrier photodiodes," *Tech. Dig. Ultrafast Electronics Optoelectronics OSA Spring Topical Meeting*, pp.166-168, 1997.
- [55]. N. Li, et al., "High-saturation-current charge-compensated InGaAs/InP uni-travelling-carrier photodiode." *The 16th Annual Meeting of the IEEE, Lasers and Electro-Optics Society*, pp.790-791, Oct. 2003.
- [56]. D. H. Jun, J.H. Jang, Ilesanma Adeseda, J.I. Song, "Improved efficiency bandwidth product of Modified Uni-traveling Carrier Photodiode Structure using an undoped Photo-absorption Layer," *Japanese Journal of Applied Science*, vol. 45, no. 4B, pp. 3475-3478, 2006.
- [57]. N. Shimizu, N. Watanabe, T. Furuta and T. Ishibashi, "InP-InGaAs un-traveling-carrier photodiode with improved 3-dB bandwidth of over 150 GHz," *IEEE Photon. Technol. Lett.*, vol. 10, no. 3, pp. 412-414, 1998.
- [58]. N. Li, X. Li, S. Demiguel, X. Zheng, J.C. Campbell, D.A. Tulchinsky, K.J. Williams, T.D. Isshiki, G.S. Kinsey and R. Sudharsanan, "High saturation current charge-compensated InGaAs –InP uni-traveling-carrier photodiode," *IEEE Photo. Technol. Lett.*, vol. 16, no. 3, pp. 864-866, Mar. 2004.
- [59]. K.J. Williams, and R.D. Esman, Design considerations for high-current photodetectors. *J. Lightw. Technol*, vol. 17, no. 8, pp. 1443-1454. 1999.
- [60]. H. Ono, S. Taniguchi, and T. Suzuki. "High-frequency characteristics and saturation electron velocity of InAlAs/InGaAs metamorphic high electron mobility transistors at high temperatures." *16th IPRM. 2004 International Conference on Indium Phosphide and Related Materials, 2004*. IEEE, 2004.
- [61]. Huang, Jack Jia-Sheng, et al. "Temperature dependence study of mesa-type InGaAs/InAlAs avalanche photodiode characteristics." *Advances in OptoElectronics 2017*, 2017.
- [62]. Z. Li, et al., "High-saturation high-linearity flip-chip bonded modified uni-traveling carrier photodiode," *Opt. Express*, vol. 19, no. 26, pp. B385-B390, 2011.
- [63]. Q. Zhou, A.S. Cross, A. Beling, Y. Fu, Z. Lu, J. C. Campbell, "High Power V-Band InGaAs/InP Photodiodes," *IEEE Photon. Technol. Lett.*, vol. 25, no. 10, 2013.
- [64]. X. Xie, Q. Zhou, K. Li, Y. Shen, Q. Li, Z. Yang, A. Beling and J.C. Campbell, "Improved Power Conversion Efficiency in High Performance Photodiodes by flip chip on diamond," *Optica.*, vol.1, no.6, pp. 429-435, Dec. 2014.
- [65]. C. H. Cox, III, et al., "Limits on the performance of RF over fiber links and their impact on device design". *IEEE Trans Microw Theory Techs*, vol. 54, no. 2, pp. 906 920, 2006.
- [66]. K. J. Williams, R.D. Esman, and M. Dagenais, "Nonlinearities in p i n microwave photodetectors." *J. Lightw. Technol*, vol. 14, no. 1, pp. 84 96. 1996.
- [67]. D. A. Humphreys, and R.A. Lobbett, "Investigation of an optoelectronic nonlinear effect in a GaInAs photodiode, and its application of a coherent optical communication system." *Optoelectronics, IEE Proceedings J*, vol. 135, no. 1, pp. 45 51, 1988.

- [68]. M. Dentan, and B. de Cremoux, "Numerical simulation of the nonlinear response of a p i n photodiode under high illumination." *J. Lightw. Technol*, vol. 8, no. 8, pp. 1137-1144, 1990.
- [69]. K. J. Williams, and R.D. Esman, "Photodiode DC and microwave nonlinearity at high currents due to carrier recombination nonlinearities." *IEEE Photon. Technol. Lett.*, vol. 10, no. 7, pp. 1015-1017, 1998
- [70]. K. J. Williams, and P.G. Goetz. Photodiode compression due to current dependent capacitance. in *Microwave Photonics, 2000. MWP 2000. International Topical Meeting on. 2000.*
- [71]. T. H. Stievater, and K.J. Williams, "Thermally induced nonlinearities in high speed p i n photodetectors." *IEEE Photon. Technol. Lett*, vol. 16, no. 1, pp. 239-241, 2006.
- [72]. M. N. Draa, A. S. Hastings, and K. J. Williams, "Comparison of photodiode nonlinearity measurement systems," *Optics Express*, vol. 19, pp. 12635-12645, 2011.
- [73]. J. Shi, Y. Cheng, J. Wun, K. Chi, Y. Hsin, and S. D. Benjamin, "High-speed, high-efficiency, large-area p-i-n photodiode for application to optical interconnects from 0.85 to 1.55 μm wavelengths," *J. Lightw. Technol*, vol. 31, pp. 3956-3961, 2013.
- [74]. G. Wang, T. Tokumitsu, I. Hanawa, K. Sato, and M. Kobayashi, "Analysis of high speed p-i-n photodiode S-parameters by a novel small-signal equivalent circuit model," *IEEE Microwave and Wireless Components Letters*, vol. 12, pp. 378-380, 2002.
- [75]. W. A. Wohlmuth, et al. "InGaAs metal - semiconductor - metal photodetectors with engineered Schottky barrier heights." *Applied physics letters* , vol. 69, no. 23, pp. 3578-3580, 1996.
- [76]. F. G. Ivey, D. Wang, D. Yang, R. Bruce and G.Knight, "Au/Ge/Ni ohmic contacts to n-Type InP." *J. Electron. Mater.*, vol.23, Issue 5, pp. 441-446, May 1994.
- [77]. M. Frecassetti, "E-Band and V-Band-Survey on status of worldwide regulation." Jun 2015.
- [78]. R. Rony, E. Lopez-Aguilera, and Ed. Garcia-Villegas. "Cost Analysis of 5G Fronthaul Networks Through Functional Splits at the PHY Layer in a Capacity and Cost Limited Scenario." *IEEE Access* 9, pp. 8733-8750.
- [79]. T. Ishibashi, et al. "InP/InGaAs uni-traveling-carrier photodiodes." *IEICE transactions on electronics*, vol.83, no. 6, pp.938-949, 2000.
- [80]. J. Zang, et al. "High quantum efficiency uni-traveling-carrier photodiode." *IEEE Photon. Technol. Lett*, vol. 29, no. 3, pp.302-305, 2017.
- [81]. J. Li, B. Xiong, C. Sun, D. Miao, and Y. Luo, "Analysis of frequency response of high power MUTC photodiodes based on photocurrent-dependent equivalent circuit model." *Opt. Express*, vol. 23, no. 17, pp. 21615-21623, 2015.
- [82]. N. Shimizu, N. Watanabe, T. Furuta, and T. Ishibashi, "Improved response of uni-traveling-carrier photodiodes by carrier injection," *Jpn. J. Appl. Phys.*, vol. 37, no. 3, p. 1424, Mar. 1998.
- [83]. Y. Fu, et al. "Characterizing and modeling nonlinear intermodulation distortions in modified uni-traveling carrier photodiodes." *IEEE J. Quantum Electron.*, vol. 47, no. 10, pp.1312-1319, 2011.

- [84]. L. Goldberg, H. F. Taylor, J. F. Weller, and D. M. Bloom, "Microwave signal generation with injection locked laser diodes," *Electron Lett.*, vol. 19, no. 13, pp. 491–493, 1983.
- [85]. S. Zhu, X. Fan, M. Li, N. Zhu, and W. Li. "Photonic generation and transmission of phase-modulated microwave signals." *In Semiconductor Lasers and Applications IX, 11182(111820B)*, 2019.
- [86]. Y. Zhang and S. Pan, "Generation of phase-coded microwave signals using a polarization-modulator-based photonic microwave phase shifter," *Opt. Lett.*, vol. 38, no. 5, pp. 766–768, 2013.
- [87]. K. Saleh, J. Millo, B. Marechal, B. Dubois, A. Bakir, A. Didier, C. Lacroûte, and Y. Kersalé. "Photonic Generation of High Power, Ultrastable Microwave Signals by Vernier Effect in a Femtosecond Laser Frequency Comb." *Sci. Rep.*, vol. 8, no.1, pp. 1-11, 2018.
- [88]. X. Xie, K. Li, Y. Shen, Q. Li, J. Zang, A. Beling, and J. C. Campbell. "Photonic generation of high-power pulsed microwave signals." *J. Lightw. Technol.*, vol. 33, no.18, pp. 3808-3814, 2015.
- [89]. J. S. Ng, C. H. Tan, J. P. R. David, G. Hill, and G. J. Rees. "Field dependence of impact ionization coefficients in $\text{In}_{0.53}\text{Ga}_{0.47}\text{As}$." *IEEE Trans. Electron Devices* 50, pp. 901-905, no. 4, 2003.
- [90]. G. Meneghesso, A. Neviani, R. Parisotto, L. Vendrame, M. Hafizi, W. E. Stanchina, C. Canali, and E. Zanoni. "Measurement of the Electron Ionization Coefficient Temperature Dependence in InGaAs-based Heterojunction Bipolar Transistors." *In ESSDERC'96: Proceedings of the 26th European Solid State Device Research Conference*, pp. 447-450. IEEE, 1996.
- [91]. K. Taguchi, T. Torikai, Y. Sugimoto, K. Makita, and H. Ishihara. "Temperature dependence of impact ionization coefficients in InP." *J Appl Phys* 59, pp. 476-481, no. 2, 1986.
- [92]. H. T. J. Meier, "Design, characterization and simulation of avalanche photodiodes." PhD diss., ETH Zurich, 2011.
- [93]. Y. Shen, J. Gaskins, X. Xie, B. M. Foley, R. Cheaito, P. E. Hopkins, and J. C. Campbell. "Thermal analysis of high-power flip-chip-bonded photodiodes." *J. Lightw. Technol.*, vol. 35, no. 19, pp. 4242-4246, 2017.
- [94]. Y. Liao, G. Lin, H. Kuo, K. Feng, and M. Feng. "10-gb/s operation of an $\text{In}_{0.53}\text{Ga}_{0.47}\text{As}$ pin photodiode on metamorphic InGaP buffered semi-insulating GaAs substrate." *IEEE Photon. Technol. Lett.*, 18, pp. 1822-1824, no. 17, 2006.
- [95]. H. Ito, S. Kodama, Y. Muramoto, T. Furuta, T. Nagatsuma, and T. Ishibashi. "High-speed and high-output InPInGaAs untraveling-carrier photodiodes." *IEEE J. Sel. Topics Quantum Electron*, vol. 10, no. 4, pp. 709-727, 2004.
- [96]. J. Taylor, S. Datta, A. Hati, C. Nelson, F. Quinlan, A. Joshi, and S. Diddams, "Characterization of power-to-phase conversion in high-speed P-I-N photodiodes," *IEEE Photon. J.*, vol. 3, no. 1, pp. 140–151, 2011.
- [97]. Agilent Application Note 150-2, 2012.
- [98]. K. Sasahira, K. Kuroda, and Y. Yoshikuni, "Pulse amplification characteristics of a CW pumped erbium-doped fiber amplifier," in *Proc. Opto Electron. Commun. Conf.*, pp. 346–347 2010.
- [99]. K. Kuroda, K. Sasahira, and Y. Yoshikuni. "Gain saturation of a CW-pumped erbium-doped fiber

- amplifier for nanosecond pulses." *Opt. Fiber Technol.*, vol. 18, no. 1, pp. 44-46, 2012.
- [100]. M. Pysker, R. Bloomer, C. M. Kaleva, T. D. Roberts, P. Battle, and O. Pfister, "Broadband amplitude squeezing in a periodically poled KTiOPO4 waveguide," *Opt. Lett.*, vol. 34, no. 3, pp. 256–258, 2009.
- [101]. Z. Yang, Q. Yu, J. Zang, J. C. Campbell, and A. Beling, "Phase modulated analog photonic link with a high-power high-linearity photodiode," *J. Lightw. Technol.*, vol. 36, no. 18, pp. 3805–3814, Sep. 15, 2018.
- [102]. H. Jiang, and P. K. L. Yu. "Equivalent circuit analysis of harmonic distortions in photodiode." *IEEE Photon. Technol. Lett.*, vol. 10, no. 11, pp. 1608-1610, Oct. 1998.
- [103]. A. Beling, H. Pan, H. Chen, and J. C. Campbell. "Linearity of modified uni-traveling carrier photodiodes". *J. Lightw. Technol.*, vol. 26, no. 15, pp 2373-2378, Aug 2008.
- [104]. T. Ohno et al. "Measurement of intermodulation distortion in high-output-power uni-travelling-carrier refracting-facet photodiode at 40 GHz." *Electronics Letters*, 36.23, 1954-1955, 2000.
- [105]. J. Li, et al. "Analysis of frequency response of high power MUTC photodiodes based on photocurrent-dependent equivalent circuit model." *Opt. Express*, vol. 23, no. 17, pp. 21615-21623, 2015.
- [106]. R. Zhang, B. Hraimel, X. Li, P. Zhang and X. Zhang, "Design of broadband and high-output power uni-traveling-carrier photodiodes." *Opt. Express*, vol. 21, no. 6, pp 6943-6954, 2013.
- [107]. H. Pan, Z. Li, A. Beling, and J. C. Campbell, "Characterization of High-Linearity Modified Uni-Traveling Carrier Photodiodes Using Three-Tone and Bias Modulation Techniques," *J. Lightw. Technol.* vol. 28, pp. 1316-1322, 2010.
- [108]. L.-C. Wang and S. Rangapillai, "A survey on green 5G cellular networks," in *2012 International Conference on Signal Processing and Communications (SPCOM)*, 2012, pp. 1-5.
- [109]. D. C. Araújo, T. Maksymuk, A. L. de Almeida, T. Maciel, J. C. Mota, and M. Jo, "Massive MIMO: survey and future research topics," *Iet Communications*, vol. 10, no. 15, pp. 1938-1946, 2016
- [110]. T. V. Omotosho, J. S. Mandeep, and M. Abdullah, "Cloud cover, cloud liquid water and cloud attenuation at Ka and V bands over equatorial climate," *Meteorol. Appl.*, vol. 21, no. 3, pp. 777–785, 2014.
- [111]. G. Skofronick-Jackson et al., "The Global Precipitation Measurement (GPM) mission's scientific achievements and societal contributions: Reviewing four years of advanced rain and snow observations," *Quart. J. Roy. Meteorol. Soc.*, vol. 144, pp. 27–48, Nov. 2018.
- [112]. M. Alemohammad, D. Novak, and R. Waterhouse. "Ka-band RF photonic link with optimized performance." in *Proc. IEEE/MTT-S Microw. Symp.*, 2012, pp. 1-3.
- [113]. M. M. Sisto, S. LaRochelle, and L. A. Rusch, "Gain optimization by modulator-bias control in radio-over-fiber links," *J. Lightw. Technol.*, vol. 24, no. 12, pp. 4974–4982, Dec. 2006.
- [114]. E. I. Ackerman et al., "Signal-to-noise performance of two analog photonic links using different noise reduction techniques," in *Proc. IEEE/MTT-S Microw. Symp.*, 2007, pp. 51–54.
- [115]. Y. Cui et al., "Enhanced spurious-free dynamic range in intensitymodulated analog photonic link using digital postprocessing," *IEEE Photon. J.*, vol. 6, no. 2, pp. 1–8, Apr. 2014.
- [116]. A. Joshi, X. Wang, D. Mohr, D. Becker, and C. Wree, "Balanced photoreceivers for analog and digital

- fiber optic communications." *Proc. SPIE*, pp. 39-50, 2005.
- [117]. P. F. Driessen, T. E. Darcie, and J. Zhang. "Analysis of a class-B microwave-photonic link using optical frequency modulation." *J. Lightw. Technol.*, vol. 26, no. 15, pp. 2740-2747, 2008.
- [118]. E. I. Ackerman, G. Betts, W. K. Burns, J. C. Campbell, C. H. Cox, III, D. Ning et al., "Signal-to-noise performance of two analog photonic links using different noise reduction techniques," in *Proc. IEEE/MTT-S Microw. Symp.*, 2007, pp. 51–54.
- [119]. X. Xie, K. Li, Q. Zhou, A. Beling, and J. C. Campbell. "High-gain, low-noise-figure, and high-linearity analog photonic link based on a high-performance photodetector." *J. Lightw. Technol.*, vol.32, no. 21, pp. 4187-4192, 2014.
- [120]. Y. Cui, Y. Dai, F. Yin, J. Dai, K. Xu, J. Li, and J. Lin. "Intermodulation distortion suppression for intensity-modulated analog fiber-optic link incorporating optical carrier band processing." *Opt. Lett.*, vol. 21, no. 20, pp. 23433-23440, 2013.
- [121]. L. Huang, R. Li, D. Chen, P. Xiang, P. Wang, T. Pu, and X. Chen. "Photonic downconversion of RF signals with improved conversion efficiency and SFDR." *IEEE Photon. Technol. Lett.*, vol 28, no. 8, pp. 880-883, 2016.
- [122]. X. Xie, Y. T. Dai, K. Xu, J. Niu, R. X. Wang, L. Yan et al., "Digital joint compensation of IMD3 and XMD in broadband channelized RF photonic link," *Opt. Exp.*, vol. 20, no. 23, pp. 25636–25643, Nov. 2012
- [123]. Q. Zhou, A. S. Cross, Y. Fu, A. Beling, B. M. Foley, P. E. Hopkins, and J. C. Campbell. "Balanced InP/InGaAs photodiodes with 1.5-W output power." *IEEE Photonics J.* vol. 5, no. 3, pp. 6800307-6800307, 2013.
- [124]. Z. Li, H. Chen, H. Pan, A. Beling, and J. C. Campbell, "High-power integrated balanced photodetector," *IEEE Photon. Technol. Lett.*, vol. 21, no. 24, pp. 1858–1560, Dec. 2009.
- [125]. A. Beling, A. S. Cross, Q. Zhou, Y. Fu, and J. C. Campbell, "High-power flip-chip balanced photodetector with >40 GHz bandwidth," in *Proc. IEEE Photon. Conf., 2013*, pp. 352–353.
- [126]. V. Houtsma et al., "A 1 W linear high-power InP balanced uni-traveling carrier photodetector," in *Proc. 37th Eur. Conf. Exhib. Opt. Commun.*, 2011, pp. 1–3.
- [127]. V. J. Urick, M. S. Rogge, F. Bucholtz, and K. J. Williams. "Wideband (0.045-6.25 GHz) 40 km analogue fibre-optic link with ultra-high (> 40 dB) all-photonic gain." *Electron. Lett.*, vol. 42, no. 9, pp. 552-553, 2006.
- [128]. V. J. Urick, Jason D. McKinney, John F. Diehl, and Keith J. Williams. "Fiber-optic links with all-photonic RF gain and low RF noise figure." in *Proc. IEEE/MTT-S Microw. Symp., 2011*, pp. 1-4.
- [129]. H. V. Roussel, M. D. Regan, J. L. Prince, C. H. Cox, J. X. Chen, W. K. Burns, G. E. Betts, E. I. Ackerman, and J. C. Campbell. "Gain, noise figure and bandwidth-limited dynamic range of a low-biased external modulation link." In *Microwave Photonics, 2007 International Topical Meeting on, 2007*, pp. 84-87.
- [130]. A. Karim, and J. Devenport. "Low noise figure microwave photonic link." in *Proc. IEEE/MTT-S Microw. Symp.*, 2007, pp. 1519-1522.
- [131]. Z. Yang, X. Xie, Q. Li, J. C. Campbell, and A. Beling. "20 GHz analog photonic link with 16 dB gain

- based on a high-power balanced photodiode." in *Proc. IEEE Photon. Conf., 2015*, pp. 144–145.
- [132]. M. R. Boss, D. C. Evans, and E. W. Jacobs. "Performance of a 40 GHz RF photonic balanced link using a polarization modulator." in *2013 IEEE Avionics, Fiber-Optics and Photonics Technology Conference (AVFOP)*, 2013, pp. 11-12.
- [133]. K. Sun, R. Costanzo, T. Tzu, Q. Yu, S. M. Bowers, and A. Beling, "Ge-on-Si waveguide photodiode array for high-power applications," *2018 IEEE Photonics Conference (IPC)*, Reston, VA, pp. 1-2, 2018.
- [134]. C. Chang, J. H. Sinsky, P. Dong, G. Valicourt, and Y. Chen, "High-power dual-fed traveling wave photodetector circuits in silicon photonics," *Opt. Express*, vol. 23, no. 7, pp. 22857-22866, 2015.
- [135]. L. Bogaert, K. Gasse, T. Spuesens, G. Torfs, J. Bauwelinck, and G. Roelkens, "Silicon photonics traveling wave photodiode with integrated star coupler for high-linearity mm-wave applications," *Opt. Express*, vol. 26, no. 26, pp. 34753-34765, 2018.
- [136]. A. Stohr, S. Babiél, P. J. Cannard, B. Charbonnier, F. v. Dijk, S. Fedderwitz, D. Moodie et al, "Millimeter-wave photonic components for broadband wireless systems," *IEEE Trans. Microw. Theory Techn.*, vol. 58, no. 11, pp. 3071–3082, 2010.
- [137]. C. Park and T. S. Rappaport, "Short-range wireless communications for next-generation networks: UWB, 60 GHz millimeter-wave WPAN, and ZigBee," *IEEE Wireless Commun.*, vol. 14, no. 4, pp. 70–78, Aug. 2007.
- [138]. S. M. Bowers, B. Abiri, F. Aflatouni, and A. Hajimiri, "A compact optically driven travelling-wave radiating source," in *Proc. Opt. Fiber Commun. Conf. (OFC)*, 2014, paper Tu2A.3
- [139]. M. Natrella, C. Liu, C. Graham, F. v. Dijk, H. Liu, C. C. Renaud, and A. J. Seeds., "Modelling and measurement of the absolute level of power radiated by antenna integrated THz UTC photodiodes," *Opt. Exp.*, vol. 24, no. 11, pp. 11793–11807, 2016.
- [140]. O. O. Olaode, W. D. Palmer and W. T. Joines. "Characterization of meander dipole antennas with a geometry-based, frequency-independent lumped element model." *IEEE Antenn and Wirel PR*, vol. 11, pp. 346-349. 2012.
- [141]. K. Sun, J. Moody, Q. Li, S. M. Bowers and A. Beling, "High power integrated photonic W-band emitter." *IEEE T Microwe Theory*, vol. 66, no. 3, pp. 1668-1677, 2017.
- [142]. R. H. Stolen, "Nonlinearity in fiber transmission," in *Proc. the IEEE*, 1980, vol. 68, no. 10, pp. 1232 1236.
- [143]. Z. Yang, S. Yu, L. Chen, H. Leng, M. Lan, Y. Qiao, and W. Gu, "Constant envelop minimum shift keying OFDM coherent optical communication system," *J. Lightw. Technol.*, vol. 30, no. 23, pp. 3627 3632, 2012.
- [144]. M. J. LaGasse, and S. Thaniyavaru. "Bias-free high-dynamic-range phase-modulated fiber-optic link." *IEEE Photon. Technol. Lett*, vol. 9, no. 5, pp. 681-683, 1997.
- [145]. J. D. McKinney, "Linearized phase modulated analog optical links." U.S. Patent No. 8,103,178. 24 Jan. 2012.

A. List of Publications

Journals:

1. **Y. Peng**, K. Sun, Y. Shen, B. Guo, A. Beling and J. C. Campbell, "40 GHz Analog Photonic Link Based on a High-Power Balanced Photodiode at 1064 nm," *J. Lightw. Technol.*, 2020 Dec.
2. **Y. Peng**, K. Sun, Y. Shen, A. Beling and J. C. Campbell, "Photonic generation of pulsed microwave signals in the X-, Ku- and K-band ," *Opt. Express*, vol. 28, no.19, 2020.
3. **Y. Peng**, K. Sun, Y. Shen, A. Beling and J. C. Campbell, "High-Power and High-Linearity Photodiodes at 1064 nm," *J. Lightw. Technol.*, 2020 May 7.
4. **Y. Peng**, J. Zang, K. Sun, Z. Yang, and J. C. Campbell. "High-Speed and High-Power MUTC Photodiode Working at 1064 nm," *Photon. Technol. Lett.*, vol. 31, no. 19, pp. 1584-1587, 2019.
5. Y. Shen, A. H. Jones, Y. Yuan, J. Zheng, **Y. Peng**, B. VanMil, K. Olver and J. C. Campbell. "Near ultraviolet enhanced 4H-SiC Schottky diode," *Appl Phys Lett*, vol. 115, no. 26, pp. 261101, 2019.
6. J. Zheng, Y. Yuan, Y. Tan, **Y. Peng**, A. Rockwell, S. R. Bank, A. W. Ghosh, and J. C. Campbell. "Simulations for InAlAs digital alloy avalanche photodiodes," *Appl Phys Lett*, vol. 115, no. 17, pp. 171106, 2019.
7. Y. Yuan, A. K. Rockwell, **Y. Peng**, J. Zheng, S. D. March, A. H. Jones, M. Ren, S. R. Bank, and J. C. Campbell. "Comparison of Different Period Digital Alloy AlnAsSb Avalanche Photodiodes," *J. Lightw. Technol.*, vol. 37, no. 14, pp. 3647-3654, 2019.
8. Y. Yuan, J. Zheng, Y. Tan, M. Ren, **Y. Peng**, A. K. Rockwell, S. R. Bank, A. W. Ghosh, and J. C. Campbell, "Temperature dependence of the ionization coefficients of InAlAs and AlGaAs digital alloy: erratum." *Photonics Research*, vol. 7, no. 3, 273-273, 2019.

9. J. Zheng, Y. Yuan, Y. Tan, **Y. Peng**, A. K. Rockwell, S. R. Bank, A. W. Ghosh and J. C. Campbell. "Digital alloy InAlAs avalanche photodiodes," *J. Lightw. Technol*, vol. 36, no. 17, pp. 3580-3585, 2018.

Conferences:

1. **Y. Peng**, K. Sun, Y. Shen, Y. Yuan, A. Beling and J. C. Campbell. "Optical Generation of Pulsed Microwave Signals with High-Power Photodiodes," *In 2020 IEEE Photonics Conference (IPC)*, 2020
2. **Y. Peng**, K. Sun, Y. Shen, A. Beling and J. C. Campbell. "High-Linearity V-Band InGaAs/InP Photodiodes Working at 1064 nm," *In CLEO: Science and Innovations*, SM3R. 2020.
3. **Y. Peng**, J. Zang, K. Sun, Z. Yang, and J. C. Campbell. "High-Power Flip-Chip Bonded Photodiode Working at 1064nm," *In 2019 IEEE Photonics Conference (IPC)*, pp. 1-2. 2019
4. J. Zheng, Y. Yuan, Y. Tan, **Y. Peng**, A. K. Rockwell, S. R. Bank, A. W. Ghosh, and J. C. Campbell. "Digital alloy-based avalanche photodiodes," *In 2018 IEEE Photonics Conference (IPC)*, pp. 1-2. 2018.
5. Y. Yuan, J. Zheng, Y. Tan, **Y. Peng**, A. K. Rockwell, S. R. Bank, A. W. Ghosh, and J. C. Campbell. "Comparison of Excess Noise in InAlAs and AlGaAs Digital and Random Alloy Avalanche Photodiodes," *In 2018 IEEE Photonics Conference (IPC)*, pp. 1-2. 2018

B. Vita

Yiwei Peng (彭义炜), son of Zhilin Peng (彭之林) and Yuzhong Lu (陆裕忠), was born on September 14th, 1994 in Nanjing, Jiangsu Province, China. After completing his study at High School Affiliated to Nanjing Normal University in 2012, he began his undergraduate study at Southeast University (SEU), majoring in Electrical engineering. In August 2017, he joined Dr. Joe. C. Campbell's group as a Ph.D. student. His current research focuses on high-power photodiodes and their applications in analog photonic links.

This dissertation has been typed by the author.